A COMPUTATIONAL STUDY ON THE LEAKAGE OF SUPERCRITICAL CARBON DIOXIDE THROUGH LABYRINTH SEALS

A Thesis

by

SANDEEP R PIDAPARTI

Submitted to the Office of Graduate and Professional Studies of
Texas A&M University
in partial fulfillment of the requirements for the degree of

MASTER OF SCIENCE

Chair of Committee,	Junthula Reddy
Committee Members,	Devesh Ranjan
	Karen Vierow
Head of Department,	Andreas Polycarpou

December 2013

Major Subject: Mechanical Engineering

ABSTRACT

To meet future energy needs the use of alternative fuel sources are gaining popularity. The supercritical carbon dioxide Brayton cycle has been proposed as a possible cycle for next generation nuclear and concentrated solar power generation. Large density fluctuations of carbon dioxide in the supercritical region can be exploited to maintain compressor inlet conditions close to the critical point and thereby, reducing the compressor work and the back work ratio. In order to improve the efficiency of turbomachinery equipment it is important to reduce internal leakage through seals.

A computational study was performed to understand the leakage through seals subject to large pressure differential using Open source CFD software OpenFOAM. FIT (Fluid Property Interpolation Tables) program is implemented in OpenFOAM to accurately model the properties of CO_2 required to solve the governing equations. To predict flow behavior in the two phase dome HEM (Homogeneous equilibrium model) is assumed to be valid. Effects of geometrical parameters and operating conditions are isolated from each other and a parametric study was performed in two parts to understand the effects of both geometrical parameters and operating conditions.

Results of the geometrical parameter study indicated that the carryover coefficient of a seal is independent of pressure drop across the seal and is only a function of geometry. A model for carryover was developed as a function of c/s (clearance to pitch ratio) and w_{cavity}/c (cavity width to clearance). It has been identified that the major non-dimensional parameter influencing the discharge through an annular orifice is

w_{tooth}/c (tooth width to clearance) and a model for C_d (discharge coefficient) can be developed based on the results we obtained. Flow through labyrinth seals can be considered as a series of annular orifices and cavities. Using this analogy, leakage rate equations can be written for each tooth and the mass flow rate can be modeled as a function of the discharge coefficient under each tooth and the carryover coefficient, which accounts for the turbulent dissipation of kinetic energy in a cavity. The discharge coefficient of first tooth in a labyrinth seal is similar to that of an annular orifice, whereas, the discharge coefficient of the rest of the tooth was found to be a function of the C_d of the previous tooth and the carryover coefficient.

To understand the effects of operating conditions, a 1-D isentropic choking model is developed for annular orifices resulting in upper and lower limit curves on a T-s diagram which show the choking phenomenon of flow through a seal. This model was applied to simulations performed on both an annular orifice and a labyrinth seal. It has been observed that the theory is, in general, valid for any labyrinth seal, but the upper and lower limit curves on a T-s diagram depend on number of constrictions. As the number of constrictions increases these two curves move farther away from the critical point.

Finally, some experimental results for a plain orifice ($L/D \sim 5$) were used to show the capabilities of the FIT model implemented in OpenFOAM. Error analysis indicated that OpenFOAM is capable of predicting experimental data within a 10 % error with the majority of data close to a 5 % error. This validates the FIT model and HEM assumption.

DEDICATION

This thesis is dedicated to my beloved family.

ACKNOWLEDGEMENTS

Throughout my graduate education, Dr. Devesh Ranjan has been an excellent mentor and I would like to thank him for his guidance during my time at STAML. I would also like to thank Dr. J.N. Reddy, Dr. Karen Vierow for taking time out of their busy schedules to provide valuable inputs on improving this thesis.

I would also like to express gratitude to Dr. Mark Anderson at the University of Wisconsin- Madison for his advice during the course of this project and also for the resources provided for performing these studies. A special mention of thanks to his students Haomin Yuan, John Edlebeck and Matthew Wolf for participating in weekly conference calls to discuss the progress on this project.

I would also like to thank my parents and sister for their patience. They were always supporting me and encouraging me with their best wishes.

Finally, I would like to thank all my lab mates and friends at STAML. Many thanks to Bhanesh, Bryce, Eric, Jacob and Sarat for helping me throughout this project.

TABLE OF CONTENTS

Page

LIST OF FIGURES

Page

LIST OF TABLES

Page

CHAPTER I

INTRODUCTION

With the ever increasing population of Earth, energy production has become a concern due to depleting supply and increasing cost of fossil fuels, such as oil, coal and natural gas. Moreover, these energy production options have adverse environmental impacts and potential long-term consequences from global climate change. For Earth to support its population, use of alternative sources of fuel, such as nuclear, solar and wind has become important more than ever. One of the Prominent, clean, safe, and cost-effective supplies is the nuclear energy.

As an international effort to meet future energy needs, ten countries- Argentina, Brazil, Canada, France, Japan, the Republic of Korea, the Republic of South Africa, Switzerland, the United kingdom, and the United States have agreed on a framework for international cooperation in research for a future generation of nuclear energy systems, known as Generation IV. These ten countries have joined together to form the Generation IV International Forum (GIF) [1], to assist with energy crisis in the future. To meet the Goals of GIF program namely sustainability, economics, safety and reliability, and Proliferation resistance and physical protection six generation IV systems have been proposed as described in Table 1.1. Three advanced cycles have been proposed for energy production in the SFR, LFR, SCWR, and VHTR categories. All three cycles operate in the supercritical region and take advantages of drastic property changes in this region.

Table 1.1: Six systems selected to generation IV by the GIF

Generation IV System	Acronym
Gas-Cooled Fast Reactor System	GFR
Lead-Cooled Fast Reactor System	LFR
Molten Salt Reactor System	MSR
Sodium-Cooled Fast Reactor System	SFR
Supercritical-Water-Cooled Reactor System	SCWR
Very-High-Temperature Reactor System	VHTR

While operating a cycle in subcritical region, continuous change of phase is needed to exploit the properties of both gases and liquids, whereas while operating a cycle in supercritical region, the fluid of interest can exhibit properties of both gas and liquid without undergoing a phase change. All these proposed cycles will be strictly operating in the supercritical state, thus only a single phase will exist throughout the cycle. This leads to a simplification of plant cycle and a reduction in the capital cost and running cost of the plant. Critical properties for all three cycles are shown in Table 1.2. One interesting fact to note is that the critical point of the helium is much lower than critical point of the other working fluids. To attain efficiencies as high as 45-48 % required turbine inlet temperature for a helium cycle is 880^{o} C and multiple recompression stages [2]. This high of an outlet temperature would disqualify most types

of structural metals and metal-based nuclear fuels. Hence, this cycle is a long-term area of research.

Table 1.2: Critical properties of fluids

Fluid	Critical Temperature[C]	Critical Pressure [MPa]
CO_2	30.95	7.377
He	-267.95	0.227
H_2O	373.95	22.06

Dostal *et al*. [2] notes that the concept of a "supercritical cycle" is rather ambiguous as it encompasses all cycles where working fluid passes through the supercritical region at one point or another. In this respect, there is a huge difference between cycles such as the supercritical water cycle (SCWR) and the S-CO2 Brayton cycle. The SCWR cycle is a Rankine cycle where the high pressure side operates above the critical point and hence removes complications related to phase transition on the high pressure side. This resulted in an overall increase in efficiency from ~ 33% in current nuclear power cycle to ~44%. The steam cycles however, are more complex than the gas cycles and feature multiple heat exchangers, and larger components that are not necessary in case of gas cycles.

Due to the issues described earlier, carbon dioxide was the next choice as a supercritical working fluid. Detailed thermodynamic analysis performed by Dostal *et al*.

[2] indicated that the S-CO_2 cycle always outperformed the helium cycle when operating between same temperatures. For the temperature range of interest, 550 to 650^o C, S-CO_2 cycle performs better than both supercritical steam and superheated steam Rankine cycles as shown in Figure 1.1. The Supercritical CO_2 cycle gains an additional efficiency benefit over the helium cycle due to better turbomachinery performance. This is mainly due to lower number of stages. In addition to the size reduction, another advantage of a S-CO_2 turbine is that it can be a single body design unlike steam and helium turbines which usually employ more turbine bodies. This further increases the differences in size as additional plena and piping are necessary. Figure 1.1 compares the sizes of steam, helium and supercritical CO_2 turbines.

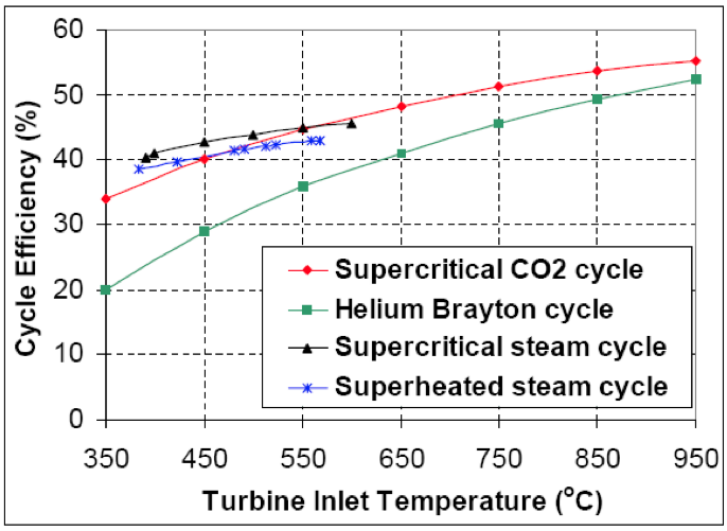

Figure 1.1: Comparison of efficiencies for advanced power cycles, figure is taken from [2].

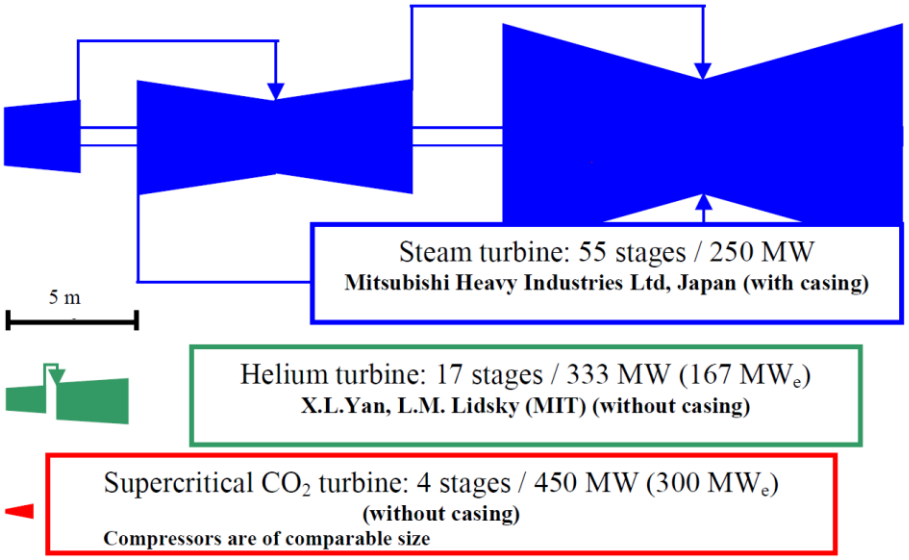

Figure 1.2: Comparison of turbine sizes, figure is taken from [3].

1.1 Overview of supercritical fluids

A supercritical fluid can be described as a substance whose state properties are at or above the critical pressure and temperature of that particular fluid. Critical point for any fluid is the point where saturated liquid and saturated vapor curve meet and difference in phases become hard to discern above this point. A critical point can be described based on any two of these three properties; critical Pressure (P_c), critical temperature (T_c) and critical density (ρ_c). In this region, there could be large differences in properties but fluid always remains in a single state. Mathematically, the critical point is defined as [4],

$$\left(\frac{\partial P}{\partial v}\right)_T = 0 \tag{1.1}$$

Supercritcal fluids are interesting due to large property variations at a temperature termed the pesudocritical temperature (T_{pc}) . The pseudocritical temperature can be defined as the tempeature at which specific heat reaches its maximum value, or mathematically as [4],

$$\left(\frac{\partial^2 P}{\partial v^2}\right)_T = 0 \tag{1.2}$$

An approximate relationship between the pseudocritical temperature and pressure is defined by Liao and Zhao [5] as

$$T_{pc} = -122.6 + 6.124P - 0.1657P^2 + 0.01773P^{2.5} - 0.0005608P^3 \tag{1.3}$$

Where T_{pc} is in ^oC and the pressure, P, is in bar.

Figure 1.3 shows approximate locations of the critical point and a sample of points on the pseudo-critical curve for CO_2 on a T-s diagram. Supercritical CO_2 or in general any supercritical fluid exhibits interesting property changes around critical point and pseudo-critical points as described earlier. Figure 1.4 gives an idea of density changes occurring as temperature is varied for a fixed operating pressure. It is very important to note that the change in density very close to critical pressure is about 300 kg/m^3 for a temperature change of less than 2^o C. In a S-CO_2 Brayton cycle, if compressor inlet is maintained very close to the critical point, CO_2 density is very high and the compressor work is very low, as it is expected to behave more like a pump. However, only a slight increase in temperature at the same pressure will cause the density to reduce by 50% and appreciably increase the compressor work which will reduce cycle efficiency. Hence, it is very crucial to maintain the cycle at desired operating conditions due to highly non-ideal behavior of S-CO_2.

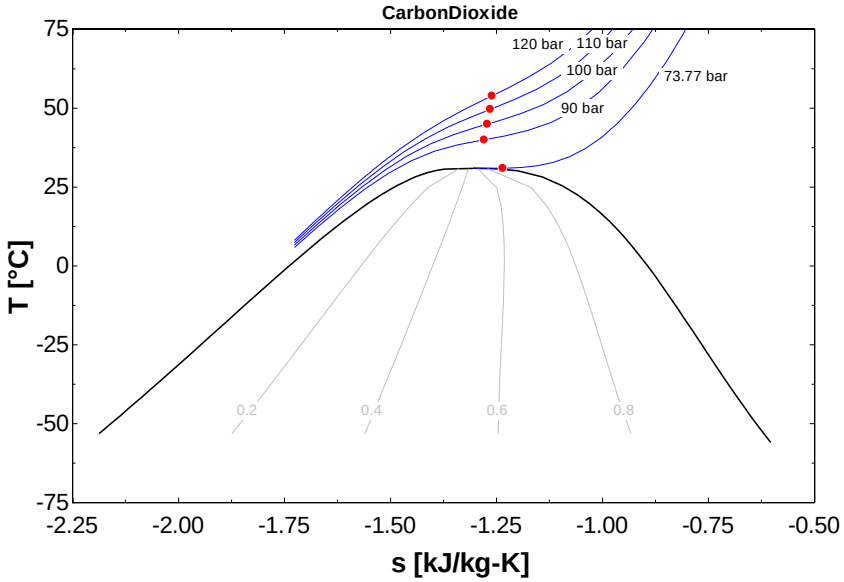

Figure 1.3: Approximate locations of critical and points on the pseudo-critical curve.

An efficient cycle is one in which the compressor input work is low relative to the turbine output work – equation (1.4) defines the back work ratio

$$BWR = \frac{\dot{W}_{compressor}}{\dot{W}_{turbine}} \tag{1.4}$$

It might also be worth-while noting that, as the operating pressure increases changes in density across the pseudo-critical point tend to flatten out and become less sensitive to the temperature as seen in figure 1.4. Apart from density, other properties like specific heat, dynamic viscosity and thermal conductivity exhibit similar kind of behavior as shown in figures 1.5, 1.6 and 1.7 respectively.

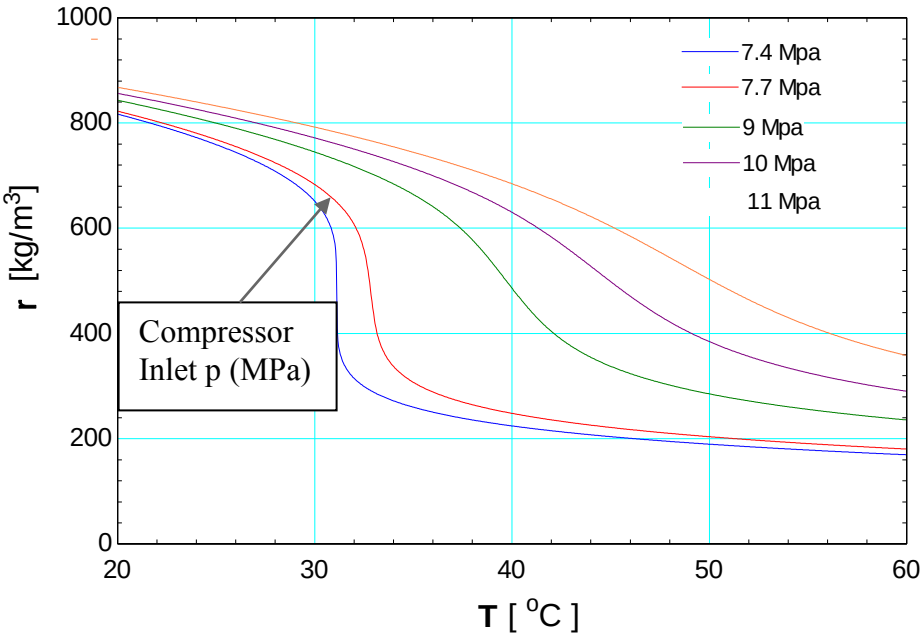

Figure 1.4: Density variations of CO_2 at varying operating pressures.

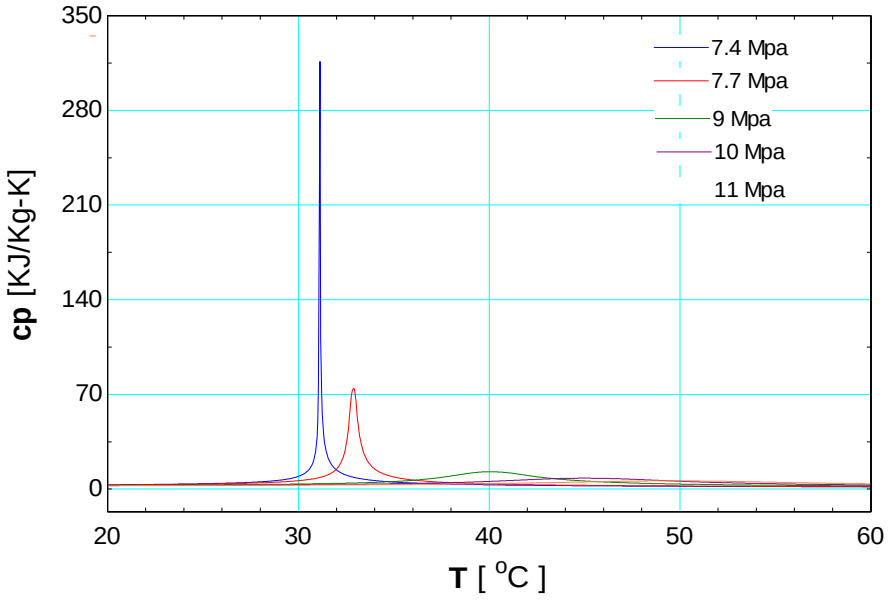

Figure 1.5: Specific heat variations of CO_2 at varying operating pressures.

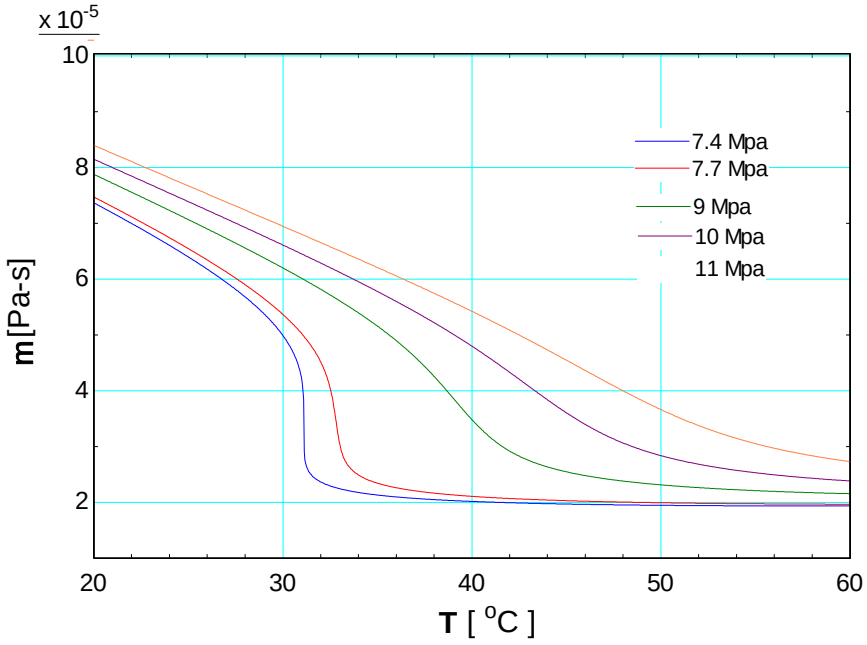

Figure 1.6: Dynamic viscosity variations of CO_2 at varying operating pressures.

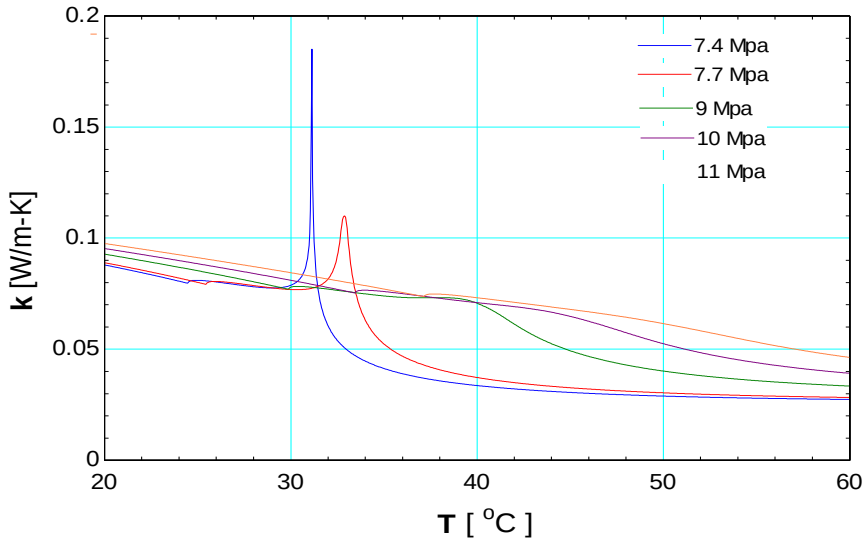

Figure 1.7: Thermal conductivity variations of CO_2 at varying operating pressures.

1.2 Simple and modified supercritical Carbon Dioxide Brayton cycles

Figure 1.8 shows a typical Brayton cycle without any inter-cooling or reheating. In this cycle fluid is compressed from the inlet condition, point, to point 2. Fluid exiting the compressor is pre-heated in recuperator using hot exhaust from the turbine (points 2 to 3). After the pre-heat stage, fluid enters the reactor to extract heat from the core and the fluid achieves its highest temperature in the cycle. An expansion through the turbine follows (points 4 to 5). After utilizing hot exhaust from turbine in the recuperator, excess cycle heat is rejected in the precooler, where fluid is cooled down to the inlet conditions. Analysis and optimization studies of simple closed Brayton cycle performed by Dostal *et al.* [2] resulted in an effective cycle efficiency of ~ 39%.

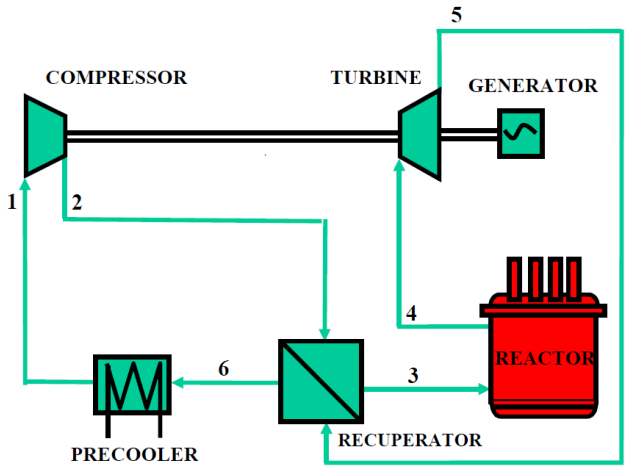

Figure 1.8: Closed Brayton cycle without inter-cooling or reheating, figure is taken from [2].

To improve efficiency, Dostal proposed the use of a recompression Brayton cycle as shown in figure 1.9. This cycle layout improves efficiency by reducing heat rejection from the cycle by introducing an additional compressor before precooler. The flow is split before entering precooler and heat is rejected only from part of the fluid flow. The outlet of the recompressing compressor is connected between the high and low temperature recuperators. In the main compressor a fraction of fluid is compressed to high pressure (points 1 to 2). In the low temperature recuperator it is pre-heated to the recompressing compressor outlet temperature (points 2 to 3). Then the fluid is merged with rest of the fluid flow from the recompressing compressor (point 3). Merged fluid is then preheated in the high temperature recuperator to reactor inlet temperature (points 3 to 4). The fluid then passes through reactor to attain highest temperature of the cycle (points 4 to 5). At this temperature fluid expands through the turbine to generate electricity. After leaving turbine the high temperature fluid is cooled in high and low temperature recuperators, where the available heat is transferred to the cooler high pressure side fluid flow. Before entering precooler the fluid flow is split (point 8). One part is recompressed to high pressure (points 8 to 3) and the other is cooled in precooler to the main compressor inlet temperature (points 8 to 1). Careful design of the recompression cycle can result in very attractive efficiencies of ~45% as reported in [2]. S-CO_2 has also been proposed to be used in Concentrated Solar Power (CSP) [6] Brayton cycle which is quite similar to the nuclear Brayton cycle; the only difference being the source of heat. Two layouts are being studied: one where supercritical carbon dioxide is

being heated by solar thermal energy and another where molten salt is being heated by solar thermal energy and the stored energy is transferred to CO_2 in a heat exchanger.

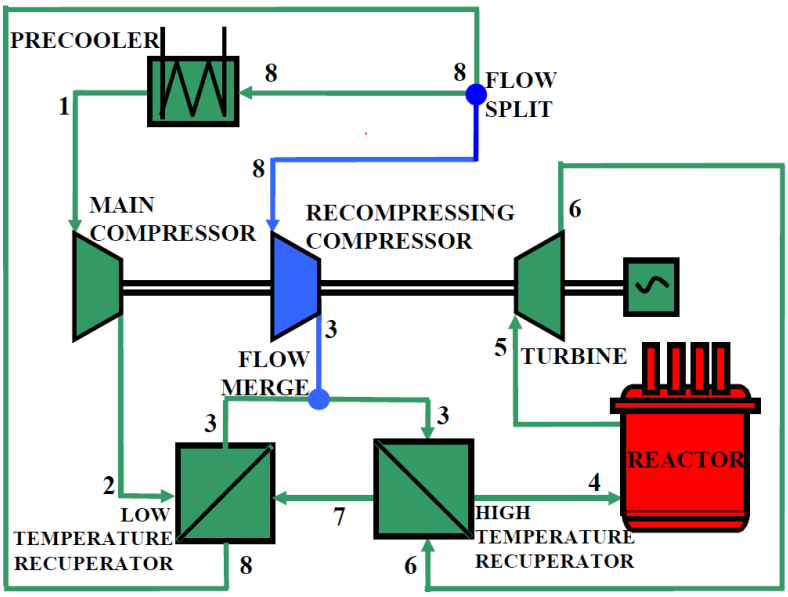

Figure 1.9: Recompression Brayton cycle layout, figure is taken from [2].

Figure 1.10 shows a proposed CSP cycle. In this cycle molten salt is passed through solar field where power towers, linear Fresnel and parabolic troughs concentrate solar energy onto the molten salt. CO_2 is heated to proposed turbine inlet temperature of 470^{o} C. After expansion through turbine, CO_2 passes through low and high temperature recuperator rejecting heat to cold stream before getting compressed in two stages as indicated in the Recompression Brayton cycle. Also present in the layout are two tanks: one hot and one cold. These tanks are used to store thermal energy to use when there is little or no solar thermal energy available.

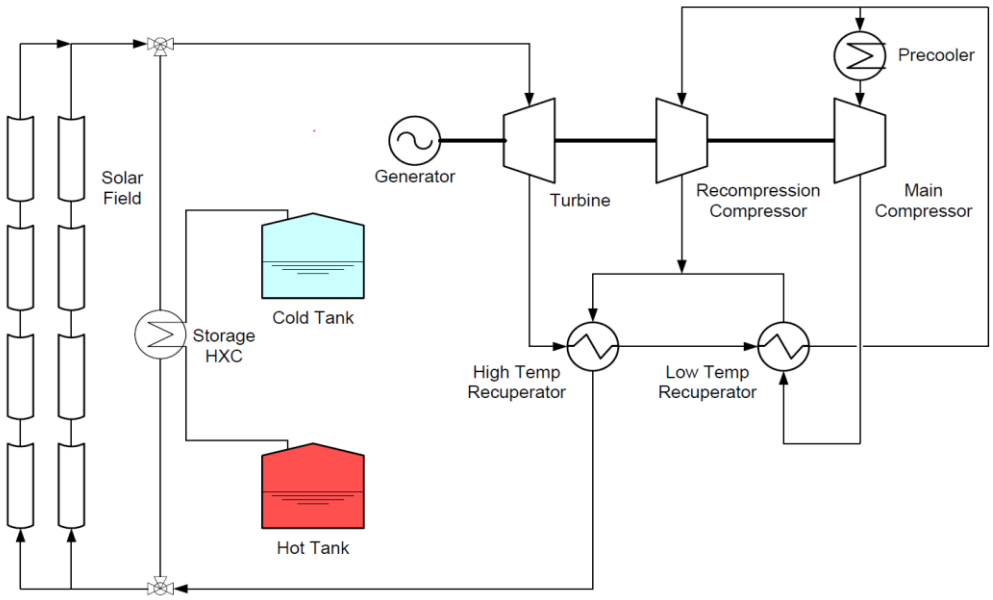

Figure 1.10: Simplified schematic of a solar thermal S-CO_2 recompression Brayton cycle, picture taken from [6].

Key to successful and efficient operation of a S-CO2 Brayton cycle is: Proper design of recuperator and the turbomachinery equipment. Design of recuperator is a whole different study by itself and is beyond the scope of this thesis. Main objective of this current investigation is to examine the problem of leakage through shaft seals implemented in the S-CO_2 Brayton cycle. Understanding the leakage problem associated with S-CO_2 will help in better design of turbomachinery components.

1.3 Motivation for current study

Labyrinth seals are commonly used in rotating machines such as pumps, compressors, and turbines. They are typically selected in applications where there is high relative speed between rotating components to limit the leakage of the working fluid. In its simplest form, a labyrinth seal consists of a series of radial fins forming a restriction to an annular flow of fluid. Labyrinth seals work by throttling the flow through successive openings in series. In each throttle, static pressure difference accelerates the flow and some of the kinetic energy associated with the flow is dissipated by turbulence induced due to intense shear stress and eddy motion in the cavity that follows. Despite careful labyrinth seal design and selection of labyrinth seal parameters, flow will inevitably be carried straight from one fin to another. This primary problem is due to the fact that shaft seals cannot create a hermetic seal about a rotating mechanism across a large pressure gradient. As a result, working fluid will leak out of the compressor and into the cavity region. Figure 1.11 provides a very simplified explanation of this situation. Windage losses associated with the turbomachinery components heavily depend on the density inside generator cavity. In a scenario where there are no labyrinth seals to isolate the compressor from the generator cavity, pressure in the generator cavity region will quickly increase to match the pressure in fluid compression region and density will increase to such a level as to make the windage losses unmanageable. Even with the presence of labyrinth seals, by virtue of natural pressure gradient from working fluid compression to generator cavity region, a certain amount of leakage is expected.

An idea to reduce the windage losses in cavity region is to decrease the density of fluid in cavity region by incorporating a secondary system to draw out residual working fluid from the cavity region. An offsetting performance penalty is related to the pumping losses that have been introduced into the overall system energy balance.

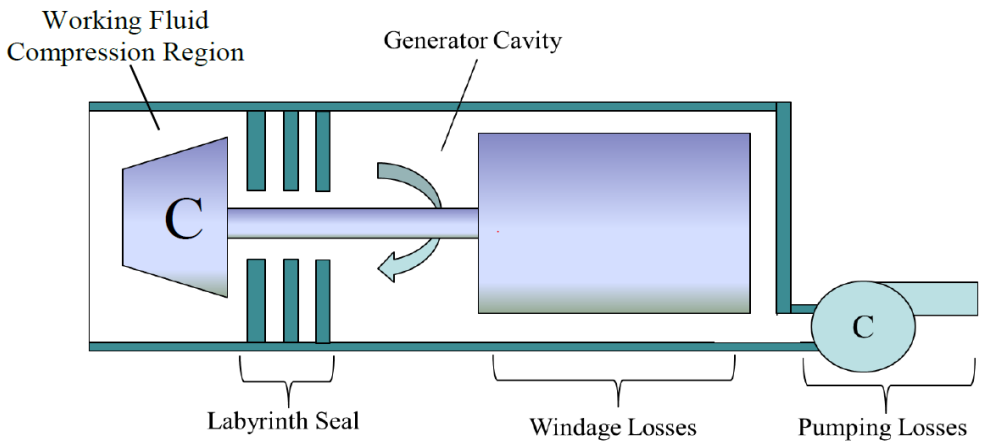

Figure 1.11: S-CO_2 compressor-generator assembly, picture taken from [7].

A natural tradeoff exists in this situation, where the windage losses are inversely related to the pumping losses as a function of cavity pressure. Hence, proper design of the turbomachinery seals would reduce the power lost for a given cavity pressure, which is the primary motivation behind these studies. Before designing advanced seals like dry lift off, staggered or honeycomb labyrinth seals for use in the S-CO_2 Brayton cycle it is worthwhile to perform studies on the flow of CO_2 through straight labyrinth seals to understand the basic underlying physics. Later-these concepts can be modified and extended to design hybrid seals.

Figure 1.12 shows a generic straight through labyrinth seal. This figure also defines some of the important nomenclature related to labyrinth seals. Labyrinth seals can be divided into two categories: one with seals on rotor and the other one with seals on the stator which will be the primary focus of this investigation.

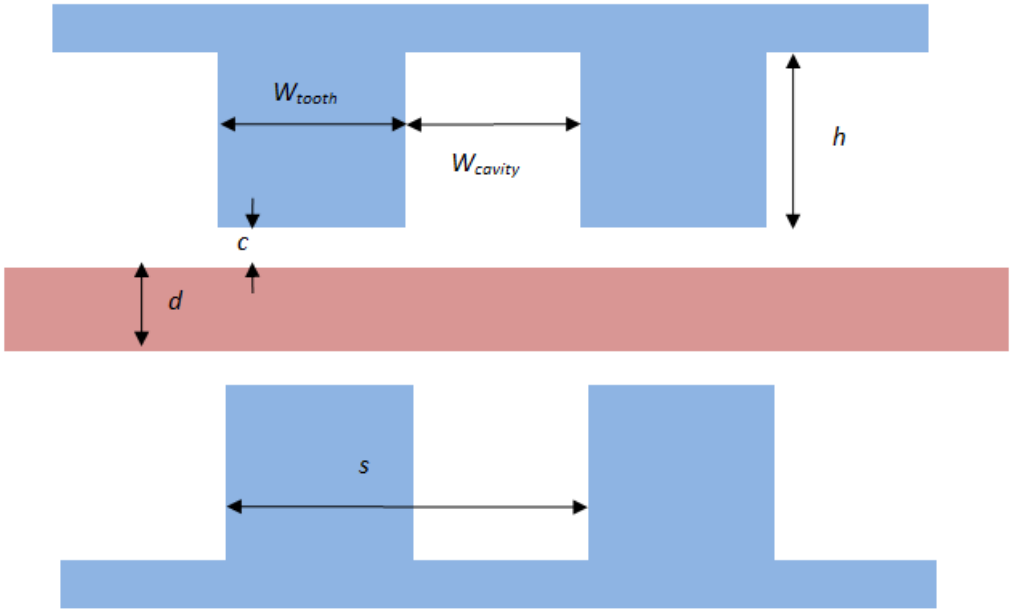

Figure 1.12: Generic straight through labyrinth seal.

1.4 Organization of thesis

This chapter gave a brief introduction to the supercritical fluids and explained the importance of supercritical fluids in advanced power generation cycles using nuclear and concentrated solar power as heat sources. The advantages of using S-CO_2 as working fluid instead of other competitors like helium or water were also demonstrated. Emphasis was laid on the design of better seals to minimize the losses in S-CO_2 Brayton cycle, which is the primary motivation behind this study.

Chapter II will provide a literature review. There is very little work published on the flow of supercritical fluids through labyrinth seals but there is some work published on the flow of incompressible and ideal fluids through labyrinth seals. This chapter will provide information about the various parameters which need to be considered for a labyrinth seal parametric study and their effects on the incompressible and ideal fluid flows is explained. Some previous work on two phase flow of water through nozzles and orifices will also be summarized.

Chapter III will explain the theory behind numerical modeling and the equations which are solved by OpenFOAM will be provided. A closure to these equations is provided by modeling the properties of CO_2 using biquintic spline interpolation method (FIT).

Chapter IV is divided into three parts. The first part of this chapter presents the numerical results of simulations performed to understand the effects of geometrical parameters while holding operating condition constant for all the cases. The second part

of this chapter will explain the numerical results of simulations performed to understand the effects of operating conditions while holding the geometry constant.

Chapter V facilitates comparison of the numerical results with the experimental results for S-CO_2 flow through a plain orifice.

Chapter VI will draw conclusions from the parametric study performed and some information will be provided about the construction of an experimental facility which will be used to validate the numerical results in future.

CHAPTER II

LITERATURE REVIEW

As an initial effort towards development of advanced power cycles Sandia National Laboratories have constructed a small scale Brayton cycle loop to study the key issue of compression near the critical point of supercritical working fluid. Details of the small scale loop can be found in the report generated by them [8]. As indicated in the report, during the compression process density changed only by 10%. This "near incompressibility" coupled with a high density fluid causes power in the compressor to be low compared to an ideal gas. To address the issue of leakage they used a four teeth labyrinth seal that closely approached staggered steps in the compressor shaft to limit flow through the seal. Because of the close approach to the critical point they suggested that it is desirable to understand the behavior of cycle in case the compressor inlet conditions drifts below the critical point and into the two phase region. They estimated leakage rates through the labyrinth seals by using a correlation developed by Egli, (1937) or by a simpler but related correlation by Martin, (1908). The predicted leakage for the Sandia operating conditions is based on the Martin's model for non-choked flow through multiple labyrinth seals assuming a constant discharge coefficient of 0.61. They found out that the leakage rate through the labyrinth seal is insensitive to the shaft rotation even at speeds as high as 70,000 rpm.

2.1 Previous work on two phase flows

In order to design better nozzles, Starkman *et al*. [9] performed experiments to investigate the flow of high pressure, low quality steam in de Laval nozzles and compared the experimental data to three simple models: a) Isentropic expansion, b) Frozen composition, c) Slip flow model.

a) The isentropic homogeneous expansion model assumes that the velocities of both the phases are equal, and that thermal equilibrium exists between phases. Neglecting the initial velocity, fluid velocity at any section is simply determined based on an energy balance.

$$V = [2g(h_e - h)]^{\frac{1}{2}} \tag{2.1}$$

$$G = \frac{\dot{m}}{A} = \frac{V}{v,} \tag{2.2}$$

The specific volume is evaluated from,

$$v = xv_g + (1 - x)v_f \tag{2.3}$$

b) The frozen composition model assumes that the velocities of both the phases are equal and that there is no heat or mass transfer between the phases which means that the quality remains constant. Assuming that gas dynamics principles hold true the following equations can be derived from simple fluid mechanics analysis,

$$h_e - h^* = x_c v_c p_c \frac{k}{k-1}\left[1 - r^{\frac{k-1}{k}}\right], \tag{2.4}$$

$$G = \frac{\dot{m}}{A} = \frac{V}{v,} \tag{2.5}$$

$$v = xv^* + (1 - x)v_f \tag{2.6}$$

The specific volume of the vapor at the critical section (v^*) is calculated from isentropic equation, $pv^{\gamma} = C$. The specific volume for liquid (v_f) is determined at the chamber condition. Then,

$$V = \sqrt{2g(h_e - h^*)} \tag{2.6}$$

The pressure ratio r^* follows from,

$$r^* = \frac{p^*}{P_c} = \left[\frac{2}{k-1}\right]^{\frac{k}{k-1}} \tag{2.7}$$

Finally, G can be written as

$$G = \frac{1}{v}\sqrt{2gx_c v_c p_c \frac{k}{k-1}\left[1 - r^{*\frac{k-1}{k}}\right]} \tag{2.8}$$

c) The slip flow model allows limited momentum interchange between phases, hence, both the phases travel at different velocities, but for calculations thermodynamic equilibrium is assumed between the phases. The energy equation for the slip flow model neglecting initial velocity is

$$h_e - h = \frac{xV_g^2}{2g} + \frac{(1-x)V_f^2}{2g} \tag{2.9}$$

Equation 2.9 can be rearranged to solve for the velocity of gaseous phase

$$V_g = \sqrt{\frac{2(h_e - h)}{x + (1-x)y^2}}$$

Where $y = V_g/V_f$ is the inverse of slip ratio.

Experimental comparison done by Starkman *et al.* [9] showed that the isentropic homogeneous equilibrium model over predicts the mass flow rate by about 10% for a vapor quality of 10% or higher and deviates sharply from the experiments when the vapor quality is less than 10%. They also found out that when the initial state is in two-phase dome, the mass flow rate is bounded by the isentropic homogeneous equilibrium model and the slip flow model. The ratio of mass flow rates predicted by the slip model to the mass flow rates predicted by the isentropic homogeneous model is given as,

$$\frac{\dot{m}_{slip}}{\dot{m}_{HEM}} = \frac{[xv_g+(1-x)v_f]}{\left[xv_g+\frac{1-x}{y}v_f\right]}[x+(1-x)y^2]^{-\frac{1}{2}}$$

Several authors tried to model the slip ratio for predicting the two phase mass flow rate through orifices based on the slip model, some of the work by previous authors is presented below.

Lockhart and Martinelli [10] developed generalized empirical curves for the simultaneous flow of air and liquids including benzene, kerosene, water, and various oils in pipes with varying diameters. They introduced a new parameter *X*, equal to the square root of the ratio of the pressure drop in pipe if liquid flowed alone to the pressure drop if gas flowed alone as shown in equation (2.10).

$$X^2 = \frac{\left(\frac{\Delta P}{\Delta L}\right)_l}{\left(\frac{\Delta P}{\Delta L}\right)_g} \tag{2.10}$$

The analysis was unsuccessful in the sense that no equations suitable for predicting pressure drop were obtained but only empirical curves were developed. Details of the analytical derivation can be found in [10].

Chisholm, (1967) [11] developed equations for predicting pressure drop by following the same theoretical analysis done by Lockhart and Martinelli [10] but including the interfacial shear force between the phases. They defined a "shear ratio factor" which is given as

$$S_R = \frac{S}{A_G \, \Delta P_{twophase}} \tag{2.11}$$

Where, S is shear force per unit length of pipe at the interface between phases. Chisholm [11] also introduced a shear force dimensionless function *Z*, which is defined as

$$Z = \left(\frac{1 + \frac{S_R A_G}{A_L}}{1 - S_R} \right)^{0.5} \tag{2.12}$$

Previous work by Chisholm, suggested that for the flow through orifices Z tends to approach a constant value independent of the individual phase flow-rates. Using a trial and error method they found out that a value of *Z*~14 gave a good agreement with Lockhart and Martinelli's empirical values. They went on to theoretically show that *Z* ~ ∞ for annular flow and for a no local slip condition in a rough pipe and they suggested the use of slip ratio,

$$K = \left[1 + x \left(\frac{\rho_l}{\rho_g} - 1 \right) \right]^{0.5} \tag{2.13}$$

Fauske, (1962) [12] derived theoretical expressions for the slip ratio to determine the critical mass flow rates for steam-water mixtures. They showed that sonic velocities are not achieved in case of the critical two phase flow and concluded that the phenomenon for critical flow is significantly different for the two-phase flow when

compared to the single phase flow. Fauske's slip ratio, equation (2.14), is based on minimizing the two phase momentum flow rate.

$$K = \left(\frac{\rho_l}{\rho_g}\right)^{\frac{1}{2}} \tag{2.14}$$

Zivi, (1964) [13] minimized the kinetic energy of a two phase flow and theoretically derived a slip ratio, equation (2.15), to obtain the maximum two phase flow rate. They explained that the minimum kinetic energy flow from a frictionless passage causes the minimum entropy production, a condition that characterizes a steady state thermodynamic process**.**

$$K = \left(\frac{\rho_l}{\rho_g}\right)^{\frac{1}{3}} \tag{2.15}$$

Moody, (1965) [14] compared the experimental results for the maximum flow rate of steam-water flow with the models developed by Fauske and Zivi, and they found out that Zivi's slip flow model is consistently better at predicting critical flow rates except at low qualities. They also developed a theoretical model to maximize the flow rate with respect to the local slip and static pressure for known upstream conditions. Their theoretical model is in good agreement with Zivi's slip flow model.

2.2 Previous work on flow through plain orifices and nozzles

Ward-Smith, (1979) [15] explained that the fundamental feature of flow through an orifice is separation of the flow at the sharp edge of the orifice resulting in different scenarios depending on the flow regime and the orifice length.

2.2.1 Incompressible flow regimes

For an incompressible flow at high Reynolds numbers, the flow characteristics depends strictly on whether the separated flow remains separated or reattachment occurs. Based on this theory several flow regimes have been identified. They are summarized below.

a) The separated flow regime ($0 < L/D < \phi$), occurs for small L/D (length to diameter) ratios, where the flow separates at the upstream edge and forms a discrete jet which contracts to a minimum cross-sectional area, at the vena contracta, as shown in figure 2.1. The value of ϕ is typically 0.75, in this range the coefficient of contraction C_c increases from 0.61 for $L/D = 0$ to 0.8 for $L/D = \phi$.

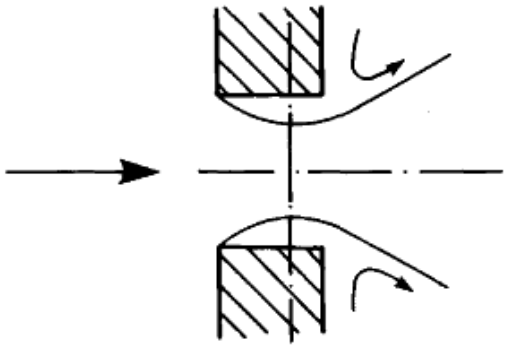

Figure 2.1: Schematic of separated incompressible flow, picture taken from [15].

b) The marginally reattached flow regime ($L/D \sim \phi$), occurs over a small but finite range of L/D very close to ϕ and the flow reattaches itself to the downstream edge and immediately separates again as shown in figure 2.2.

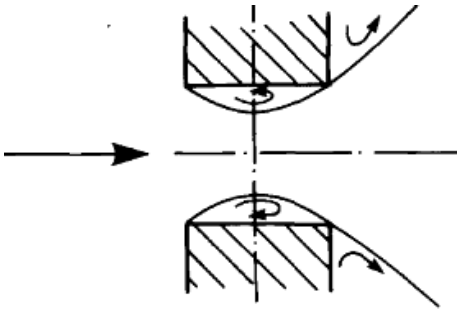

Figure 2.2: Schematic of the marginally reattached incompressible flow, picture taken from [15].

c) The fully reattached flow regime ($L/D > \phi$), occurs for values of L/D higher than a certain critical value, where reattachment occurs to form a turbulent boundary layer, resulting in a separation bubble being entrapped at the orifice entry, as shown in figure 2.3. In this type of flow the separation bubble is independent of L/D and C_c remains constant at about 0.61.

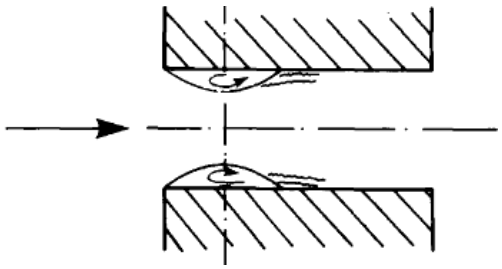

Figure 2.3: Schematic of the fully reattached incompressible flow, picture taken from [15].

2.2.2 Compressible flow regimes

a) The marginally reattached flow regime ($0 < L/D < \delta$): As ratio of the downstream to upstream pressure is reduced the flow rate increases until the velocity at the vena-contracta becomes sonic. Further reduction in pressure ratio reduces the area of vena contracta and moves it further upstream to a point where the area of the maximum contraction approaches the upstream edge of the orifice. The jet reattaches itself to the downstream edge, before separating again and expanding to downstream conditions as shown in figure 2.4.

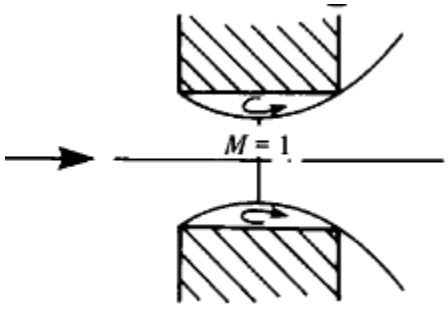

Figure 2.4: Schematic of marginally reattached compressible flow, picture taken from [15].

b) The fully reattached flow regime ($\delta < L/D < \varepsilon$): For orifices in this range of L/D the flow remains reattached to the surface at all pressure ratios from the incompressible limit to the onset of choking, as shown in figure 2.5, which is achieved when velocity at the vena contracta is sonic. The experimental evidence gathered by some of the authors shows that $\delta \sim 0.5$.

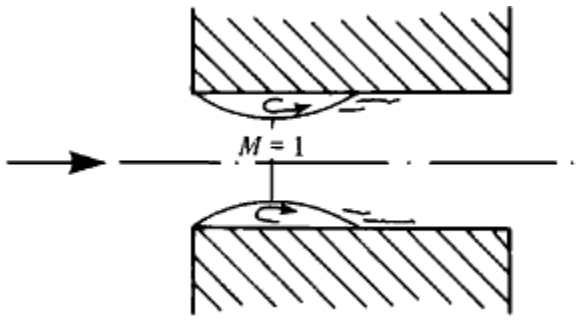

Figure 2.5: Schematic of fully reattached compressible flow, $\delta < L/D < \varepsilon$, picture taken from [15].

The fully reattached Flow regime ($L/D > \varepsilon$): In this flow regime, due to frictional effects of the developing boundary layer, the flow chokes at the downstream plane rather than choking at the vena contracta plane, as shown in figure 2.6. There is a particular value of $L/D = \varepsilon$ for which the flow chokes simultaneously at the exit and the vena contracta plane.

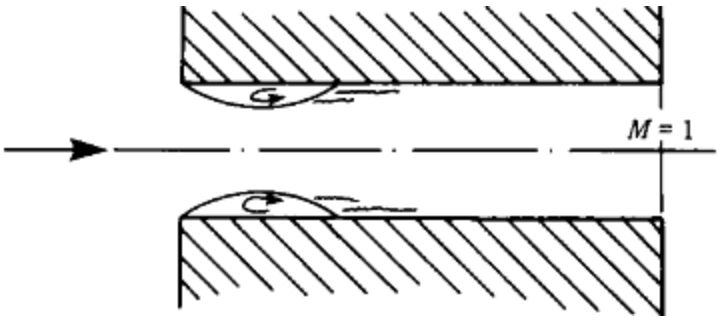

Figure 2.6: Fully reattached compressible flow, *L/D* > *ε* [15].

For orifices with *L/D* ranging between 0 and *ε*, choking occurs at the plane of the vena contracta and the discharge coefficient is dependent on *L/D*. In general, C_d decreases with an increase in *L/D*. For orifices with *L/D* ranging from $\delta < L/D < \varepsilon$, C_d is independent of *L/D*. This is a very important result indicating that all the orifices in this range have same C_d for choked flow. For orifices with $L/D > \varepsilon$, choking is referred to as Fanno choking and C_d decreases with increasing *L/D*. Since, the magnitude of the Mach number at the vena contracta depends on frictional characteristics from the point of reattachment and downstream, the value of C_d in this range will generally depend on Reynolds number and surface roughness. Ward and smith [15] compared C_d for a large database of experimental results covering a wide range of *L/D's*, as shown in figure 2.7.

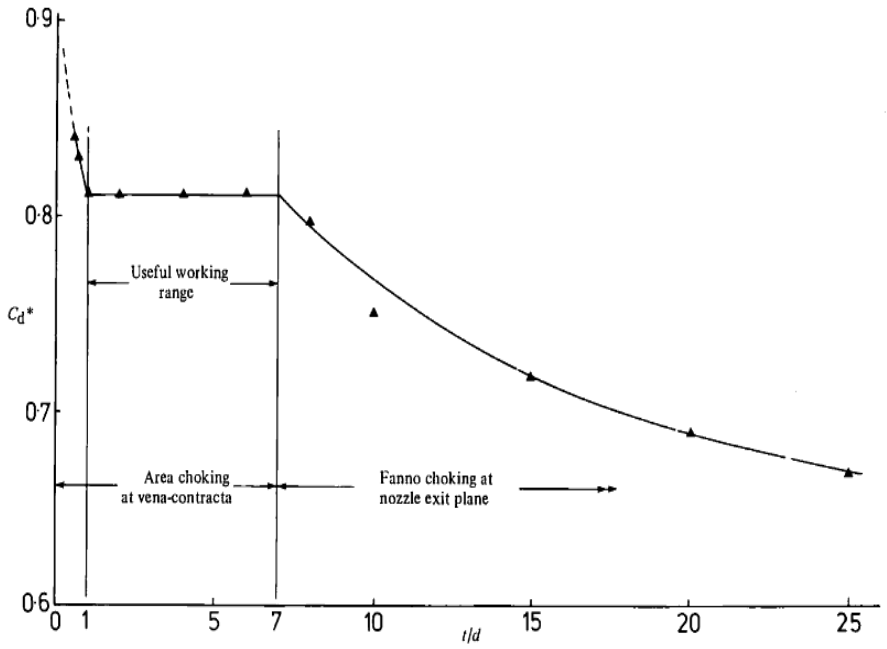

Figure 2.7: Graph showing the relationship between C_d, and *L/D*, picture taken from [15].

Linfield [16] has indicated that, a number of geometrical parameters and fluid flow conditions affect the discharge coefficient of orifices. The most important parameters influencing the discharge coefficient are: wall angle, α, exit-to-channel area ratio A_r, orifice shape χ, edge radius of curvature-to-diameter ratio R_{lip}/D, gas specific heat ratio k, ratio of outlet to inlet pressure r, and orifice thickness to diameter ratio L/D as shown in figure 2.8 and equation (2.16).

$$Cd = Cd\left(\alpha, Ar, \chi, \frac{Rlip}{D}, k, r, \frac{L}{D}\right). \tag{2.16}$$

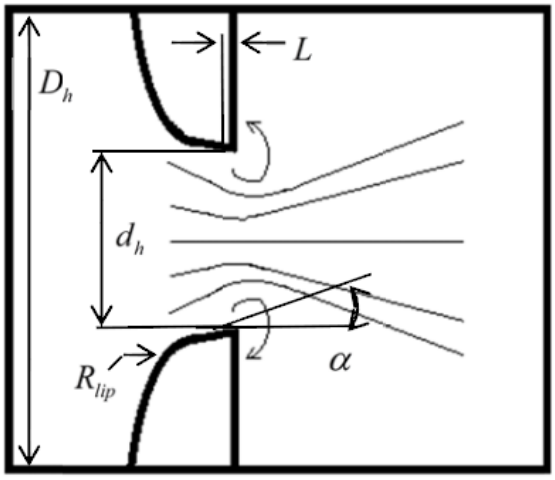

Figure 2.8: Geometrical properties related to the critical discharge coefficient, picture taken from [7].

Linfield studied the effect of all the parameters mentioned above except the effect of *L/D*, which was studied in detail by Ward-Smith [15]. The contraction coefficient has been used in literature to indicate the deviation between the actual to ideal flow rates. It is defined as,

$$C_c = \frac{A_{jet}}{A_{exit}} \tag{2.17}$$

Where A_{jet} is the area of cross section at the vena-contracta and A_{exit} is the cross sectional area of the orifice exit. The contraction coefficient has been traditionally used instead of the discharge coefficient and is only valid for inviscid, incompressible and subcritical flow. It loses its meaning when the flow becomes sonic (M = 1). Above this Mach number there is no final minimum-area of contracted jet, hence the discharge coefficient will be used to describe the flow throughout this thesis. Linfield developed a CFD code to numerically evaluate the discharge coefficient for both planar and axisymmetric flows

in subsonic and supersonic flow configurations. Details of the code and results can be found in [16].

2.3 Previous work on flow through annular orifices

The flow through an annular orifice differ from the flow through a plain orifice due to the fact that, fully developed annular flow involve a combination of two boundary layers (each extending from the wall to, say, a point of maximum velocity) which, unlike those that meet at the center of a pipe for plain orifices. This results in quite different distributions of velocity, shear stress, and turbulence quantities. Flow through plain orifice is a limiting case for annular orifice flow. The geometrical factors influencing the flow through a plain orifice will influence the flow through an annular orifice as well. Other factors affecting the flow through an annular orifice are the ratio of inner to outer diameter ($\beta = D_{in}/D_{out}$), eccentricity (e) of the annuli, rotation speed (ω) of the shaft/inner pipe. Hence, the discharge coefficient of an annular orifice can be expressed by equation 2.18.

$$Cd = Cd\left(\alpha, Ar, \chi, \frac{Rlip}{D}, k, r, \frac{L}{D}, \beta, e, \omega\right). \tag{2.18}$$

Brighton and Jones, (1964) [17] analyzed the fully developed incompressible turbulent flow through a smooth annular orifice, with annulus diameter ratio and Reynolds number (Re) as parameters. They varied β, and found out that the lower β values resulted in a more skewed velocity distribution than the exact solution for laminar flow. Also, the Reynolds number effect on velocity distribution is slightly less on the

inner profile than on the outer profile for small values of β, as shown in figure 2.9 (α used in the figure is equivalent to β in the thesis). It can be clearly seen that radius of the point of maximum velocity is less than that of laminar flow, with the deviation being greater for smaller radius ratios. They also found out that shear stress deviated from; it's typically linear distribution for laminar flow, as the value of β is reduced. As the point of maximum velocity is shifted towards the inner wall, the ratio of shear stress at the inner wall to that at the outer wall is reduced since a force balance shows that the inner-wall shear force must balance the pressure force on a smaller annular area. One interesting thing they found is that the mean velocity measurements followed the "law of the wall" from the outer surface to the point of maximum velocity but deviated significantly from the "law of the wall" from the inner wall to the point of maximum velocity, especially for lower values of β.

Tao and Donovan, (1954) [18], were one of the earliest investigators on flow through annuli both theoretically and experimentally to understand the effects of eccentricity and relative motion of the walls. It has been theoretically proven that the flow rate of an eccentric annulus is always greater than that of a concentric annulus with the amount of increase depending on lot of factors, mainly if the flow is laminar or turbulent. Tao and Donovan developed an analytical functional relationship for the increase in flow rate for both laminar and turbulent flows, as shown in equations (2.19 and 2.20).

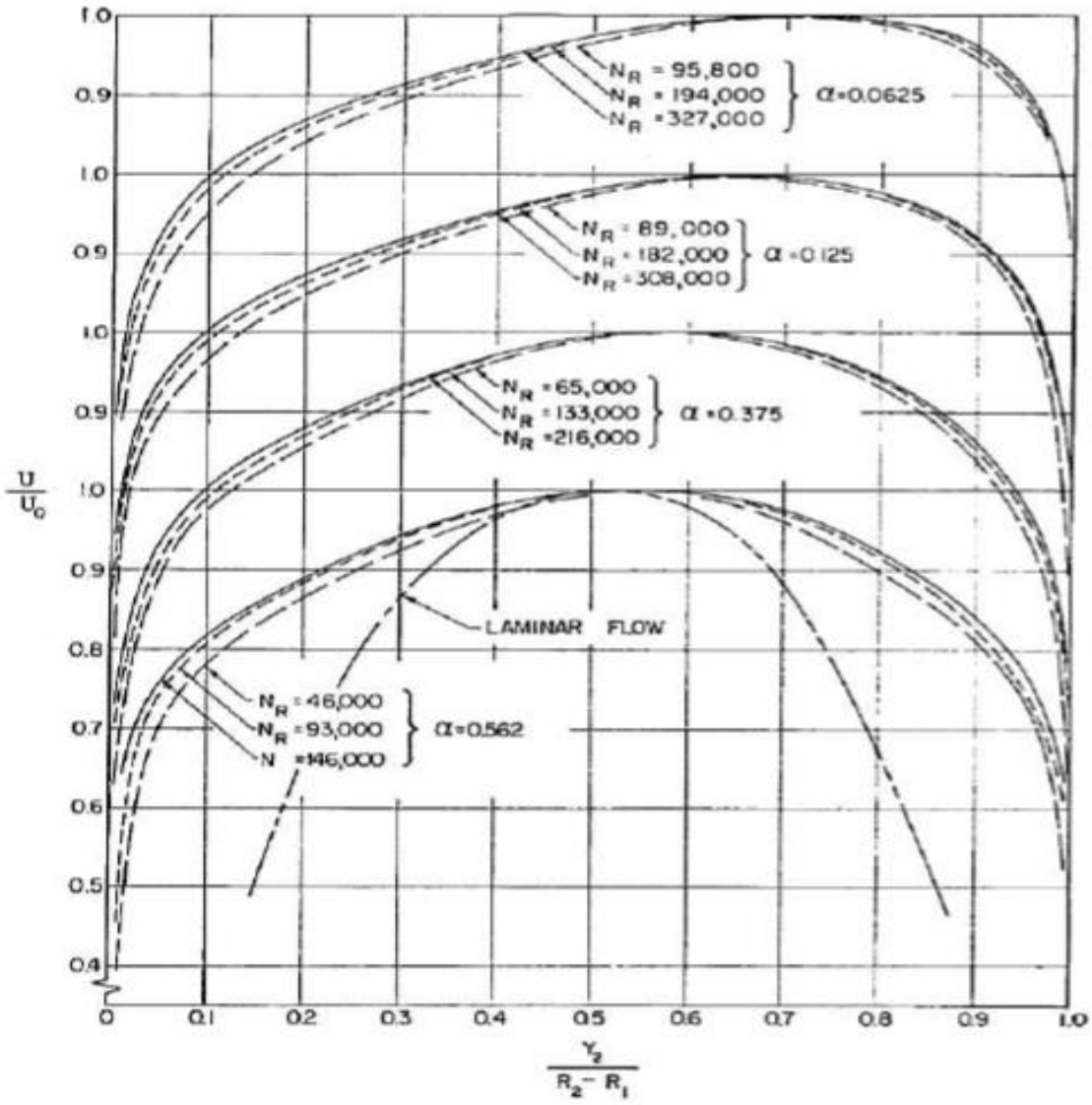

Figure 2.9: Mean velocity distribution for annular flow, picture taken from [17].

$$\frac{Q_e}{Q_{concentric}} = 1 + \frac{3}{2}\eta^2 \qquad (Laminar\ flow) \tag{2.19}$$

$$\frac{Q_e}{Q_{concentric}} = F\left(-\frac{m}{2}, \frac{1-m}{2}; 1; \eta^2\right) (Turbulent\ flow) \tag{2.20}$$

Where η is the ratio of eccentricity to clearance and m is the degree of the Legendre function which is expressed as an infinite series (details can be found in [18]). They performed experiments with water flow through an annulus for Re ranging from 800 to 30000 and plotted the friction factor against the Re for both laminar and turbulent flow regimes. For both flow regimes they found out that the friction factor can be represented by a power-law relationship, as seen in equation 2.21.

$$f = \frac{C}{Re^n} \tag{2.21}$$

Where, C = 170 and n =1.03 for laminar flow

C = 0.316 and n = 0.21 for turbulent flow

Tao and Donovan repeated the same set of experiments with inner wall rotating and observed that the resistance of flow-(pressure drop) is not effected in the laminar regime but for the turbulent regime pressure drop increased by a factor of $(\sec \varphi)^{0.79}$, where, φ is the angle between the absolute and axial velocities. For eccentric cases, they plotted the flow rate ratio between eccentric and concentric cases at identical conditions versus the eccentricity ratio, as shown in figure 2.10.

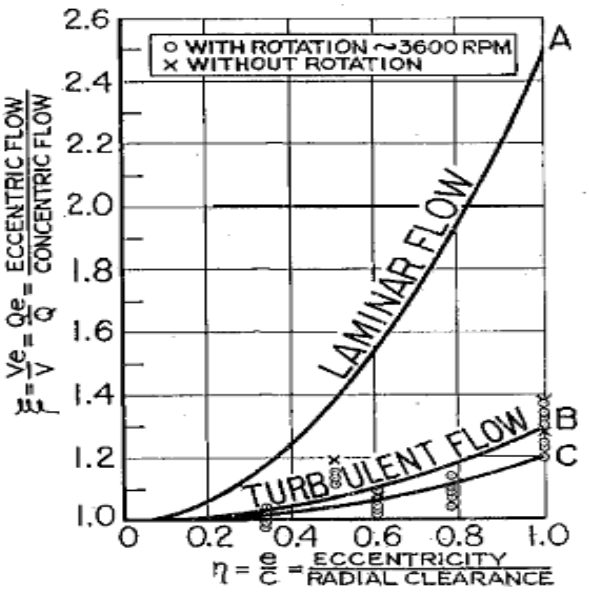

Figure 2.10: Flow ratio versus eccentricity ratio, picture taken from [18].

Jonsson and Sparrow, (1965) [19] conducted experiments to study the pressure drop and local friction factors for turbulent air flow through eccentric annular ducts with Re ranging from 18,000 to 180,000. They employed three different diameter ratios (0.281, 0.561 and 0.75) and varied the eccentricity from zero (concentric annulus) to unity (walls in contact). Pressure was measured at 42 different locations using pressure taps and the local pressure gradient was estimated by fitting a second-degree polynomial curve, from which the fully developed friction factor and shear stress were evaluated as,

$$f = \left(-\frac{dp}{dz}\right)\frac{D_h}{\frac{1}{2}\rho u_b^2},\ D_h = D_{in} - D_{out} \tag{2.22}$$

$$f = \frac{4\bar{\tau}}{\frac{1}{2}\rho u_b^2} \tag{2.23}$$

Jonsson and Sparrow plotted the friction factor versus the Re for all diameter ratios and eccentricities, as shown in figure 2.11, and realized that the friction factor could be correlated to the power law relationship as described in equation (2.21). They found out that the exponent, n, was 0.18 for all the Reynolds numbers, diameter ratios, and eccentricities. It was also observed that the value of C, in equation (2.21), depends on eccentricity and diameter ratios (β) and can be read from figure 2.11. From these results, it can be observed that for a fixed β and Re, the friction factor tends to decrease with increasing eccentricity. This effect is more pronounced for higher diameter ratios. For a fixed eccentricity and Re, the friction factor decreases as the diameter ratio is increased. Based on the pressure gradient information obtained from the experiments they also reported dimensionless hydrodynamic entrance lengths (z/D_h) for different eccentricities and diameter ratios as show in table 2.1. It has been that the entrance length increases with eccentricity for a fixed diameter ratio. For larger diameter ratios ($d1/d2 \sim 0.750$), the entrance length was about 3 times higher than that of the corresponding concentric case indicating that eccentricity is a decisive factor when dealing with the annular flows.

Table 2.1: Entrance Lengths, z/D_h

d_1/d_2	0.0	0.5	0.9	1.0
0.281	29	32	38	38
0.561	26	38	59	78
0.750	28	50	69	91

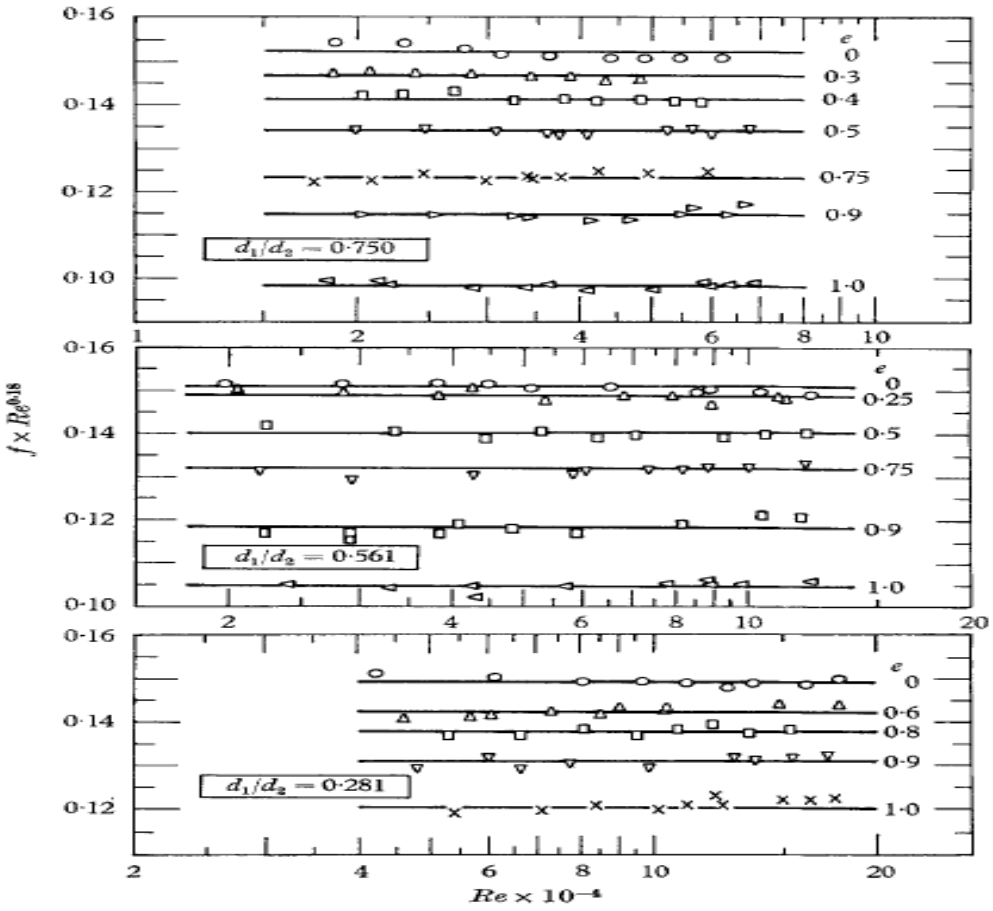

Figure 2.11: Friction factor results for eccentric annular ducts, picture taken from [19].

Sorgun *et al*. (2010) [20], developed a computational model for predicting the frictional pressure drop in concentric and eccentric annuli with the inner pipe rotating both for laminar and turbulent flow regimes and compared their computational results to the available experimental data. They observed that the pipe rotation has no noticeable effect on the frictional pressure loss for concentric annuli but drastically increases the frictional pressure loss in case of eccentric annulus, particularly at low flow rates, as can be seen in figures 2.12 and 2.13. They also found that the pipe rotation significantly increases axial velocities, especially for higher eccentricity cases.

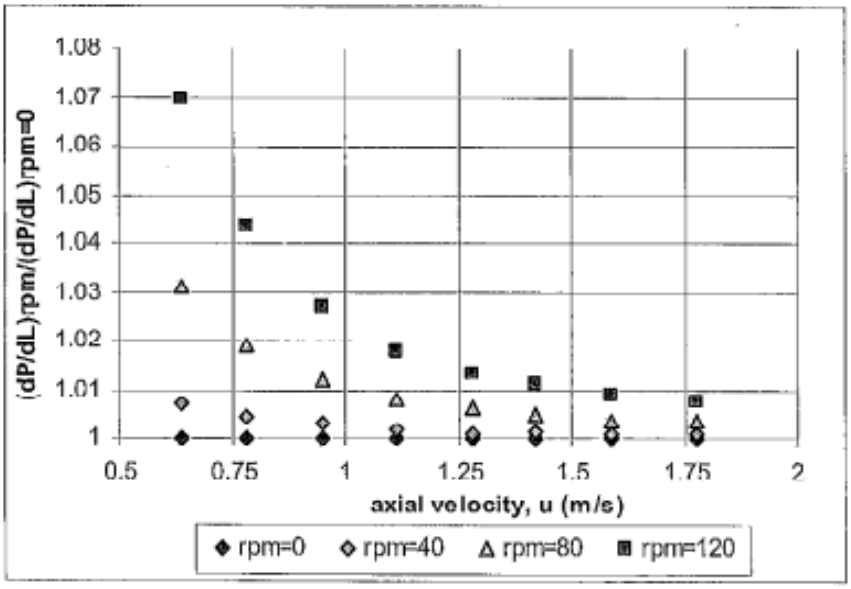

Figure 2.12: Pipe rotation effects on the frictional pressure loss of water through concentric annuli, picture taken from [20].

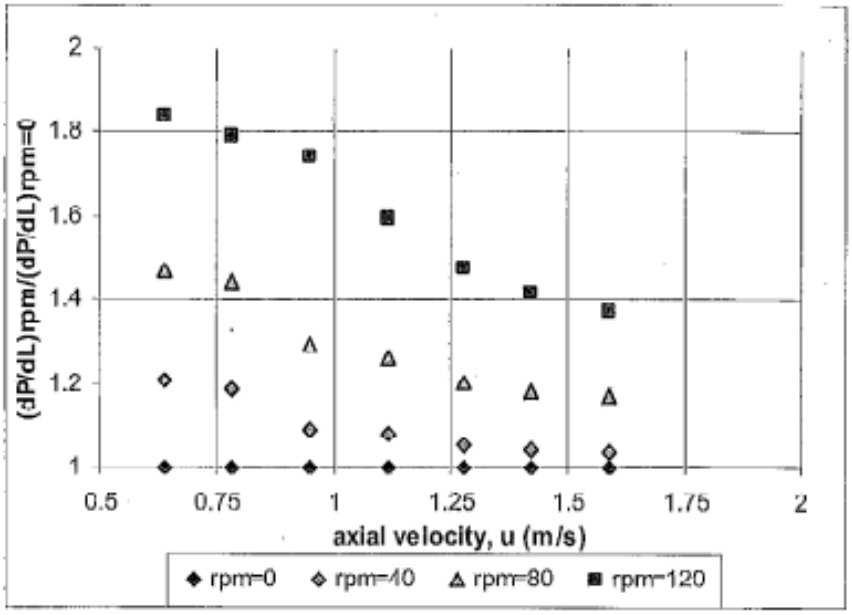

Figure 2.13: Pipe rotation effects on the frictional pressure loss of water through fully eccentric annuli, picture taken from [20].

2.4 Previous work on flow through labyrinth seals

Martin, (1908) [21] developed a purely analytical labyrinth seal leakage rate prediction equation, shown in equation (2.24), based on work done to achieve the required pressure drop. He assumed that the kinetic energy carryover ($\gamma = 1$) which might be true if the seal constrictions are placed far apart. This pure thermodynamic analysis is not sufficient to evaluate precisely the amount of energy remaining after each throttling cycle and hence, didn't match well with the experimental results as stated by many authors. However, it is the basis for several models which were developed later.

$$\dot{m} = \frac{AP_i}{\sqrt{RT_i}} \sqrt{\frac{1-\left(\frac{P_e}{P_i}\right)^2}{n-ln\left(\frac{P_e}{P_i}\right)}} \tag{2.24}$$

It has been noted that the spacing between the seal constrictions and the radial clearance between the shaft and seal constriction determine the amount of residual energy remaining after each throttling cycle. Generally speaking, smaller the distance between seal constrictions, larger clearance, and higher shaft rotation speed would result in more residual velocity energy through the deceleration zone.

Egli, (1937) [22] identified the need for a kinetic energy carryover coefficient and developed a semi-empirical model, shown in equation (2.25) based on Martin's equation by including an experimentally determined flow coefficient for steam to account for kinetic energy carryover.

$$\dot{m} = \gamma_{emperical} \frac{AP_i}{\sqrt{RT_i}} \sqrt{\frac{1-\left(\frac{P_e}{P_i}\right)^2}{n-ln\left(\frac{P_e}{P_i}\right)}} \tag{2.25}$$

Vermes, (1961) [23] modified Martin's equation and developed an expression for kinetic energy carryover based upon the boundary layer theory as shown in equations (2.26 and 2.27).

$$\gamma = \sqrt{\frac{1}{1-\alpha}} \tag{2.26}$$

$$\alpha = \frac{8.52}{\frac{s-w}{c}+7.23} \tag{2.27}$$

Where, α, is the relative amount of kinetic energy present upstream of tooth.

Stocker, (1975) [24] used an experimental procedure to design better labyrinth seals for high pressure ratio gas turbines. Their experiments were divided into 3 phases: In phase 1, they tested different seal configurations by analyzing the turbulence generated in cavities when water was flowing through each configuration. In this phase, they varied dimensions such as seal pitch, clearance, and step height as well as seal configuration. In phase 2, potential seal configurations were tested on a static seal rig using air flow. In phase 3, the configurations tested in phase 2 were tested on a dynamic rig at three extremely high peripheral speeds (262, 525 and 786 fps) to understand the effects of rotation. It was found out that the rotating seal tests produced a lower leakage rate than the static seal tests for all the selected configurations with a minimum reduction of 10.7% and a maximum reduction of 25 %. Although, Stocker was dealing with extremely high peripheral speeds variation in leakage rate is not as high as expected. This could be due to the fact that they were dealing with sophisticated seal configurations which are already showing excellent performance on a static rig than straight-through labyrinth seal types considered in this thesis.

Benvenuti *et al*. 1981 [25] set up an experimental test rig to understand what effect the number of throttlings have on the leakage rate. For a fixed seal length, given upstream conditions, and expansion ratio they found out that there is an optimum value for the number of throttlings (n_{opt}) and increasing the number of throttlings beyond n_{opt} would result in increased leakage rate. A qualitative explanation of this phenomenon can be understood by analyzing three possible flow patterns in the cavities, as shown in figure 2.14. For a higher throttling pitch (case A) it can be observed that the fluid fills in

the entire cavity after a sudden enlargement before contracting again. In case B, although the pitch is smaller compared to case A, it can be observed that the fluid still fills in entire cavity and hence the resistance to flow can be assumed to be same as that of case A.

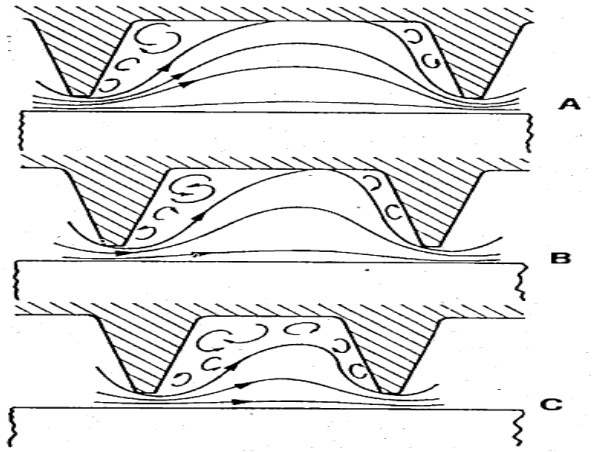

Figure 2.14: Possible flow patterns for different throttling pitches [25].

Therefore, case B would result in an optimum number of throttlings without change in the flow pattern. Increasing the number of throttlings over the optimum value would result in a reduction of pitch to such a level (case C) that the fluid doesn't fill in the entire cavity and thereby, increasing the leakage rate.

Demko *et al.* (1987) [26] performed combined computational and experimental investigation of an incompressible flow through labyrinth seals mounted on the shaft at low Re. They found out that at low Re, increasing the shaft peripheral speed resulted in the formation of a second recirculation zone (SRZ) counteracting the first one, as shown in figures 2.15 and 2.16, thereby, reducing the leakage rate. It was also found that for a

fixed Re this favorable formation of a SRZ occurs over a particular Taylor number (Ta), defined in equation (2.28).

$$Ta = \frac{W_{sh}c}{\nu}\sqrt{\frac{c}{r_{sh}}} \tag{2.28}$$

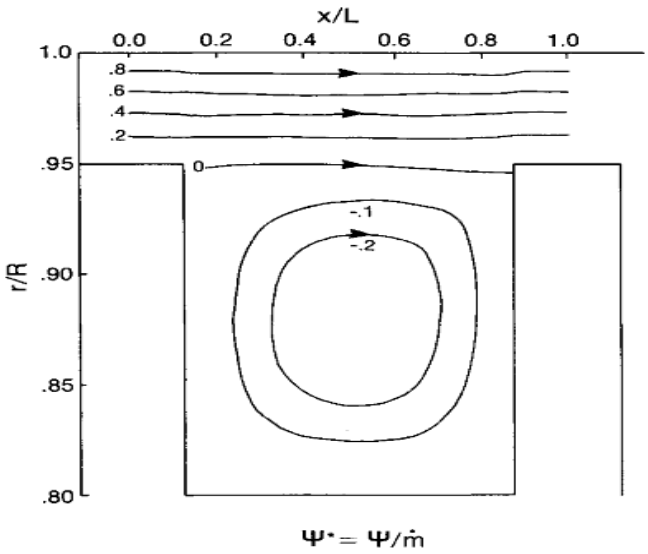

Figure 2.15: Streamline pattern for Re = 17,800, Ta = 0, picture taken from [26].

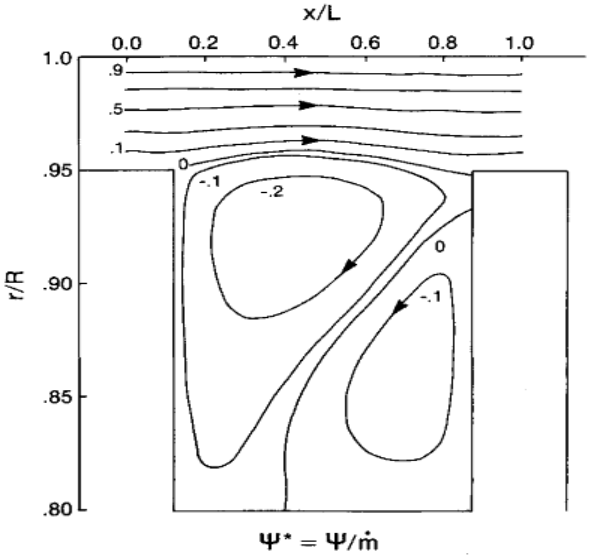

Figure 2.16: Streamline pattern for Re = 17,340, Ta = 19,000, picture taken from [26].

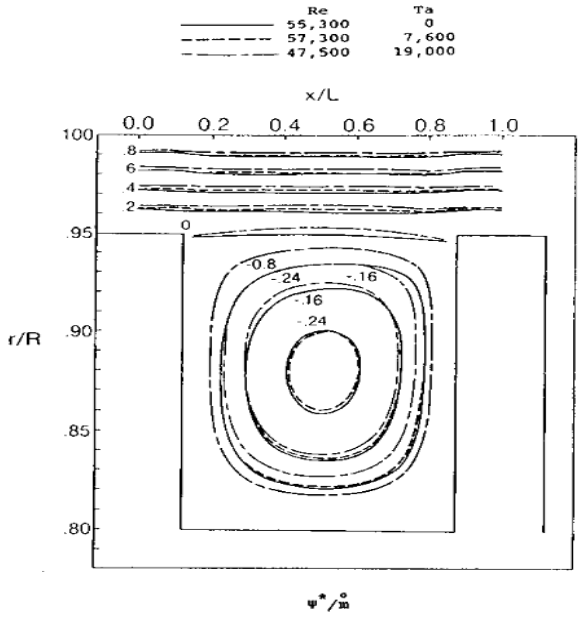

Figure 2.17: Streamline pattern for high Re, picture taken from [27].

Increasing the Reynolds number over a certain value for the same values of Ta, didn't result in formation of SRZ as presented by Demko *et al.* (1984) [27] and shown in figure 2.17.

Hodkinson, 1931 [28] modified Egli's approach to provide a semi empirical relation that was based on the assumptions of a gas jet's geometry. They assumed that the fluid jet expands conically from the tip of an upstream tooth at a small angle, β. A part of the jet impinges on the downstream tooth to recirculate in the cavity dissipating kinetic energy associated with the jet. The portion which is undissipated travels under the downstream tooth and carries over kinetic energy to the next cavity. They assumed that the angle θ (as shown in figure 2.18) is only a function of seal geometry.

Hodkinson, 1931 [28] modified Egli's approach to provide a semi empirical

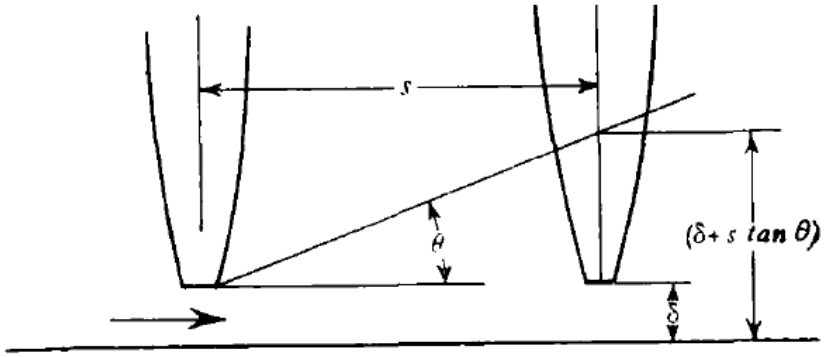

Figure 2.18: Kinetic energy carryover fraction, picture taken from [28].

Hodkinson gave following semi-empirical relation for seal leakage,

$$\dot{m} = A\alpha\Psi\gamma\sqrt{P_i\rho_i} \tag{2.29}$$

Where the expansion coefficient, ψ, which accounts for compressibility effects, is defined as

$$\Psi = \sqrt{\frac{1-\left(\frac{Pe}{P_i}\right)^2}{n-ln\left(\frac{Pe}{P_i}\right)}} \tag{2.30}$$

The kinetic energy carryover coefficient, γ, is modeled as a function of seal geometry alone, as seen in equation 2.31.

$$\gamma = \sqrt{\frac{1}{1-\frac{n-1}{n}\frac{\frac{c}{s}}{\frac{c}{s}+0.02}}} \tag{2.31}$$

The factor, α, is an experimentally determined flow coefficient, similar to the discharge coefficient.

Suryanarayanan, (2009) [29] extended the work of Gamal *et al*. [30] and developed a model for an incompressible discharge coefficient and carryover coefficient for water, and air through a labyrinth seal. The parameters used are illustrated in figure 2.19.

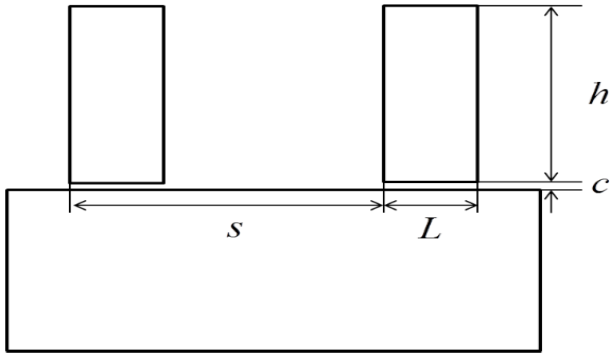

Figure 2.19: Parameters used in empirical model by Suryanarayanan, picture taken from [29].

Suryanarayanan isolated the effects of geometrical parameters and studied the effect of each individual parameter on C_d and γ. The model developed by Suryanarayanan is identified in equations (2.32) through (2.38), which are solved iteratively to estimate the leakage rate and pressure drop for each constriction. They compared the derived model with the previously available experimental data and reported a maximum error of 25 %. Suryanarayanan realized that the discharge coefficient of first tooth in a labyrinth seal is different from that of following teeth due to the fact that first tooth doesn't have a preceding cavity. Equation (2.32) represents the incompressible discharge coefficient of the first tooth in a labyrinth seal.

$$C_d|_{PR=1}^{1^{st}\,seal} = \frac{0.7757 - 0.002051\,L/c}{\left(1 + 44.86\,\frac{\frac{L}{c}}{Re_{D_h}}\right)^{0.2157}} \tag{2.32}$$

From the second tooth they took into account the carryover coefficient from preceding cavity and derived Equation (2.33) based on curve fit.

$$C_d|_{labyrinth}^{2^{nd}-n^{th}\,seal} = C_d|_{labyrinth}^{1^{st}\,seal}\,(0.925\gamma^{0.861}) \tag{2.33}$$

Carryover coefficient (γ) was isolated and studied based on pitch, cavity depth, tooth width, clearance to arrive at Equation (2.34)

$$\gamma = \left(1 - 6.5\left(\frac{c}{s}\right) - 8.638\left(\frac{c}{s}\right)\left(\frac{L}{s}\right)\right)\,(Re + R_o)^{\left(2.454\left(\frac{c}{s}\right)+2.268\left(\frac{c}{s}\right)\left(\frac{L}{s}\right)^{1.678}\right)} \tag{2.34}$$

$$R_o = \left(1 - 6.5\left(\frac{c}{s}\right) - 8.638\left(\frac{c}{s}\right)\left(\frac{L}{s}\right)\right)^{\left(\frac{-1}{2.454\left(\frac{c}{s}\right)+2.268\left(\frac{c}{s}\right)\left(\frac{L}{s}\right)^{1.678}}\right)} \tag{2.35}$$

Finally, to account for compressibility, a compressibility factor was introduced which was determined to be varying linearly with pressure ratio as shown in equation (2.36).

$$\Psi = 0.558PR + 0.442 \tag{2.36}$$

The empirical discharge coefficient and the compressibility factor are then input into equation (2.37) to determine the leakage rate through labyrinth seal

$$G_{empirical} = C_d|_{labyrinth}\Psi\sqrt{2\rho_{in}(P_{in} - P_{out})} \tag{2.37}$$

This model is applicable only under the conditions described below.

$$PR \rightarrow 1$$

$$0.0075 < \frac{c}{s} < 0.0375$$

$$0.0075 < \frac{L}{S} < 0.5$$

$$2.67 < \frac{L}{c} < 66.67,\ 0.75 < \frac{h}{s} < 0.4$$

$$134 < Re_{D_h} < 15000$$

CHAPTER III

NUMERICAL MODELING

This study is based upon CFD simulations performed using the open source software OpenFOAM 2.1.1. OpenFOAM is a C++ based CFD (Computational Fluid Dynamics) toolbox for development of customized numerical solvers based upon the applications of users. The applications developed in OpenFOAM fall under two categories: solvers, that are designed to solve a specific problem in continuum mechanics; and utilities, that are designed to perform tasks that involve data manipulation. The OpenFOAM distribution contains numerous solvers and utilities covering a wide range of problems, details of these can be found in chapter 3 [31] under standard solvers and standard utilities section.

One of the solvers of interest for this study is rhoSimplecFoam [31] which is a steady-state SIMPLEC based solver designed for laminar and turbulent RANS flows of compressible fluids. This solver solves a set of modified continuity, momentum, and energy equations programmed in C++ and necessary to represent a scenario in hand. The closure to these equations is provided by modeling properties of the fluid being simulated. One of the distinguishing features of OpenFOAM is its syntax for tensor operations and partial differential equations that closely resemble the equations being solved. Equation (3.1) is represented by the code shown in figure 3.1.

$$\frac{\partial \rho U}{\partial t} + \nabla . \varphi U - \nabla . \mu \nabla U = -\nabla p \tag{3.1}$$

```
solve
(
      fvm::ddt(rho,U)
    + fvm::div(phi,U)
    - fvm::laplacian(mu,U)
      ==
    - fvc::grad(p)
);
```

Figure 3.1: OpenFOAM syntax for differential equations, picture taken from [31].

A new solver termed as hRhoSimplecFoam has been developed in OpenFOAM which solves the same set of partial differential equations as rhoSimplecFoam but provides closure to the governing equations by using the user defined CO_2 properties instead of standard thermodynamic models used by the original solver.

This chapter provides an in-depth explanation of the solver hRhoSimplecFoam. First, the theoretical governing equations being solved by the application will be discussed. Next, details will be provided about the user defined CO_2 properties modeled into the application, wherein the problem setup will be explained as well. Finally, a table is generated showing the seal geometries and the operating conditions used in this study (Appendix A, B, C).

3.1 Governing equations

The Navier-Stokes (NS) equations are the basic governing equations for a viscous, heat conducting fluid flow problem and consist of equations for the

conservation of mass and momentum. The momentum equation is a vector equation obtained by applying Newton's laws of motion to a fluid element. It is supplemented by the mass conservation equation, also called the continuity equation. For a fluid flow problem involving the transfer of energy such as a heat transfer problem the energy equation must be used in addition to the NS equations [32].

The continuity equation (3.2), momentum equation (3.3) and energy equation (3.4) for a compressible fluid can be written as follows

$$\frac{\partial \rho}{\partial t} + \frac{\partial}{\partial x_j}\left[\rho u_j\right] = 0 \tag{3.2}$$

$$\frac{\partial}{\partial t}\left(\rho u_i\right) + \frac{\partial}{\partial x_j}\left[\rho u_i u_j + p\delta_{ij} - \tau_{ji}\right] = 0, \;\; i = 1,2,3 \tag{3.3}$$

$$\frac{\partial}{\partial t}(\rho e_o) + \frac{\partial}{\partial x_j}\left[\rho u_j e_o + u_j p + q_j - u_i \tau_{ij}\right] = 0 \tag{3.4}$$

For a Newtonian fluid, assuming that Stokes law is valid, the viscous stress is given by:

$$\tau_{ij} = 2\mu S_{ij}^* \tag{3.5}$$

Where the trace-less viscous strain-rate is defined by:

$$S_{ij}^* \equiv \frac{1}{2}\left(\frac{\partial u_i}{\partial x_j} + \frac{\partial u_j}{\partial x_i}\right) - \frac{1}{3}\frac{\partial u_k}{\partial x_k}\,\delta_{ij} \tag{3.6}$$

The heat-flux, q_j, is given by Fourier's law as:

$$q_j = -\lambda \frac{\partial T}{\partial x_j} \equiv -C_p \frac{\mu}{Pr}\frac{\partial T}{\partial x_j} \tag{3.7}$$

Where the laminar Prandtl number, *Pr* is defined by:

$$Pr \equiv \frac{C_p \mu}{\lambda} \tag{3.8}$$

The total energy, e_o, is defined by:

$$e_0 \equiv e + \frac{u_k u_k}{2} \tag{3.9}$$

Since, flow through seals is highly turbulent, turbulence modeling is important to capture the real scenario. There are numerous ways to model turbulence in a flow ranging from a simple linear eddy viscosity model to large eddy simulations (LES) and direct numerical simulation (DNS). In this thesis, two equation turbulence models which are one of the most common types of turbulence models are used. By definition, two equation models include two extra transport equations to represent the turbulent properties of the flow. Most often one of the transported variables is the turbulent kinetic energy, *k*. The second transport variable varies depending on what type of two-equation model is being used. Common choices are the turbulent dissipation, ε, or the specific dissipation, ω [32].

The equation for the ensemble averaged velocity is shown in equation 3.7.

$$u_i = \overline{u_i} + u_i' \tag{3.7}$$

The over-bar implies that the velocity is averaged, while the prime, ‘, implies the fluctuating component to the velocity. This same format is used for various other properties. A new set of equations can be developed for turbulent flows by modifying equations (3.2) through (3.4). The conservation of mass equation (3.2) remains the same for turbulent flow as well, while the momentum equation becomes:

$$\frac{\partial}{\partial t}(\rho\overline{u_i}) + \frac{\partial}{\partial x_j}(\rho\overline{u_i u_j}) = -\frac{\partial p}{\partial x_i} + \frac{\partial}{\partial x_j}\left[\mu\left(\frac{\partial \overline{u_i}}{\partial x_j} + \frac{\partial \overline{u_j}}{\partial x_i} - \frac{2}{3}\delta_{ij}\frac{\partial \overline{u_i}}{\partial x_j}\right)\right] + \frac{\partial}{\partial x_j}(-\rho\overline{u_i' u_j'}) \tag{3.8}$$

These equations are known as the Reynolds averaged Navier-Stokes equations (RANS).

The basis for all two equation models is the Boussinesq eddy viscosity assumption, which postulates that the Reynolds stress tensor, τ_{ij}, is proportional to the mean strain rate tensor, S_{ij}, as shown in equation (3.9).

$$\tau_{ij} = 2\mu_t S_{ij} - \frac{2}{3}\rho k \delta_{ij} \tag{3.9}$$

Where, μ_t is a scalar property called the eddy viscosity which is normally computed from the two transport variables. The same equation can be written more explicitly as:

$$-\overline{\rho u_i' u_j'} = \mu_t \left(\frac{\partial U_i}{\partial x_j} + \frac{\partial U_j}{\partial x_i}\right) - \frac{2}{3}\left(\rho k + \mu_t \frac{\partial u_k}{\partial x_k}\right)\delta_{ij} \tag{3.10}$$

The drawback of two equation models is the Boussinesq assumption which is a significant simplification. There might be some complex flows, like flows that are strongly accelerated, strongly rotating flows where Boussinesq assumption is simply not valid. Throughout this study, the standard *k-ε* turbulence model with enhanced wall treatment was chosen. Transport equations for standard k-epsilon model can be derived as [33],

$$\frac{\partial}{\partial t}(\rho k) + \frac{\partial}{\partial x_i}(\rho k u_i) = \frac{\partial}{\partial x_j}\left[\left(\mu + \frac{\mu_t}{\sigma_k}\right)\frac{\partial k}{\partial x_j}\right] + P_k + P_b - \rho\varepsilon - Y_M + S_k \tag{3.11}$$

$$\frac{\partial}{\partial t}(\rho \varepsilon) + \frac{\partial}{\partial x_i}(\rho \varepsilon u_i) = \frac{\partial}{\partial x_j}\left[\left(\mu + \frac{\mu_t}{\sigma_\varepsilon}\right)\frac{\partial \varepsilon}{\partial x_j}\right] + \frac{C_{1\varepsilon}\varepsilon}{k}(P_k + C_{3\varepsilon}P_b) - \frac{C_{2\varepsilon}\rho\varepsilon^2}{k} + S_\varepsilon \tag{3.12}$$

The turbulent viscosity is modeled as,

$$\mu_t = \frac{\rho C_\mu k^2}{\varepsilon} \tag{3.11}$$

Production of k can be written as,

$$P_k = -\rho\overline{u_i' u_j'}\frac{\partial u_j}{\partial x_i} \tag{3.12}$$

$$P_k = \mu_t S^2 \tag{3.13}$$

Where S is the modulus of the mean rate-of-strain tensor, defined as:

$$S \equiv \sqrt{2S_{ij}S_{ij}} \tag{3.14}$$

The model constants used for these equations are,

$$C_{1\varepsilon} = 1.44, \quad C_{2\varepsilon} = 1.92, \quad C_{3\varepsilon} = -0.33, \quad C_{\mu} = 0.09, \quad \sigma_k = 1.0, \quad \sigma_{\varepsilon} = 1.3$$

For turbulent flows, the velocity distribution near the wall can be divided into three distinct regions: the laminar sub layer, buffer region, and log-law region. Due to the no-slip condition at the wall, turbulent flows are greatly affected by the presence of the laminar sub layer. To accurately capture the aspects of this laminar sub-layer an enhanced wall treatment provided by OpenFOAM is used. More details of the near wall treatment can be found in the OpenFOAM user guide [31]. The non-dimensional parameter y^+ needs to be employed for use of the wall treatment. The parameter is defined as:

$$y^+ = \frac{u^* y}{\nu_w} \tag{3.15}$$

Where y is the distance from the wall, and ν_w is kinematic viscosity at the wall. The friction velocity, u^* is defined by:

$$u^* = \sqrt{\frac{\tau_w}{\rho}} \tag{3.16}$$

It has been suggested by many CFD experts in the past that value of y^+ should be less than 5 in order to use the enhanced wall function. Using a certain y^+ the distance of first node from the wall can be estimated approximately and a mesh can be generated accordingly.

All the governing equations derived earlier are in general valid for any Newtonian fluid. To provide closure for a particular fluid, an equation of state (EOS) to model properties of the fluid has to be specified. Most commercial softwares like FLUENT provides a direct link to the National Institute of Standards and Technology (NIST) thermodynamic and transport properties. OpenFOAM uses the ideal fluid equations to model the properties of CO_2 which are invalid in the supercritical region or in the two phase dome. In order to accurately model the properties of CO_2 in OpenFOAM a FIT (Fluid property Interpolation Tables) algorithm was implemented which utilizes a modified version of biquintic spline interpolation method .

Span and Wagner, (1994) [34] developed a new equation of state for CO_2 which is expressed in the form of the Helmholtz energy, *A*, with the two independent variables density, ρ, and temperature, *T*. They expressed the dimensionless Helmholtz energy $\varphi = A/(RT)$ in two parts: the ideal-gas part and the residual real fluid behavior which is expressed as in equation (3.17).

$$\varphi(\delta,\tau) = \varphi^o(\delta,\tau) + \varphi^r(\delta,\tau) \tag{3.17}$$

Where $\delta = \frac{\rho}{\rho_c}$ is the reduced density and $\tau = \frac{T_c}{T}$ is the inverse reduced temperature. Both the density and the temperature were reduced with their critical values. All the thermodynamic properties of a pure substance can be obtained by combining the derivatives of Equation (3.17). The Helmholtz energy of the ideal gas is given by equation (3.18).

$$A^o(\rho,T) = h^o(T) - RT - Ts^0(\rho,T). \tag{3.18}$$

Ideal gas enthalpy, h^0, and the entropy, s^0, can be derived from an equation for the ideal-gas heat capacity, $C_p{}^0$. The final form of ideal gas Helmholtz energy equation can be written as in equation (3.19).

$$A^o = \int_{T_o}^{T} C_p^o dT + h_0^o - RT - T\int_{T_o}^{T} \frac{(C_p^o - R)}{T}\, dT - RT\left[ln\left(\frac{\rho}{\rho_o}\right)\right] - TS_0^o \quad (3.19)$$

Where, subscript indicates the properties at reference state. The final equation for ideal gas part is,

$$\varphi^o = \frac{A^o}{RT} \quad (3.20)$$

$$\varphi^o(\delta,\tau) = ln(\delta) + a_1^o + a_2^o\tau + a_3^o\, ln(\tau) + \sum_{i=4}^{8} a_i^o\, ln[1 - exp(-\tau\theta_i^o)]\,. \quad (3.21)$$

Since, there is no theoretical approach to accurately model the residual part of the Helmholtz energy which is valid in the whole fluid region of a pure substance Span and Wagner modeled the residual part in an empirical way by optimizing its functional form and fitting its coefficients to a large database of experimental results. The actual empirical form of the residual part is quite complicated and the bank of terms which were used in the optimization of the final EOS contained a total of 860 terms. More details about the coefficients in equation (3.21) and the residual part can be found in [33].

From the Helmholtz energy other properties can be calculated based on following thermodynamic relationships in reduced form

$$\frac{P(\delta,\tau)}{\rho RT} = 1 + \delta\varphi_\delta^r \quad (3.22)$$

$$\frac{s(\delta,\tau)}{R} = \tau(\varphi_\tau^o + \varphi_\tau^r) - \varphi^o - \varphi^r \quad (3.23)$$

$$\frac{u(\delta,\tau)}{RT} = \tau(\varphi_\tau^o + \varphi_r^r) \tag{3.24}$$

$$\frac{C_v(\delta,\tau)}{R} = -\tau^2(\varphi_{rr}^o + \varphi_{rr}^r) \tag{3.25}$$

$$\frac{h(\delta,\tau)}{RT} = 1 + \tau(\varphi_\tau^o + \varphi_r^r) + \delta\varphi_\delta^r \tag{3.26}$$

$$\frac{C_p(\delta,\tau)}{R} = -\tau^2(\varphi_{rr}^o + \varphi_{rr}^r) + \frac{\left(1+\delta\varphi_\delta^r-\delta\tau\varphi_{\delta\tau}^r\right)^2}{1+2\delta\varphi_\delta^r+\delta^2\varphi_{\delta\delta}^r} \tag{3.27}$$

Where, $\varphi_\delta = \left[\frac{\partial\varphi}{\partial\delta}\right]_\tau, \delta_{\delta\delta} = \left[\frac{\partial^2\varphi}{\partial\delta^2}\right]_\tau, \varphi_\tau = \left[\frac{\partial\varphi}{\partial\tau}\right]_\delta, \varphi_{\tau\tau} = \left[\frac{\partial^2\varphi}{\partial\tau^2}\right]_\delta, \varphi_{\delta\tau} = \left[\frac{\partial^2\varphi}{\partial\delta\partial\tau}\right]$.

FIT libraries [35] are based on a piecewise biquintic interpolation of Helmholtz free energy. From Helmholtz free energy and all its derivatives as described in equations (3.22 through 3.27), all the other thermodynamic properties are calculated. If the Helmholtz free energy and its derivatives are known at the control points then the interpolated surface can be written as,

$$A(\rho,T) = \sum_{i=0}^{5}\sum_{j=0}^{5} a_{ij}\rho^i T^j \tag{3.28}$$

This representation will result in 36 unknown coefficients and these coefficients can be calculated from a set of equations obtained at the control points. The transport properties like k, α, μ etc. are interpolated independently. The results of the FIT algorithm for CO_2 were compared to REFPROP (Software for fluid properties developed by NIST) and agreed well with a typical error on the order of ~0.01%.

To solve the mass, momentum, and energy equations, the pressure based solver was used along with the SIMPLEC (Semi-Implicit Method for Pressure Linked Equations Corrected) algorithm for pressure-velocity coupling. A second order Gauss upwind scheme was used to solve the governing equations for the simulations performed

on annular orifices and labyrinth seals. For simulations performed on plain orifices a first/second order accurate Gauss van leer scheme was used for better accuracy. More details about these schemes can be found out in a CFD book or the OpenFOAM user guide [31]. The boundary conditions selected for this study were a constant pressure at the inlet and outlet of the seal. A constant enthalpy/temperature boundary condition is used at the inlet.

When the flow expands into the saturation dome, the properties of CO_2 depend on quality and both the phases will be out of equilibrium to some extent traveling at different velocities with different temperatures. In this case the problem becomes complicated and in order to capture the two phase flow field accurately, a separate set of equations have to be developed for both the phases taking into account the properties of each phase. However, for this thesis these complications are eliminated by assuming that there is no slip between phases and that both the phases are in thermal equilibrium. These are the basic assumptions of the "Homogeneous equilibrium model" explained in literature review section. Based on previous work using steam, authors in the past reported that they obtained good results using HEM except for very low quality steam. So, then the question is: "How valid is the HEM for CO_2?"

To answer this question, let us look at figures (3.2 and 3.3). The density ratio of liquid to gas is much smaller for CO_2 compared to that of water in the pressure range of interest. This would imply that slip between liquid and gas is much smaller for CO_2 and relative velocity between phases is not as important as that of water. Hence, it is quite reasonable to assume that both the phases are travelling at same velocities.

Similarly, the ratio of the gas specific heat to the liquid specific heat for CO_2 is comparable to that of water. These two plots indicate that if the HEM works reasonably well for water, it should work much better for CO_2. This is in fact true and will be shown in chapter 4 where some numerical results are compared to the experimental data for plain orifices.

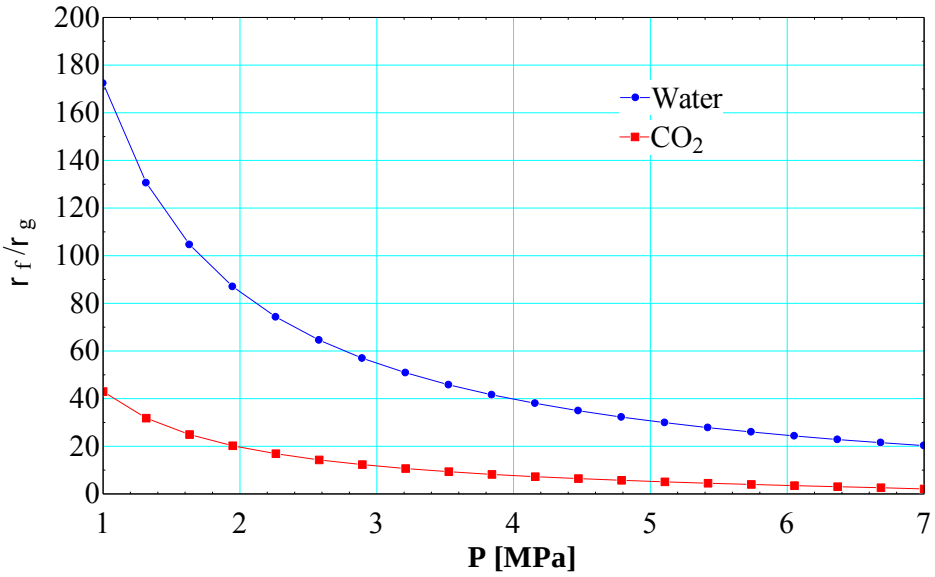

Figure 3.2 Density ratios for two phase CO_2 and water.

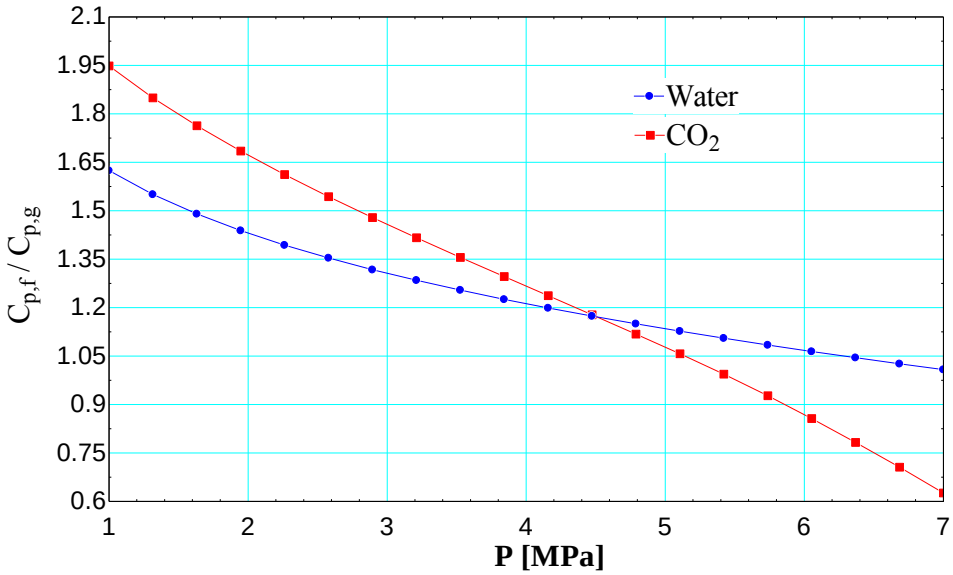

Figure 3.3 Specific heat ratios for two phase CO_2 and water.

CHAPTER IV

NUMERICAL RESULTS

This chapter is divided into three parts; the first part explains the effect of the geometrical parameters, the second part deals with the effect of operating conditions and in third part numerical results obtained for plain orifices are compared to experimental results obtained by the University of Wisconsin, Madison.

4.1 Effect of geometrical parameters on discharge coefficient

In order to understand the effect of geometry on the leakage rate through a labyrinth seal, a single tooth annular orifice was considered for initial study and the results of this study can be extended to multiple tooth labyrinth seal. One of the most important concepts of interest when dealing with Labyrinth seals is the "discharge coefficient". The term "discharge coefficient" describes the total losses that occur as the fluid flows under the tooth and through the cavity.

One Dimensional Isentropic Flow Model for Annular orifices

In the context of labyrinth seals, the flow through an orifice can be modeled as a simple one dimensional isentropic flow, which would ideally give a theoretical maximum flow rate through the orifice. A reduction in flow rate from this isentropic value will always occur as there is always entropy generated due to a real physical flow

processes such as phase change, turbulent dissipation, flow separation and reattachment etc. Furthermore, in a real scenario there will always be more than one dimension involved and 1-D assumptions might not be valid anymore. However, as a matter of convenience to compare complicated flow processes with simple one-dimensional flow, the discharge coefficient (C_d) is defined as,

$$\boldsymbol{C_d} = \frac{\boldsymbol{G_{actual}}}{\boldsymbol{G_{1-D,isentropic}}} \tag{4.1}$$

One dimensional isentropic mass flow rate for an annular orifice can be calculated by performing energy balance across orifice (Figure 4.1) and assuming that flow is isentropic.

Figure 4.1: Generic annular orifice.

1-D isentropic model equations for annular orifices are as follows:

$$h_{down} = h\,(P_{up}, \rho_{up}) \tag{4.2}$$

$$S_{up} = S(P_{up}, \rho_{up}) \tag{4.3}$$

$$S_{down} = S_{up} \tag{4.4}$$

$$h_{down} = h(P_{down}, S_{down}) \tag{4.5}$$

$$h_{up} = h_{down} + \frac{V_{down}^2}{2} \tag{4.6}$$

$$\rho_{down} = \rho(P_{down}, S_{down}) \tag{4.7}$$

$$\dot{m} = \rho_{down} * V_{down} * A_{clearance} \tag{4.8}$$

It can be seen from equations above, that the1-D isentropic model depends only on upstream conditions, downstream conditions as well as clearance area between the shaft and the tooth. It doesn't take into account the effects of tooth width, depth or any other geometrical parameters. These equations are modeled in EES and the 1-D isentropic mass flow rate for case 2 in Appendix A with inlet conditions of 10 MPa, 498 kg/m^3 is shown in figure 4.2.

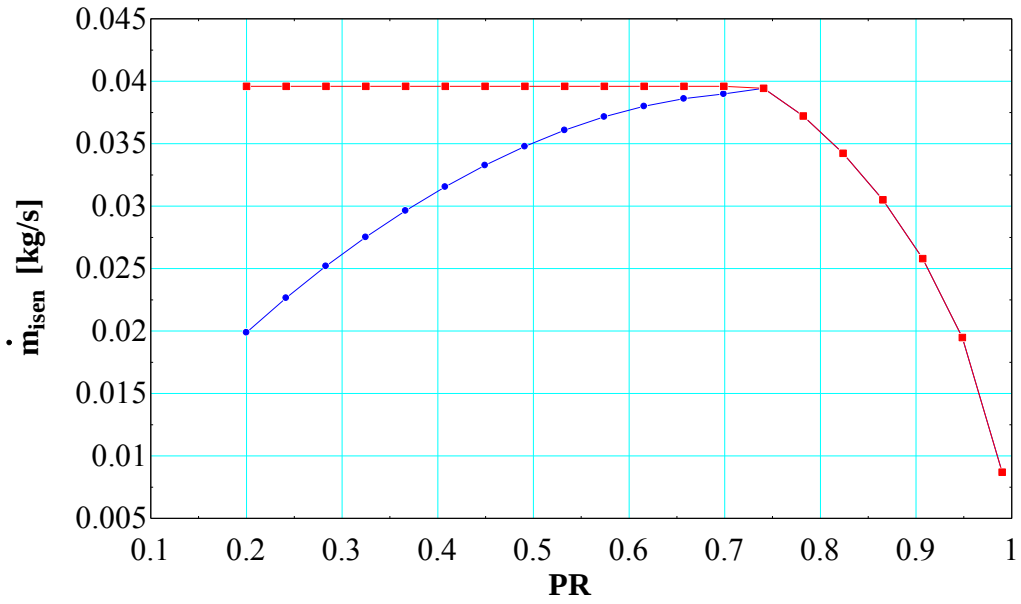

Figure 4.2: 1-D Isentropic mass flow rate calculations.

It can be seen that mass flow-rate increases to a maximum value at a certain Pressure ratio (PR) and then starts decreasing, shown by the blue curve. When the mass flow-rate reaches its maximum value the flow is termed as "choked flow" and the pressure ratio is known as "choked pressure ratio". Choked flow occurs when the velocity of the bulk of particles in flow reaches the sonic condition. The red curve in figure 4.2 shows the actual 1-D isentropic mass flow rate. The choked PR for the isentropic model is calculated by running the calculations through min/max function in EES. Throughout this thesis, the procedure to calculate 1-D isentropic mass flow rate is same as above. In the context of choked flow, there is a difference between choked flow and critical flow. Critical flow results when velocity of any particle in the flow reaches sonic condition. Therefore, according to the definition of choked flow, mass flow-rate should not change after the flow has choked.

The flow is assumed to be axisymmetric and hence a two dimensional (axial-radial) simulation is utilized. Axisymmetric assumption is considered to be good enough to represent flow field as long as the effects of boundary layer in the θ (Azimuthal) direction are negligible. The shaft is represented by a straight wall along the bottom of the domain. Long entrance and exit regions are used before and after the annular orifice to allow for the flow to equilibrate before it enters the tooth clearance. This would represent real geometry which would be used in experiments. A sample mesh (for case 2 in Appendix A) is shown in Figure 4.3. The mesh is created using the blockMeshDict utility provided by OpenFOAM which translates a set of well-defined coordinates and blocks into a mesh. In Figure 4.3 it can be seen that, the computational mesh is much

finer in the clearance region. Care has been taken to make sure that value of Y^+ for nodes very close to the tooth and shaft walls is less than 5 in order to resolve the laminar sublayer. The mesh is also generated to follow the flow and hence is non-orthogoanl to the surface of tooth outside clearance region. Error due to this non-orthogoanlity is minimized by performing non-orthogonal corrections after every iteration.

Before looking at the effects of various geometrical parameters on leakage through annular orifice, it was necessary to perform a grid independence study to make sure that results obtained from the computational studies are independent of mesh. Since, OpenFOAM doesn't have the capabilities to refine the mesh based on the gradient in variables, the mesh was subjected to various levels of manual refinement.

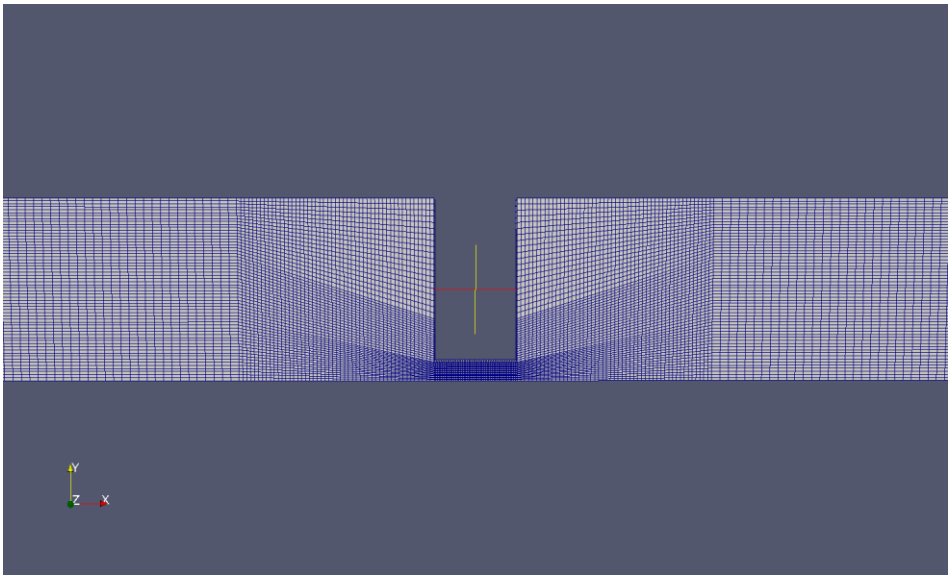

Figure 4.3: A sample computational mesh used for simulations.

Results of the grid independence studies are presented in Figures (4.4 and 4.5). The leakage rate prediction error between the mesh with 20000 nodes and the orthogonal mesh with 50000 nodes was about 3 % for higher pressure ratios and less than 0.6 % for lower pressure ratios. This error at higher pressure ratios might slightly effect the prediction of C_d as shown in Figure 4.3. The error between the mesh with 30000 nodes and that of orthogonal mesh is about 1 % for higher pressure ratios and less than 0.3 % for lower pressure ratios. Hence, the mesh with 30000 nodes is employed for computational studies on the annular orifice.

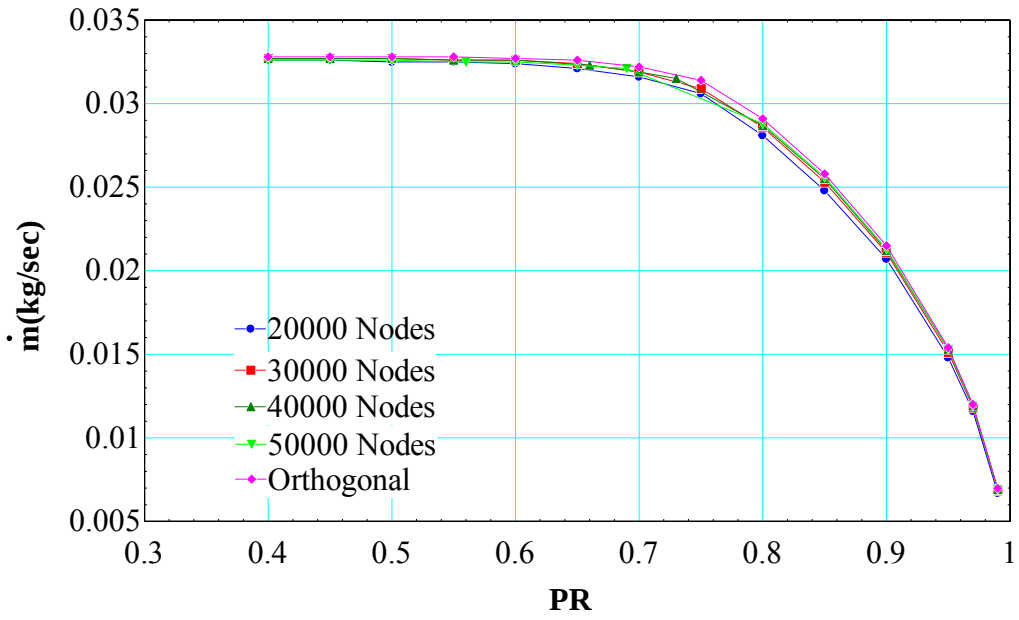

Figure 4.4: Variation of leakage rate prediction with number of nodes.

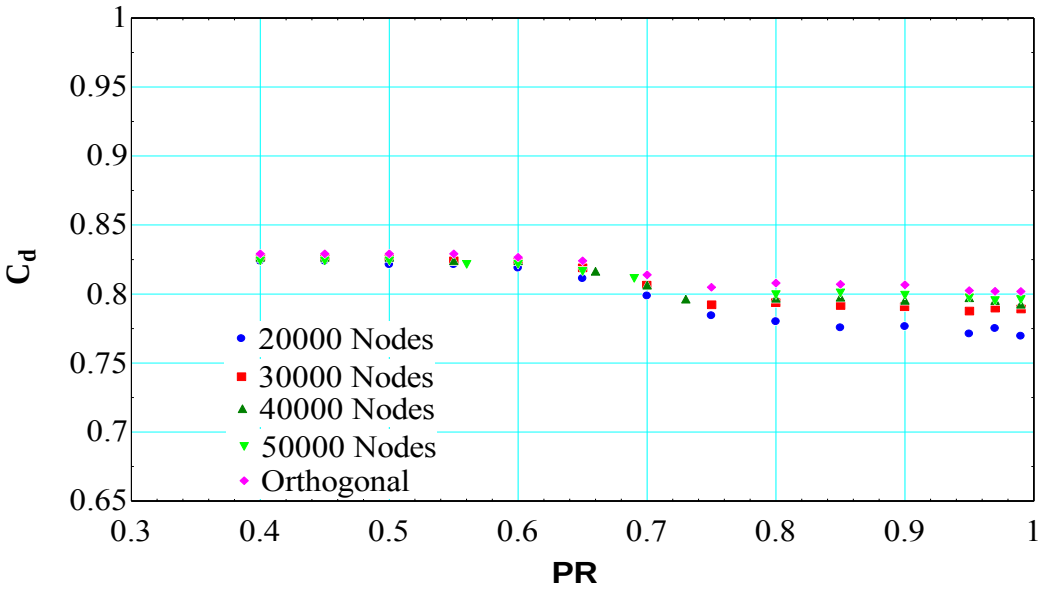

Figure 4.5: Variation of discharge coefficient with number of nodes.

As mentioned earlier in the literature review section, there are various geometrical factors affecting discharge through orifices. Some of the important parameters which will be analyzed in this section are the effects of radial clearance, tooth width, tooth depth, inlet radius of curvature, shaft diameter.

4.1.1 Effect of radial clearance

The first parameter that is of interest when designing seals for turbo-machines is the radial clearance. Simulations were performed for four different radial clearances (cases 1-4 in Appendix A) with the rest of the geometrical parameters held constant for all four cases. The leakage rate is calculated by integrating the mass flow at each node of the inlet and scaling the 2-D axisymmetric mass flow rate to a 3-D model. Then the discharge coefficient is predicted by calculating the ratio of this scaled mass flow rate

with respect to the 1-D isentropic mass flow rate. Figures (4.6 and 4.7) present the results of the leakage rates and discharge coefficients respectively for all four cases.

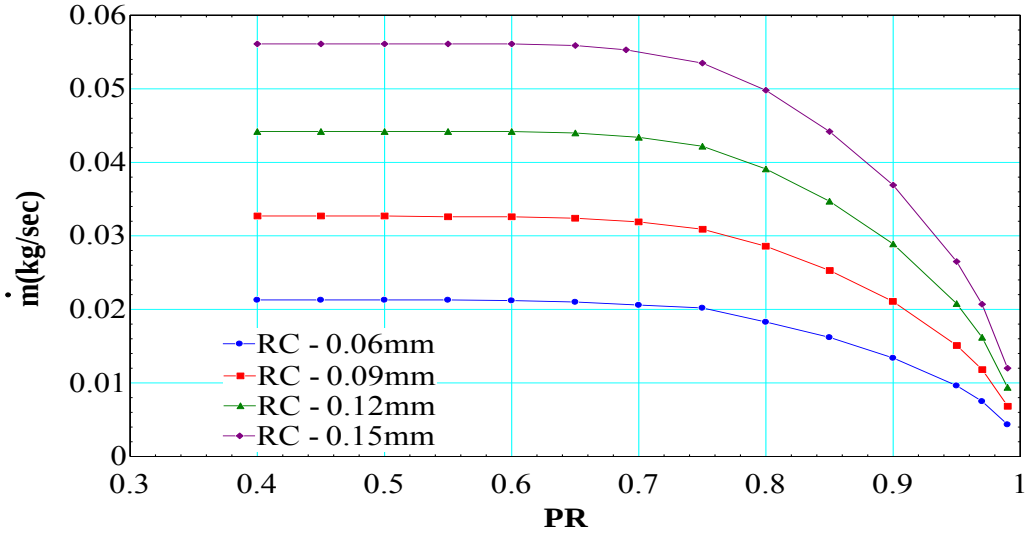

Figure 4.6: Variation of leakage rate with radial clearance.

The leakage rate increases with an increase in radial clearance, which is a fairly obvious result as an increase in clearance area allows more fluid to be forced underneath the tooth. It should be noted that the inlet operating condition for all these simulations is fixed at a pressure of 10 MPa, and a density of 498 kg/m^3. Although the leakage rate increases by a magnitude of approximately 3 times between the clearances of 0.06 mm and 0.15 mm, it is interesting to note that the discharge coefficient for all the four cases doesn't vary by much.

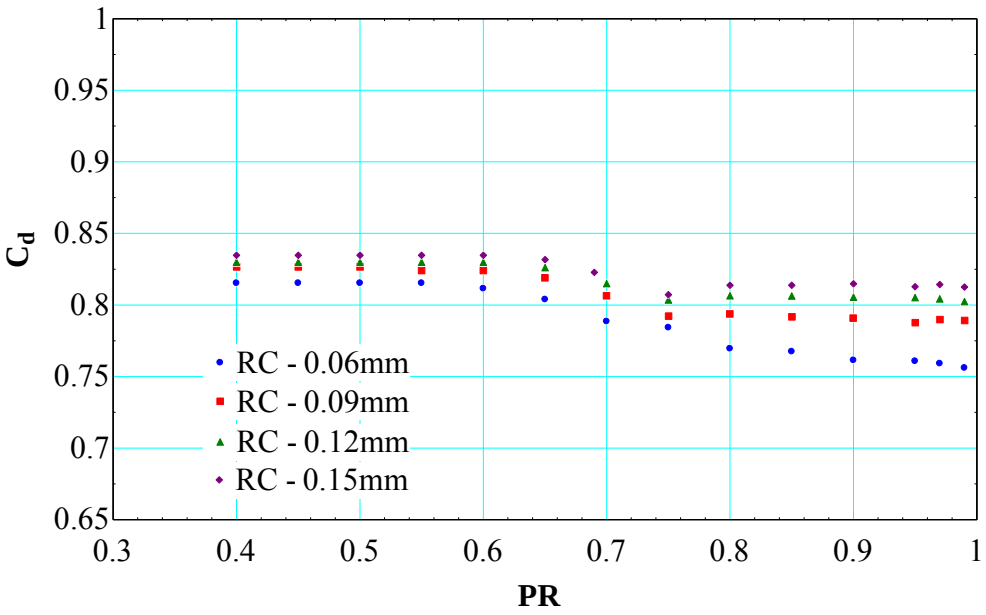

Figure 4.7: Variation of discharge coefficient with radial clearance.

This result implies that the 1-D isentropic model is able to predict the leakage rate for all radial clearances equally well. One more interesting thing to note is how the C_d remains constant for higher PR's, increases over a certain range of PR and stays constant below the choked PR. The reason for this increase in C_d over a range of PR is due to the fact that the 1-D isentropic model and real flow choke at different PR's. In reality, the mass flow rate continues to increase even after the 1-D isentropic model chokes and hence, the C_d increases till the real flow chokes and stays constant after that.

4.1.2 Effect of tooth width

To understand the effect of tooth width on the C_d, simulations were performed for three different tooth widths while holding rest of the geometrical parameters constant (cases 2, 5 and 6 in Appendix A). Figures (4.8 and 4.9) present the results of the leakage rates and discharge coefficients respectively for all three cases.

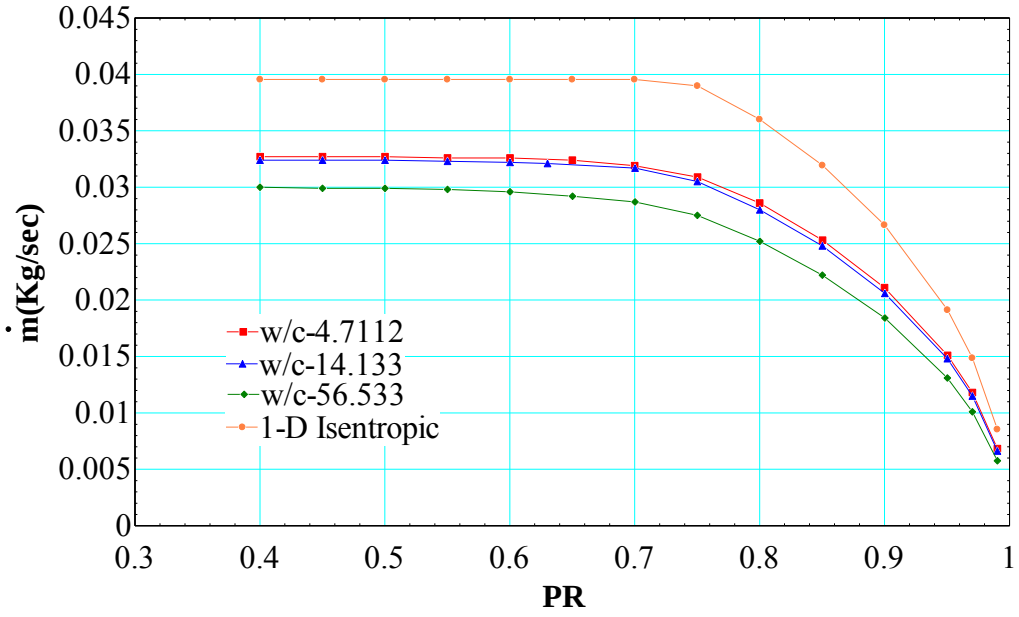

Figure 4.8: Variation of leakage rate with tooth width.

It can be seen that smaller *w/c* (width to clearance) result in higher leakage rate and as a result, the discharge coefficients are higher for the lower *w/c* cases. As the flow enters the clearance region, fluid separates from the tooth edge and forms a recirculation zone in the clearance region until the flows reattaches back to surface. The fluid stream reaches a minimum diameter where radial velocity is zero before reattaching to the

surface again. The point where fluid stream has least diameter is termed as "vena contracta". The Coefficient of contraction (C_c) can be defined as in equation (4.9)

$$C_c = \frac{Area\ at\ vena\ contracta}{Area\ of\ orifice} \tag{4.9}$$

The typical value of C_c is 0.64 for a sharp orifice. The smaller the value of C_c, the more effective the vena contracta is. After the flow reattaches to the surface the pressure drop in the orifice can be treated equivalent to a flow through pipe. In the case of laminar pipe flow for a given pressure drop the flow rate gets smaller as the length of the pipe increases, as shown in equation (4.10). This can be extended to complicated turbulent flow and said that the leakage rate is inversely proportional to the tooth width.

$$Q = \frac{\pi D^4 \Delta P}{128 \mu l} \tag{4.10}$$

As presented in figure 4.9, C_d doesn't change much for lower *w/c* cases. If the fluid reattaches to the surface of tooth very close to the downstream edge, the effect of tooth width might not be very significant, as observed for lower *w/c* cases. As *w/c* increases the effect of tooth width becomes more and more significant. In fact, while understanding the effect of radial clearance, *w/c* for the least clearance (0.06mm) case is about 7.06 whereas for the maximum radial clearance (0.15mm) case it is about 2.82 which is the reason why the discharge coefficients didn't vary much even though the leakage rates increased by 3 times between minimum and maximum clearance cases. It has been shown by many authors [28] in the past that the major non-dimensional parameter influencing the discharge coefficient is *w/c*.

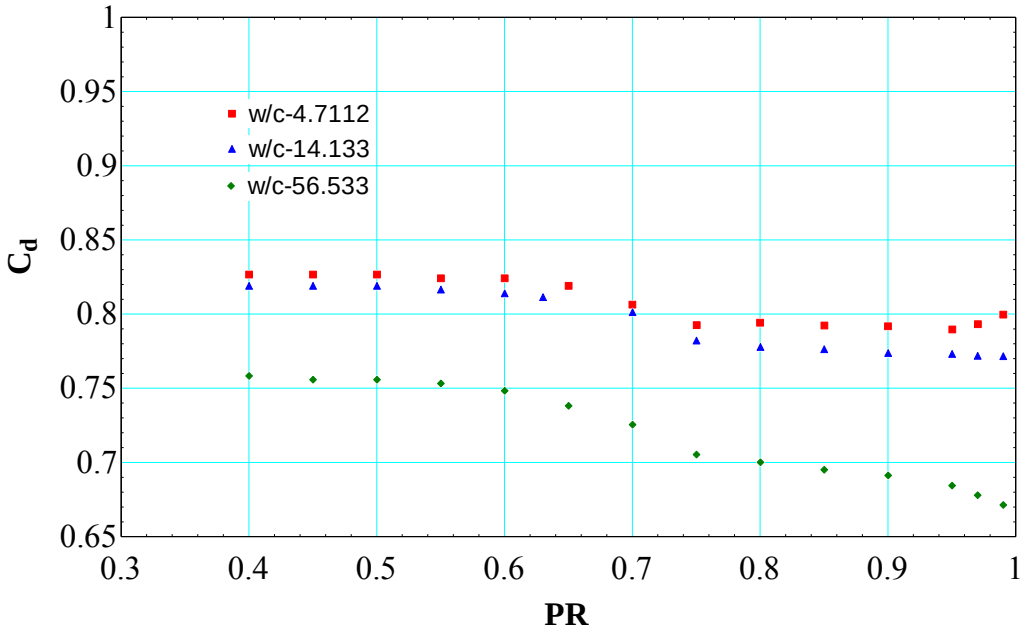

Figure 4.9: Variation of C_d with tooth width.

In order to reassert the theory that *w/c* is the only geometrical parameter that significantly affects the discharge coefficient of an annular orifice, two simulations were performed with different widths and clearances but having the same *w/c* (cases 2 and 7 in Appendix A). Figure 4.10 indicates that the discharge coefficient of both the cases show nearly the same functional relationship with PR thus verifying that *w/c* is the correct non-dimensional geometrical parameter that influences the discharge coefficient of an annular orifice. It might also be worthwhile to affirm the theory at higher *w/c* of 56.533 or above, which is left to be part of future work.

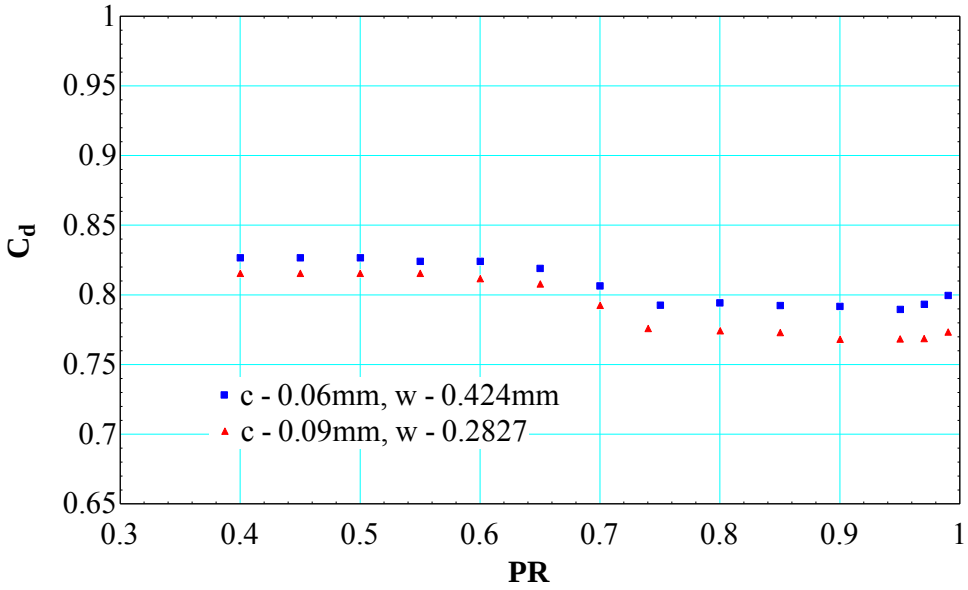

Figure 4.10: C_d of annular orifices having same *w/c*.

4.1.3 Effect of tooth height

In order to examine the effects of tooth height, simulations are performed for 3 different tooth heights (cases 2, 8 and 9 in Appendix A) while holding the other geometrical parameters constant. The results for leakage rate and C_d are presented in figures 4.11and 4.12. It can be shown using the Bernoulli equation that, for an incompressible fluid as tooth height decreases, the total head loss from inlet to exit of an orifice decreases. This implies that the leakage rate will be higher for a given pressure drop. This theory can be extended to complicated turbulent flows and it can be concluded that the leakage rate increases as tooth depth decreases as seen in figure 4.11.

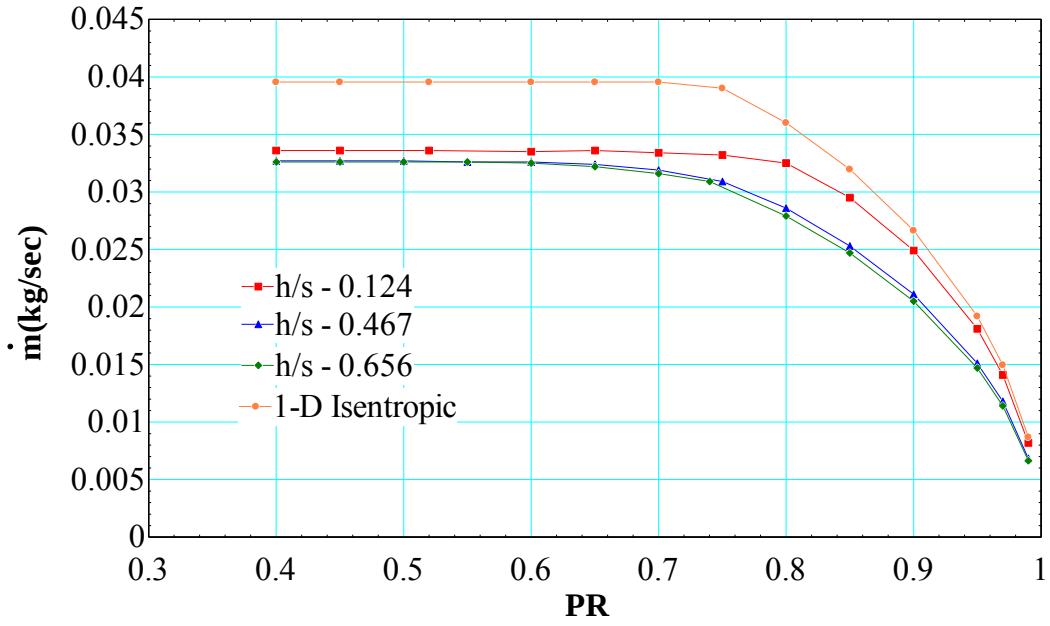

Figure 4.11: Variation of leakage rate with tooth height.

It is interesting to note that the C_d for lower tooth height case is higher for higher PR's and decreases over a certain PR and stays constant after 1-D isentropic flow chokes. This trend is quite opposite to what other cases present. This is due to the real flow choking before the 1-D isentropic flow chokes and hence isentropic flow rate keeps increasing even after the real flow chokes. The physical reason behind why the real flow chokes before the isentropic flow is unknown at this point and requires more detailed study. As tooth height increases, discharge coefficient is nearly independent of tooth height and can be assumed that it has no effect on C_d. It has to be noted that the aspect ratio of cavities of most real world labyrinth seals is over 0.5 and rarely exceeds 1.5.

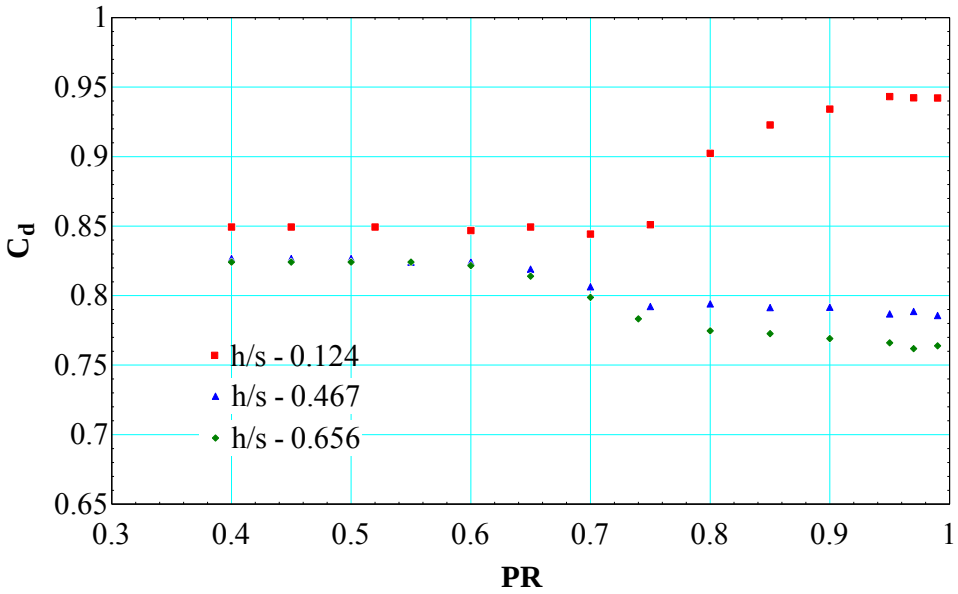

Figure 4.12: Variation of C_d with tooth height.

4.1.4 Effect of shaft diameter

It can be observed from figure 4.13 that the C_d of annular orifice doesn't change with shaft diameter, even after increasing the shaft diameter to 3 times the initial value (Cases 2 and 10 in Appendix A). Hence, it can be concluded that shaft diameter does not influence the value of C_d and a model which is developed for a particular shaft diameter can be applied to any shaft diameter.

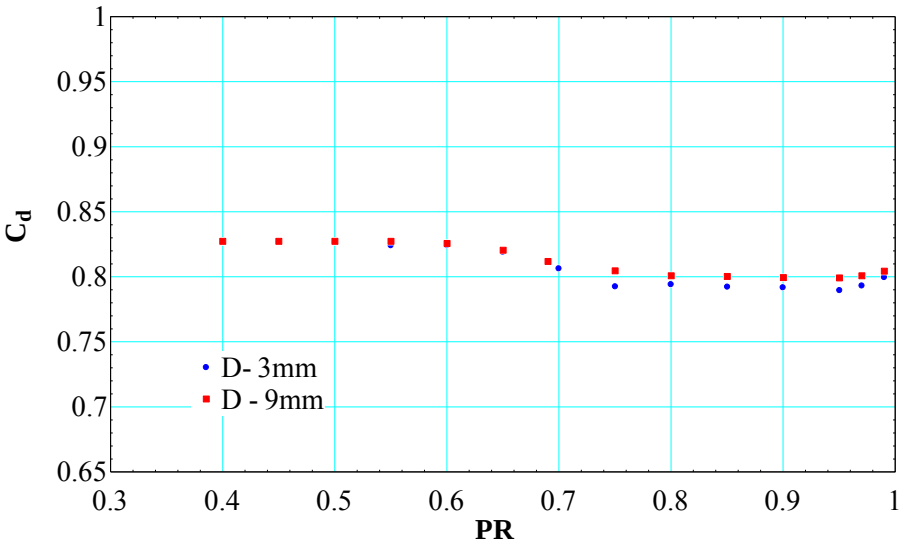

Figure 4.13: Variation of C_d with shaft diameter.

4.2 Effect of geometrical parameters on carryover coefficient

As described by Hodkinson [28], leakage rate through a labyrinth seal can be estimated as,

$$\dot{m} = \alpha\gamma\dot{m}_{ideal} \tag{4.11}$$

Where $\dot{m}_{ideal}$ is the 1-D isentropic flow rate for labyrinth seals, γ is the carryover coefficient of the cavity, α is the flow coefficient similar to discharge coefficient.

Following the definition presented by Hodkinson, γ is calculated as a function of the divergence angle, β, measured from the streamline separating the fluid recirculating in the seal cavity and that passing under the tooth. The carryover coefficient can be calculated based on following relationships provided by Hodkinson.

$$\gamma^2 = \frac{1}{1-\chi} \tag{4.12}$$

$$tan\,\beta = c\frac{(1-\chi)}{\chi s} \tag{4.13}$$

The divergence angle, β, is the angle made between the line connecting the lip of the upstream tooth to the point of impingement of the jet onto the downstream tooth and a line parallel to the rotor surface. Radial velocity data is collected along the downstream tooth surface and the point where radial velocity is zero is taken as the point of impingement of the jet, as shown in figure 4.14. The cavity geometrical parameters are varied (single parameter is varied at a time) and model for carryover coefficient is developed to include the geometrical effects.

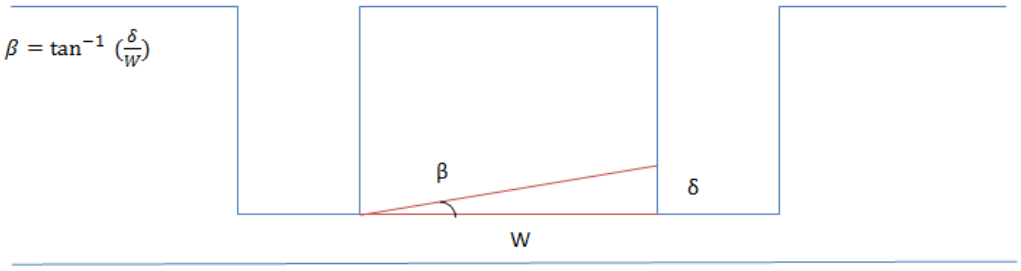

Figure 4.14: Measurement of divergence angle in the cavity.

4.2.1 Effect of radial clearance

Hodkinson [25] used, the clearance to pitch ratio (*c/s*) as the only non-dimensional parameter to develop an empirical correlation for γ based on geometry. Four cases are simulated for fixed pitch but with varying clearance (cases 1-4 in Appendix B). The carryover coefficient for each of these cases is calculated and the results are presented in figure 4.15.

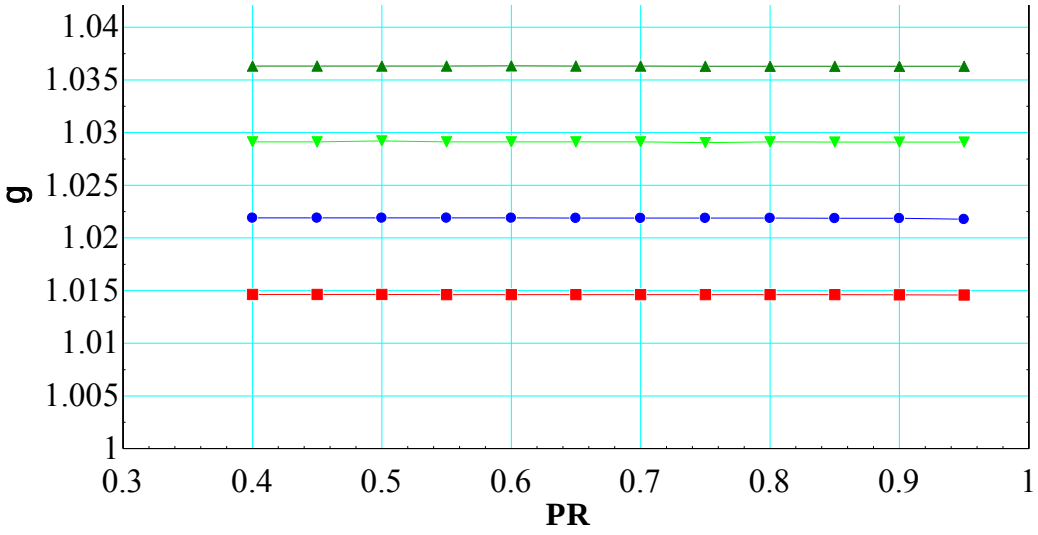

Figure 4.15: Effect of clearance on γ.

It is very important to note that γ is not a function of PR and stays constant for a fixed clearance to pitch ratio. A higher value of *c/s* results in higher carryover coefficient as, for a given jet divergence more fluid flows under the tooth when the clearance is higher. However, increasing the clearance by a factor of 2.5 increases the carryover

coefficient by only 2%. Based on these results, the carryover coefficient can be written as shown in equation (4.14).

$$\gamma = 0.3948\left(\frac{c}{s}\right) + 1.001 \tag{4.14}$$

4.2.2 Effect of tooth height on carryover coefficient

Changing the tooth height to pitch ratio (*h/s*) changes the aspect ratio and could possibly have some effect on recirculation in the cavity. To verify if changing the aspect ratio of the cavity affects the carryover coefficient or not, three simulations were performed by varying the cavity depth while leaving other geometrical parameters constant (cases 9, 10 and 11 in Appendix B). It can be seen from figure 4.16 that the carryover coefficient is independent of *h/s*. Therefore, the conclusions from these simulations is that tooth height or cavity height has no effect on the kinetic energy carryover coefficient, which is one of the basic assumptions made by Hodkinson [28].

As the cavity depth decreases it is expected that the intensity of turbulence dissipation in the cavity increases thereby decreasing the leakage rate through the seal. As shown in figure 4.17 (cases 2, 9, 10 and 11 in Appendix B), the leakage rate decreases as the cavity height decreases due to the phenomenon explained above. However, it has been shown earlier that cavity depth doesn't have any effect on carryover coefficient which would imply that the effect of change in cavity depth has to be modeled into the flow coefficient, α, described in equation (4.11).

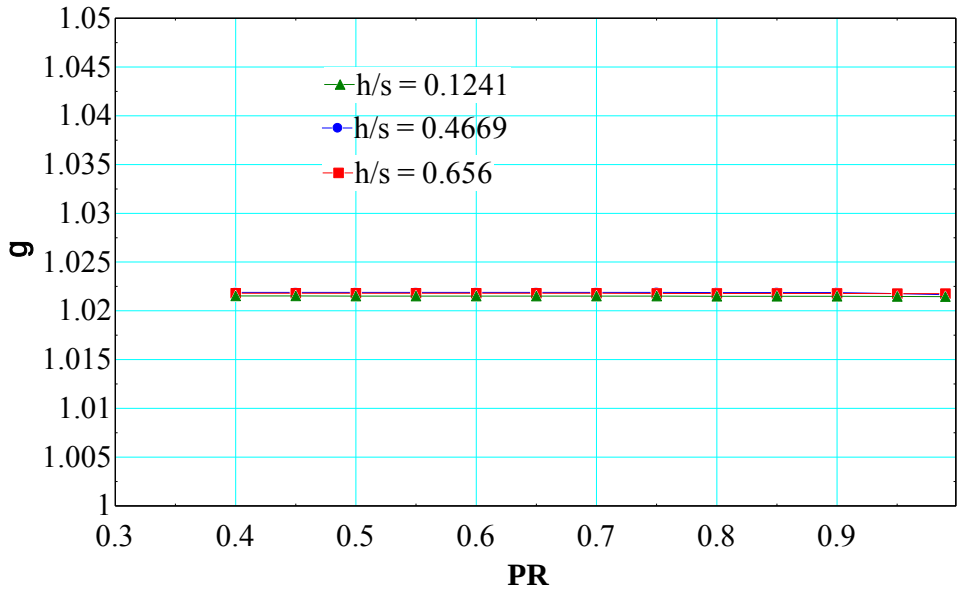

Figure 4.16: Effect of tooth/cavity height on γ.

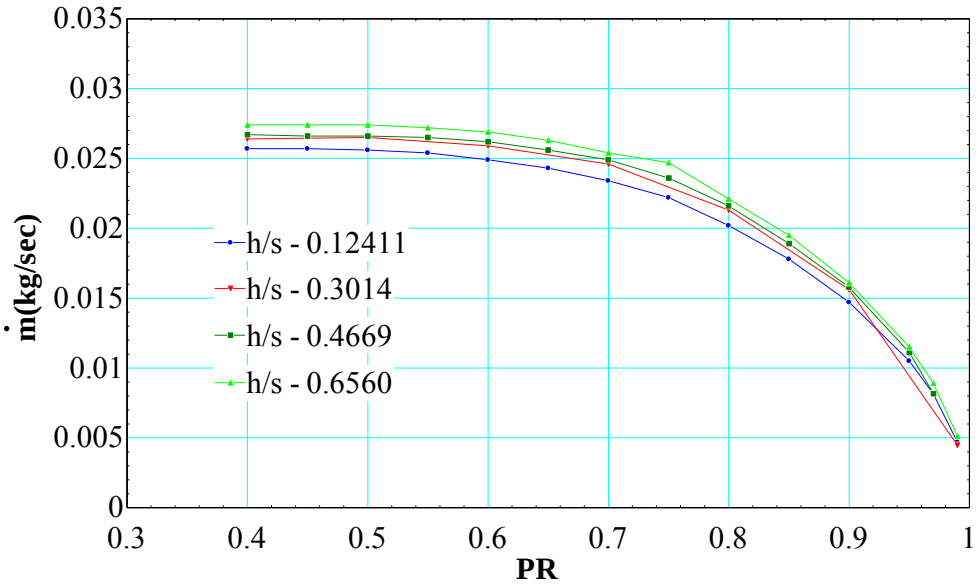

Figure 4.17: Effect of cavity height on leakage rate.

4.2.3 Effect of cavity width on carryover coefficient

The vortex pattern of the flow field varies with cavity width. It is expected that, as the width of the cavity increases the intensity of the vortex pattern increases causing a reduction in the leakage rate as shown in figure 4.18. (Cases 1, 5, 6, 7 and 8 in Appendix B) and figure 4.19 show the variation of carryover coefficient for these cases.

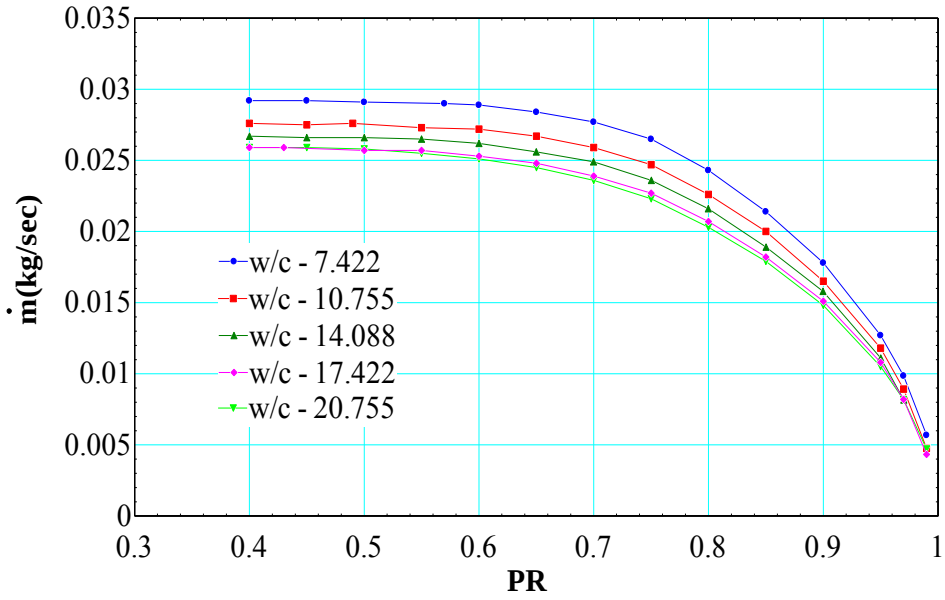

Figure 4.18: Effect of cavity width on leakage rate.

It can be seen that as *w/c* increases the carryover coefficient increases whereas the leakage rate decreases. These are two contradictory results which could be due to the fact that the discharge coefficient of any tooth with a preceding cavity is different from that of a single tooth without any preceding cavity as in the case of annular orifices.

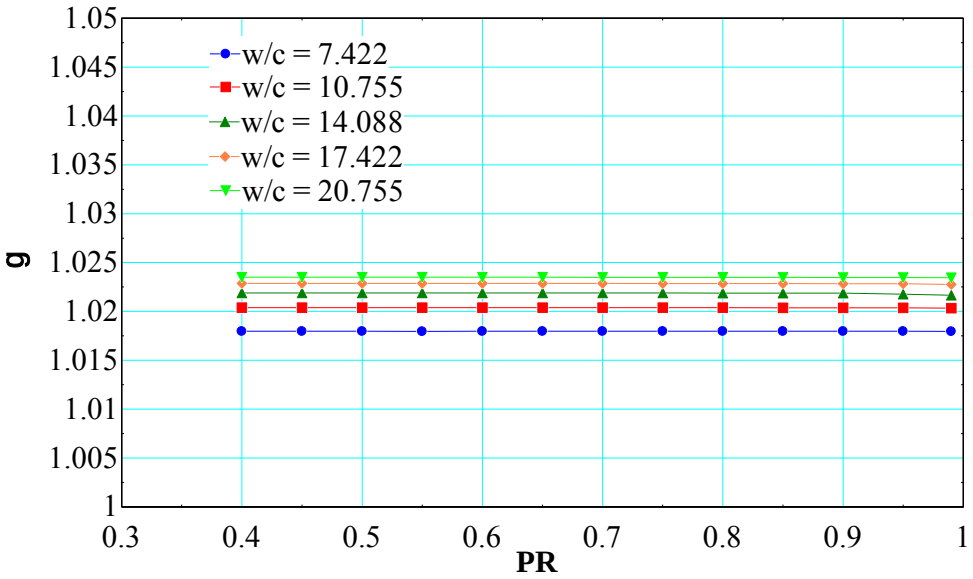

Figure 4.19: Variation of γ with cavity width.

So, the discharge coefficient of the first tooth in a multiple tooth labyrinth seal is similar to that of an annular orifice since it doesn't have any preceding cavity whereas the discharge coefficient from the second tooth will be a function of the discharge coefficient of the previous tooth and the carryover coefficient as shown in equation (4.15)

$$C_d^{n\ tooth} = f(C_d^{n-1\ tooth}, \gamma) \tag{4.15}$$

This can be proved by analyzing the velocity profiles at the entrance of each tooth in a three teeth labyrinth seal (Case 1 in Appendix B). Figure 4.20 indicates that the velocity profile at the entrance of each tooth is different. It is interesting to note that velocities at the entrance of last tooth are much higher than that of previous teeth which is due to the pressure drop being largest for the last tooth which will be shown later.

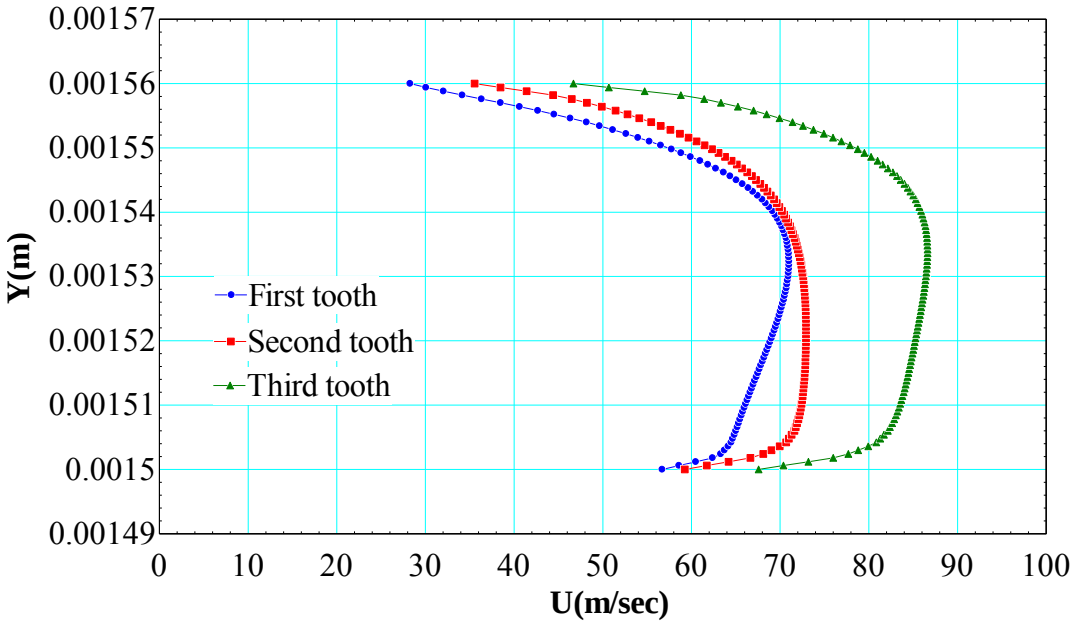

Figure 4.20: Velocity profile at the entrance of each tooth.

Taking into account the effect of cavity width, equation (4.14) is modified and model for γ is developed with *c/s*, *w/c* as the non-dimensional parameters.

$$\gamma = 0.91559 + \left[0.395745 + 0.113839\left(\frac{w_{cavity}}{c}\right)\right]\left(\frac{c}{s}\right) \qquad (4.16)$$

4.2.4 Effect of shaft rotation on annular orifices and labyrinth seals

A rotating shaft may change the flow pattern within the seal as it introduces swirl velocity. The speed of the shaft might influence the discharge coefficient and the carryover coefficient of flow through a labyrinth seal. Literature often presented contradictory results with some studies indicating that the shaft rotation reduced leakage rate whereas some studies showed that leakage rate increases due to shaft rotation. A report by Sandia National Laboratories (SNL) [8] indicated that shaft rotation has no

influence on the leakage rate even for speeds as high as 65,000 rpm. To analyze this effect, simulations are performed for a fixed operating condition and seal geometry at different shaft speeds. First, results will be presented for discharge through annular orifices and then for labyrinth seals.

The results for annular orifices are presented in figure 4.21 (cases 2, 11-16 in Appendix A) and it can be seen that for a low pressure ratio shaft rotation has nearly no influence on C_d. This is in good agreement with the results from SNL. However, at higher PR there is a drastic increase in C_d as shown in figure 4.21. The induced radial velocity due to shaft rotation increases as the shaft speed increases and is nearly independent of PR. The reason for the drastic increase in C_d might be due to the fact that induced radial velocities are comparable to axial velocities at higher PR's.

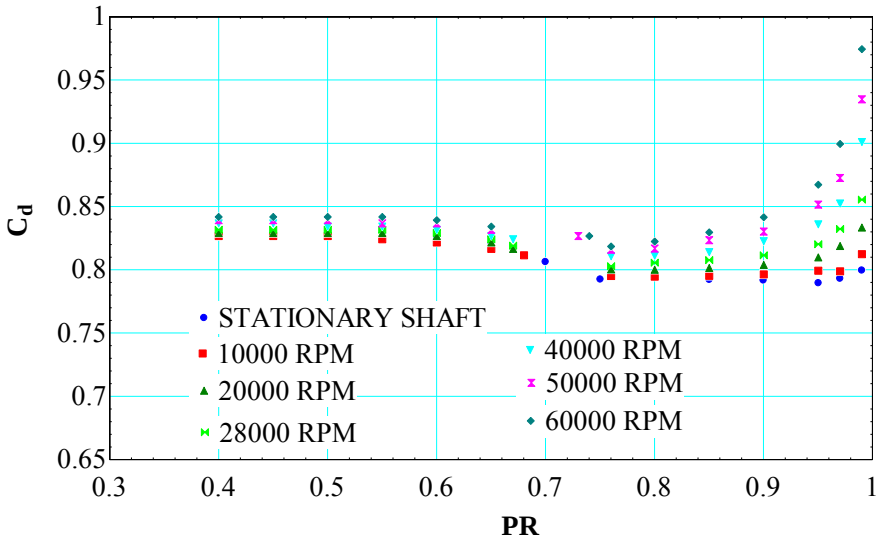

Figure 4.21: Influence of shaft rotation on C_d of annular orifice.

The conceptual discharge coefficient for labyrinth seals is calculated with respect to the 1-D isentropic model for annular orifices to facilitate a direct comparison with the annular orifice data. The conceptual discharge coefficient for labyrinth seals is defined as shown in equation (4.17)

$$C_d|_{labyrinth-seal} = \frac{\dot{m}_{simulation}}{\dot{m}_{1-D,isentropic}} \tag{4.17}$$

The Conceptual C_d can be considered as an effective discharge coefficient of a labyrinth seal and will be a function of the C_d through an annular orifice having dimensions that of the tooth and carryover coefficient from the cavity.

It has been observed that shaft rotation has no effect on the carryover coefficient as shown in figure 4.22 and hence the conceptual C_d of a labyrinth seal as shown in figure 4.23 (cases 2, 12-16 in Appendix B) presents a similar trend as that of an annular orifice.

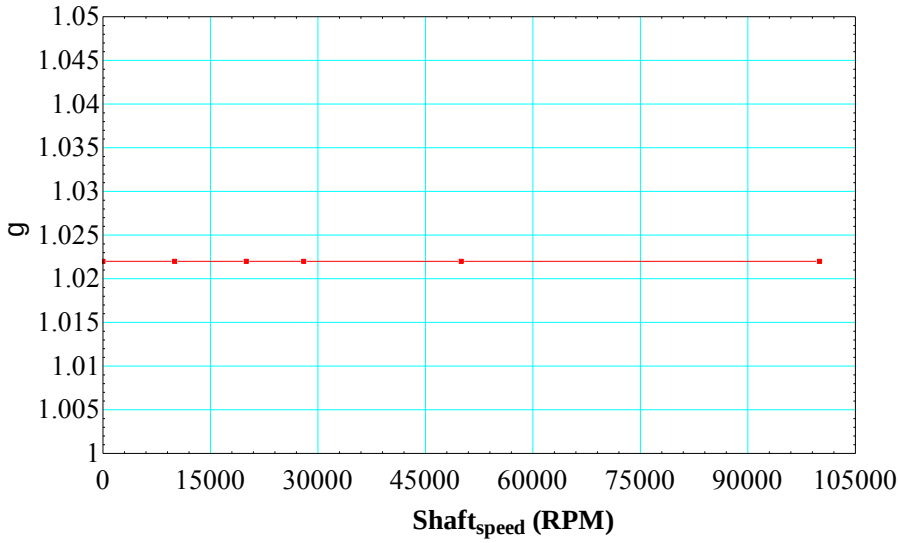

Figure 4.22: Variation of γ with shaft speed.

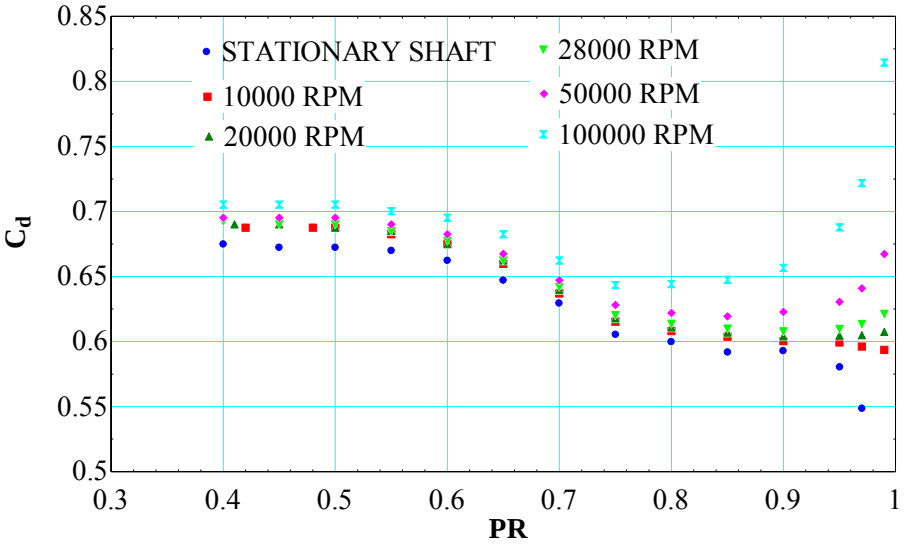

Figure 4.23: Variation of the conceptual C_d with shaft speed.

This would imply that it is sufficient to model the influence of shaft rotation into C_d of an annular orifice. However, at these high shaft speeds, the influence of boundary layer in the θ direction might be significant and it is good practice to validate some of these results against a 3-D model or experimental data for an annular orifice, which is left as a part of future work.

To predict leakage through labyrinth seal, each tooth can be treated individually and leakage rate equation for each tooth can be written as,

$$\dot{m} = C_d|_{ntooth}\gamma\dot{m}_{isentropic} \tag{4.18}$$

Where C_d of the first tooth is same as that of an annular orifice and C_d from the second tooth depends on the C_d of previous tooth and γ of the cavity. For first constriction γ is equal to 1. A correlation for γ is developed earlier in this section. In future, it is proposed to develop a correlation for the discharge coefficient which can be applied to each tooth

as in equation (4.18). This would result in a set of equations equal to the number of teeth in a labyrinth seal. These equations can be solved simultaneously to obtain the pressure drop across each tooth and the leakage rate through the labyrinth seal.

It has been found out that a 1-D isentropic model assuming that $C_d = 1$ and $\gamma =$ 1is good enough in predicting the leakage rate through labyrinth seals as shown below. One Dimensional Isentropic flow model for Labyrinth seals:

The ideal leakage rate through a labyrinth seal (figure 4.24) can be calculated by assuming that the carryover coefficient ($\gamma = 1$) in cavity, which means that the kinetic energy of the jet expanding from the tooth is completely dissipated in following cavity.

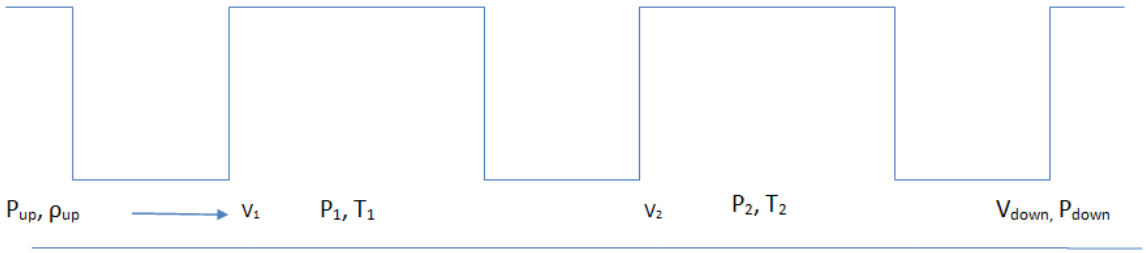

Figure 4.24: Generic labyrinth seal

The 1-D isentropic model equations for Labyrinth seals are as follows:

$$S_{up} = S(P_{up}, \rho_{up}) \tag{4.19}$$

$$S_{up} = S_1 = S_2 = S_{down} \tag{4.20}$$

$$h_{up} = h(P_{up}, \rho_{up}) \tag{4.21}$$

$$h_1 = h(P_1, S_1),\ \rho_1 = \rho(P_1, S_1) \tag{4.22}$$

$$h2 = h(P_2, S_2),\ \rho_2 = \rho(P_2, S_2) \tag{4.23}$$

$$h_{down} = h(P_{down}, S_{down}),\ \rho_{down} = \rho(P_{down}, S_{down}) \quad (4.24)$$

$$h_{up} = h_1 + \frac{V_1^2}{2} \quad (4.25)$$

$$h_1 = h_2 + \frac{V_2^2}{2} \quad (4.26)$$

$$h_2 = h_{down} + \frac{V_{down}^2}{2} \quad (4.27)$$

$$\dot{m}_{ideal} = \rho_1 A_{clearance} V_1 = \rho_2 A_{clearance} V_2 = \rho_{down} A_{clearance} V_{down} \quad (4.28)$$

The Above set of equations are modeled in EES and solved simultaneously to obtain 1-D isentropic leakage rate for labyrinth seals without carryover. Although, the equations presented here are for three teeth cases, these equations can be extended to a labyrinth seal with any number of teeth. The behavior of this model is quite similar to that of an annular orifice model. The isentropic leakage rate increases until the choking PR and then starts decreasing. Again, these calculations are run through min/max function in EES and the modified leakage rate will be used for multiple teeth cases as well. The model assumes temperature and pressure to be constant across the cavity in the radial clearance region. The question now is: "How valid is this assumption?"

To answer this question, temperature and pressure in the radial clearance region are plotted for one of the cases (Case 1 in Appendix B). From figure 4.25 it can be observed that for a pressure drop as high as 6 MPa, pressure remains fairly constant throughout the cavity. It can also be seen from figure 4.26 that temperature also follows the same trend. It is also interesting to note that majority of the pressure and temperature drop occurs across the last tooth. This would imply that leakage rate through labyrinth seal is dictated by the C_d of last tooth.

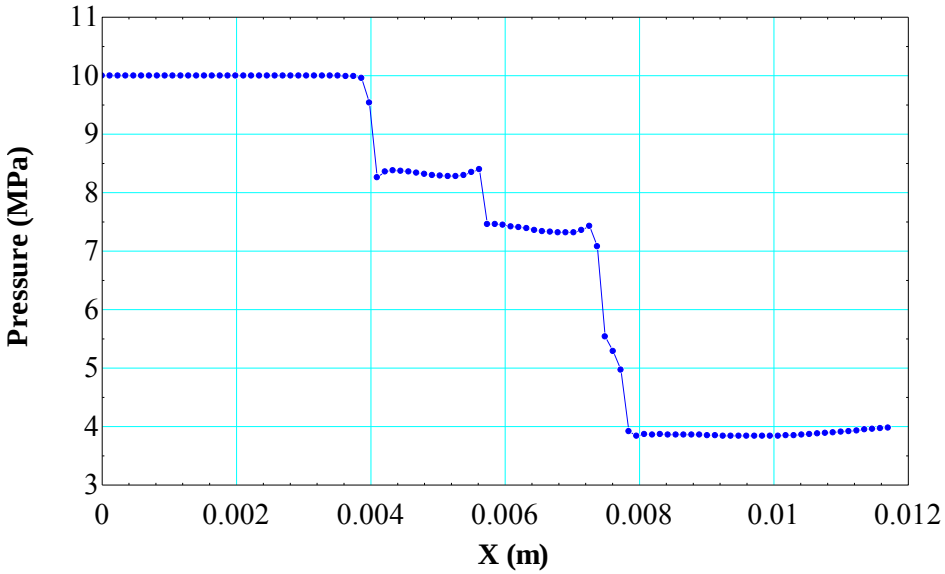

Figure 4.25: Pressure variation along centerline in the radial clearance region.

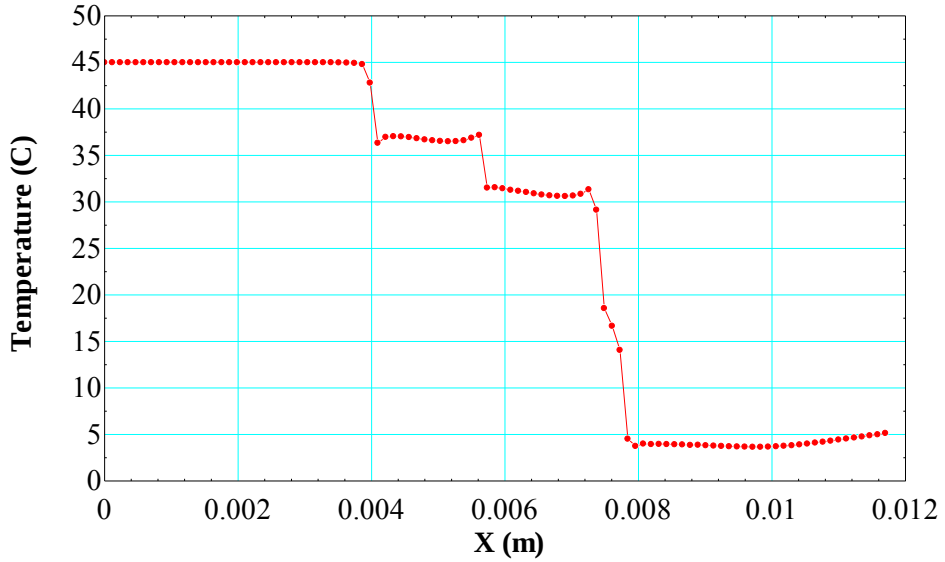

Figure 4.26: Temperature variation along centerline in the radial clearance region.

The 1-D isentropic model for labyrinth seal, described above is applied to case 2 in Appendix B. From figure 4.27, it can be seen that a simple 1-D isentropic model for

labyrinth seals assuming the C_d and the γ are equal to 1, works reasonably well in predicting leakage through multiple constrictions. The drawback of this 1-D isentropic model is that it doesn't take into consideration the geometrical parameters of labyrinth seals and is only dependent on the number of constrictions and radial clearance.

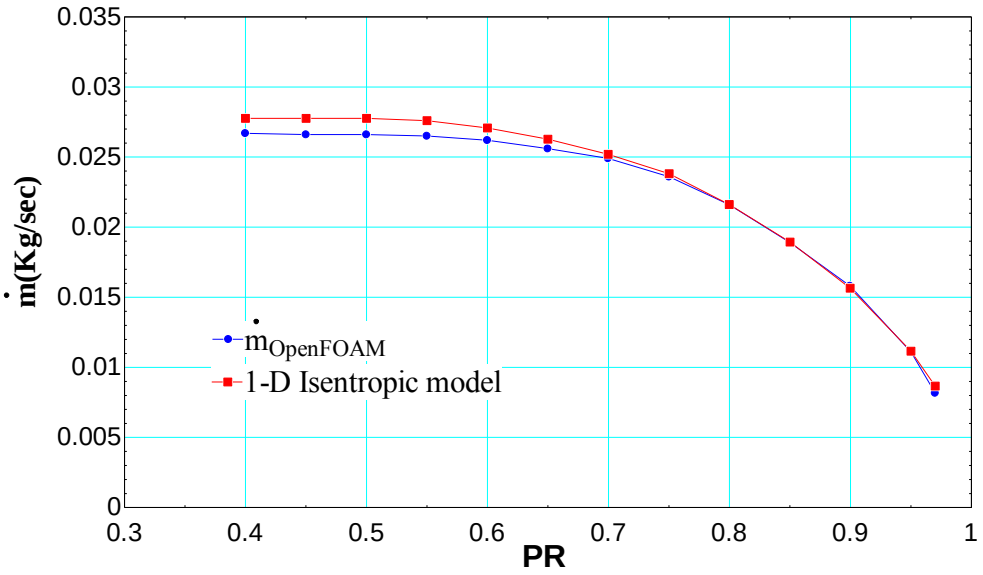

Figure 4.27: Leakage rate prediction using 1-D isentropic model for case 2 in Appendix B.

4.3 Effect of operating conditions

The previous section explained the effects of geometrical parameters while holding the inlet operating condition constant at 10 MPa, 498 kg/m^3. In this section we will look at the effect of operating conditions without changing geometry. First, the effect of operating conditions on an annular orifice will be studied and then the theory will be extended to labyrinth seals. Before even performing simulations, a simple 1-D isentropic model for annular orifices is used to understand the effects of operating conditions.

According to the 1-D isentropic flow model for annular orifices,

$$\dot{m} = \rho_{down} * V_{down} * A_{clearance} \tag{4.29}$$

$$V_{down} = \sqrt{2(h_{up} - h_{down})} \tag{4.30}$$

For a given inlet condition and constant entropy condition, every variable in these equations is a function of the downstream pressure only. To find where the mass flow rate reaches its maximum value, the derivative of $\dot{m}$ with respect to P_{down} (downstream pressure) can be set to zero.

$$\frac{d\dot{m}}{dP_{down}} = \sqrt{2(h_{up} - h_{down})}\frac{d\rho_{down}}{dP_{down}} - \frac{\rho_{down}}{\sqrt{2(h_{up}-h_{down})}}\frac{dh_{down}}{dP_{down}} = 0 \tag{4.31}$$

Rearranging the above equation one can obtain,

$$\frac{dh_{down}}{d\rho_{down}} = \frac{2(h_{up}-h_{down})}{\rho_{down}} \tag{4.32}$$

From equation (4.32) it can be seen that for a given inlet condition there is a corresponding outlet pressure that will satisfy this equation and that the mass flow rate is maximum. These equations are modeled in EES and the behavior of the isentropic model

is studied as inlet conditions are varied. All the inlet conditions are shown on a T-s diagram in figure 4.28. Three inlet entropies and four inlet pressures are tested.

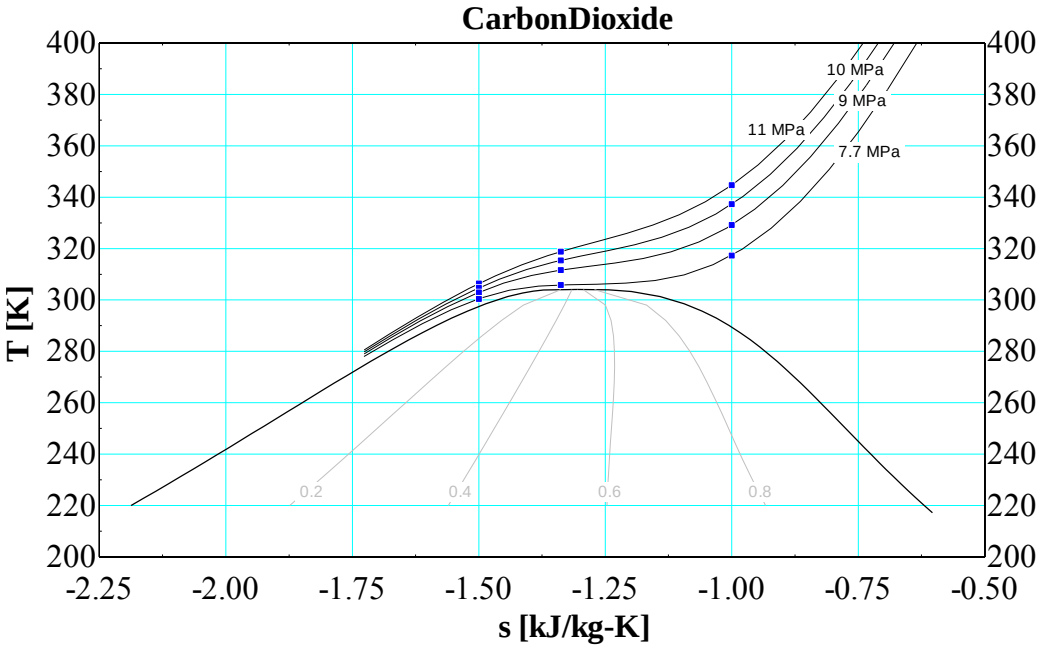

Figure 4.28: Inlet conditions used for testing 1-D isentropic model.

The results of the1-D isentropic flow model are presented in figures (4.29, 4.30 and 4.31). Some very important conclusions can be drawn from the behavior of the1-D isentropic model as inlet conditions are changed. Firstly, it can be seen that if geometry is fixed and the operating conditions are changed, the pressure at which the flow chokes changes as well as the leakage rate changes. For inlet entropy (S_{in}) = -1.0 KJ/Kg-K (right side of the two phase dome), the inlet pressures of 9 MPa and 10 MPa choke very close to the saturation pressure when the flow is expanded isentropically. Inlet pressure of 11 MPa choke before the flow enters two phase dome or chokes in superheated region for

this particular entropy, whereas inlet pressure of 7.7 MPa chokes late into the two phase dome.

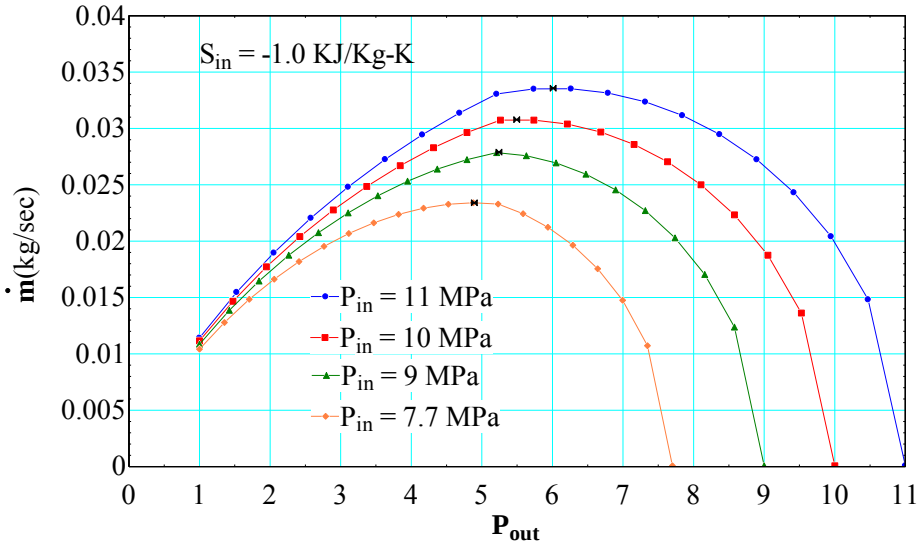

Figure 4.29: Isentropic flow behavior for Sin = -1.0 KJ/Kg-K.

For S_{in} = -1.338 KJ/Kg-K (very close to the critical point), inlet pressures of 11Mpa and 10Mpa choke at the critical point which is very close to the saturation pressure for this entropy whereas inlet pressures of 9Mpa and 7.7Mpa choke very late into the saturation dome.

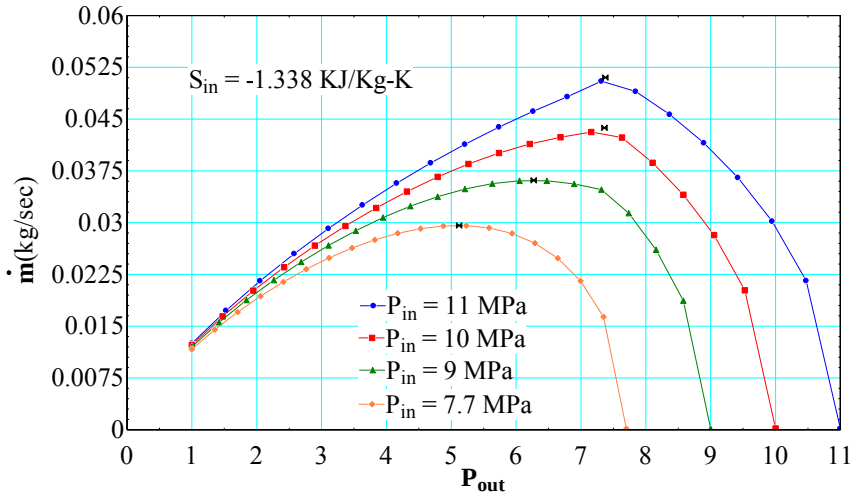

Figure 4.30: Isentropic flow behavior for Sin = -1.338 KJ/Kg-K.

For S_{in} = -1.5 KJ/Kg-K (left side of the two phase dome), the inlet pressures of 11MPa, 10MPa, and 9MPa choke right where the flow enters the saturation dome, whereas the inlet pressure of 7.7Mpa chokes late into the saturation dome.

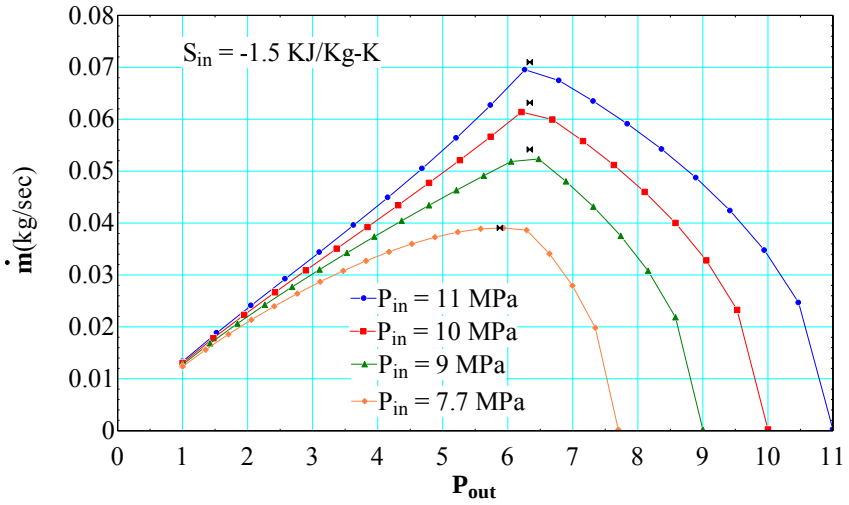

Figure 4.31: Isentropic flow behavior for S_{in} = -1.5 KJ/Kg-K.

Table 4.1 is generated to show the choking and saturation pressures for different inlet pressures and entropy conditions. From this analysis, we can ask ourselves a very valid question: "What is determining the choking point for each operating condition?" The isentropic flow theory explained in the next few pages of this thesis gives an idea about the choking behavior as operating conditions are varied.

Table 4.1 Choking and saturation pressures for various operating conditions

S_{in} [KJ/Kg-K]	P_{in}[MPa]	$P_{choking}$[MPa]	$P_{saturation}$[MPa]
-1.0	11	6.011	5.243
-1.0	10	5.494	5.243
-1.0	9	5.243	5.243
-1.0	7.7	4.892	5.243
-1.5	11	6.338	6.338
-1.5	10	6.338	6.338
-1.5	9	6.338	6.338
-1.5	7.7	5.887	6.338
-1.338	11	7.376	~ critical pressure
-1.338	10	7.362	~ critical pressure
-1.338	9	6.271	~ critical pressure
-1.338	7.7	5.121	~ critical pressure

From first law of Thermodynamics for a quasi-static process,

$$dh = \delta Q + v\, dP \tag{4.33}$$

According to Clausius equality, for a reversible process

$$\oint \frac{\delta Q}{T} = 0 \xrightarrow{yields} \delta Q = T\, ds \tag{4.34}$$

Hence,

$$dh = T\, ds + v\, dP \tag{4.35}$$

For an isentropic flow,$ds = 0$ implies

$$\rho\, dh = \ dP \tag{4.36}$$

Equation (4.36) can be applied to downstream condition as,

$$\rho_{down} \frac{dh_{down}}{d\rho_{down}} = \frac{dP_{down}}{d\rho_{down}} = c^2 \tag{4.37}$$

Equation (4.37) can be rearranged as,

$$\frac{dh_{down}}{d\rho_{down}} = \frac{2(h_{up} - h_{down})}{\rho_{down}} \tag{4.38}$$

$$\rho_{down} \frac{dh_{down}}{d\rho_{down}} = 2\left(h_{up} - h_{down}\right) = V_{down}^2 \tag{4.39}$$

From equations (4.37 and 4.39), the true definition of the choking point is

$$V_{down}^2 = c^2 \tag{4.40}$$

To answer the question raised earlier, downstream velocity (V_{down}) and local speed of sound (c) at the exit are plotted in figure 4.32 for a given inlet pressure and entropy as a function of outlet pressure. From equation (4.37) for a fixed inlet entropy the local speed of sound is only a function of the outlet pressure which is represented by the black curve in figure 4.32. It should be noted that there is a sudden drop in local speed of sound which occurs right when the fluid enters saturation dome, which is the

main criteria dictating the choking phenomenon. The homogeneous equilibrium model (HEM), as explained earlier, is assumed to calculate local speed of sound in the saturation dome. As inlet pressure increases, the downstream velocity increases for a given outlet pressure and as the outlet pressure is decreased, at a point velocity will be equal to the local speed of sound which is the choking point. The sudden change in the speed of sound occurs almost instantaneously at the saturation pressure for a given inlet entropy condition.

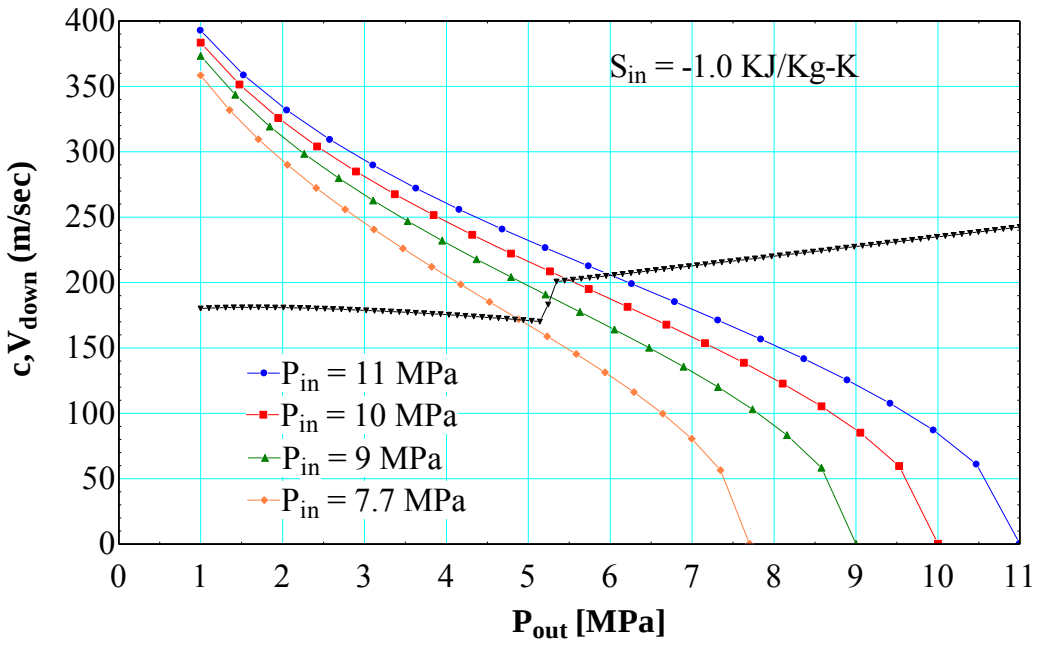

Figure 4.32: Downstream velocity and local sound speed of an annular orifice as a function of outlet pressure.

From a general observation of figure 4.33 it can be said that for a given inlet entropy condition, there exists a range of inlet pressures for which the downstream velocity intersect the sound speed curve very close to the saturation pressure. Following the above theory, inlet entropy is varied from $-0.75\frac{KJ}{Kg-K}$ to $-1.75\frac{KJ}{Kg-K}$ with an increment of $-0.05\frac{KJ}{Kg-K}$ and the upper and lower limit of inlet pressure for which the flow chokes at the saturation point is calculated for each S_{in}. The results of the above calculations are presented in figure 4.31 and the following conclusions are made:

a) If the inlet condition is bounded by the two curves, the flow chokes very close to the saturation point/ when flow enters the saturation dome.
b) If the inlet condition is above both the curves, the flow chokes before it enters the saturation dome.
c) If the inlet condition is below both the curves, the flow chokes late into the saturation dome.

The theory derived above is based on the isentropic flow assumption. So, the next question is: "Is this model valid for a real flow situation?"

To check the validity of this model simulations are performed for annular orifices holding the geometry constant and varying operating conditions as shown in (Table C.1 of Appendix C).

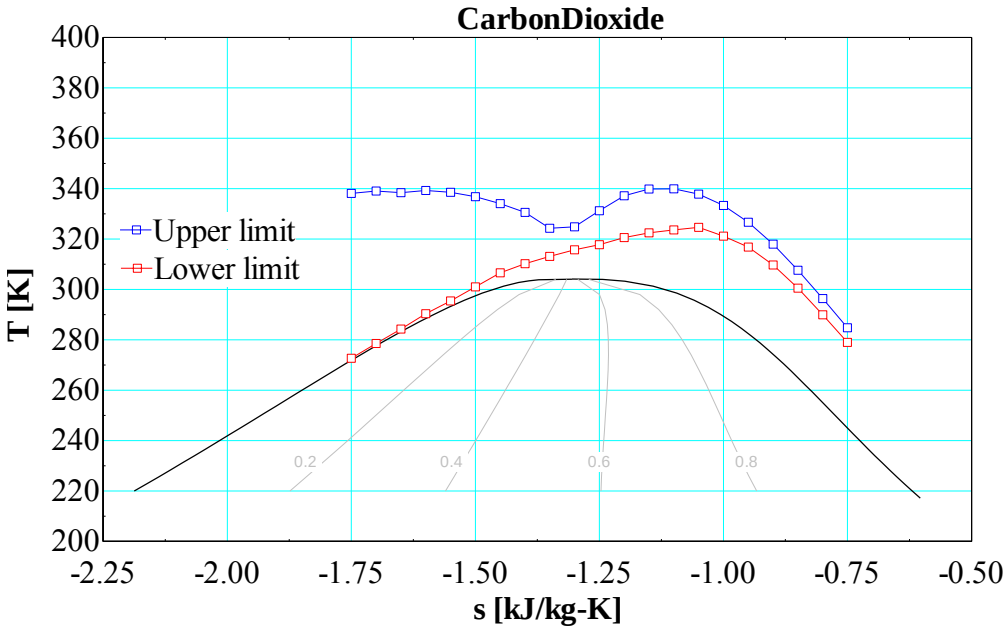

Figure 4.33: Choking theory for isentropic flow.

4.3.1 Results for annular orifice

The geometry of the annular orifice used for these simulations is the same as the geometry of case 2 in Appendix A. Simulations are performed for two different inlet densities (372 kg/m^3 and 498 kg/m^3) at an inlet pressure of 9 MPa (cases 4 and 5 of Table C.1 in Appendix C) and the leakage rate through the annular orifice for both these operating conditions are plotted in figures 4.34 and 4.35.

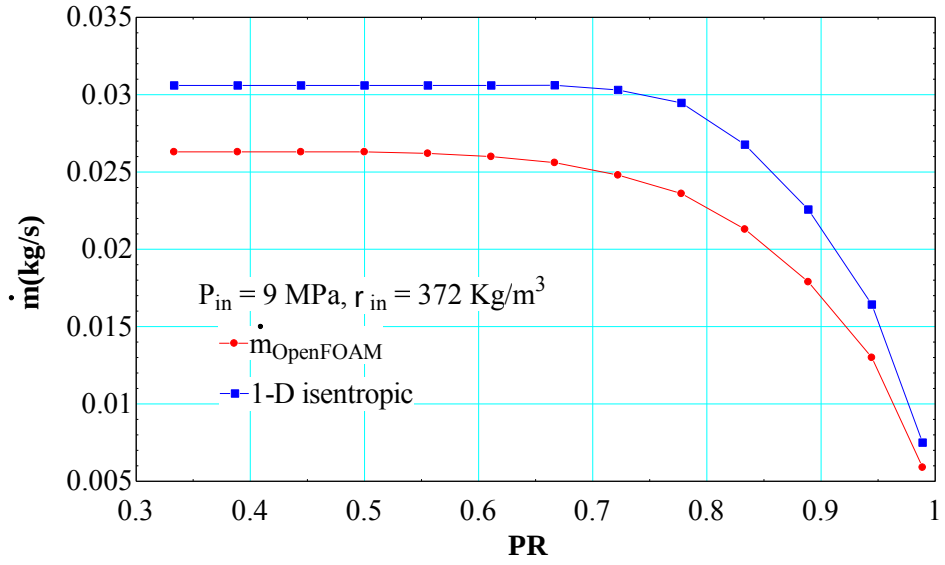

Figure 4.34: Leakage rate for inlet condition of 9 MPa and 372 Kg/m^3.

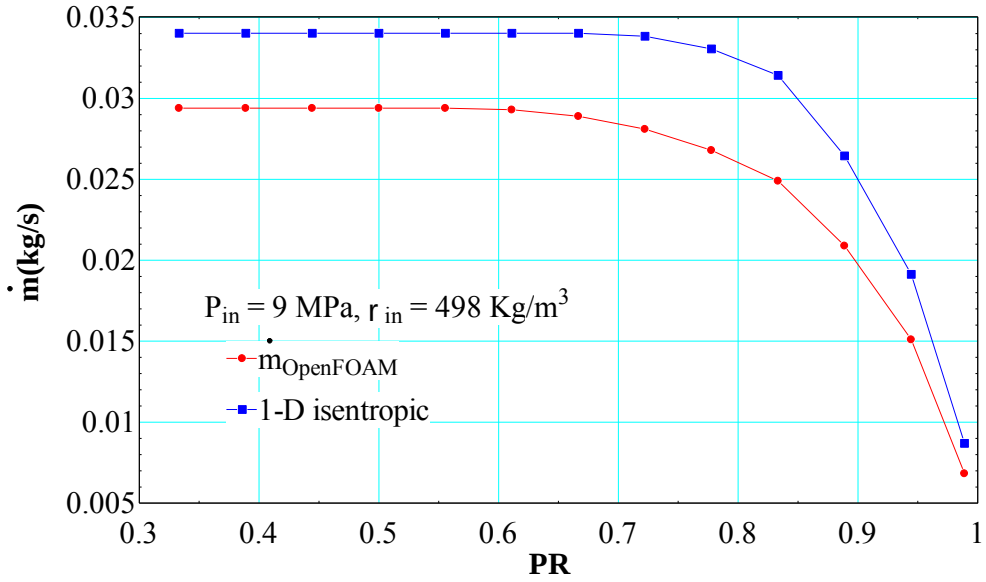

Figure 4.35: Leakage rate for inlet condition of 9 MPa and 498 Kg/m^3.

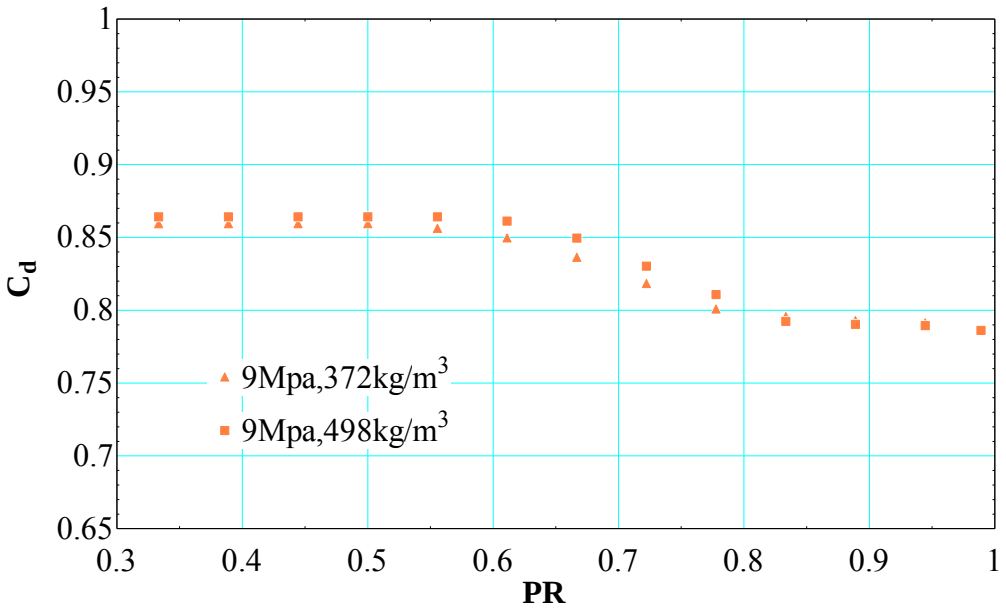

Figure 4.36: C_d for cases 4 and 5 in Table C.1 of Appendix C.

It can be noted that for a fixed inlet pressure as inlet density is increased the leakage rate increases which is what one would expect to see. However, it is interesting to note that the discharge coefficient for both these cases is nearly the same for all pressure ratios as can be seen from figure 4.36. The discharge coefficient stays constant at about 0.8 for higher pressure ratios before starting to increase.

Next, the inlet density is fixed as (372 kg/m^3 and 498 kg/m^3), the inlet pressure is increased to 10 MPa (case 3 in Table C.1 of Appendix C and case 2 in Appendix A) and the leakage rate through the annular orifice for both these operating conditions is plotted in figures (4.37 and 4.38). Again, the leakage rate is higher for higher density case and the discharge coefficient is the same for both these cases as shown in figure 4.39.

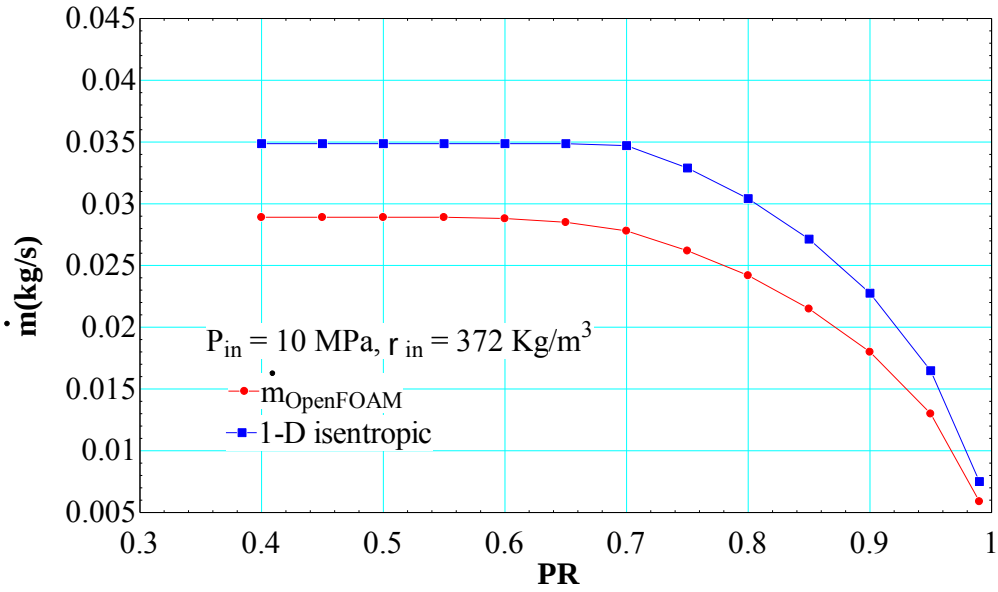

Figure 4.37: Leakage rate for inlet condition of 10 MPa and 372 Kg/m^3.

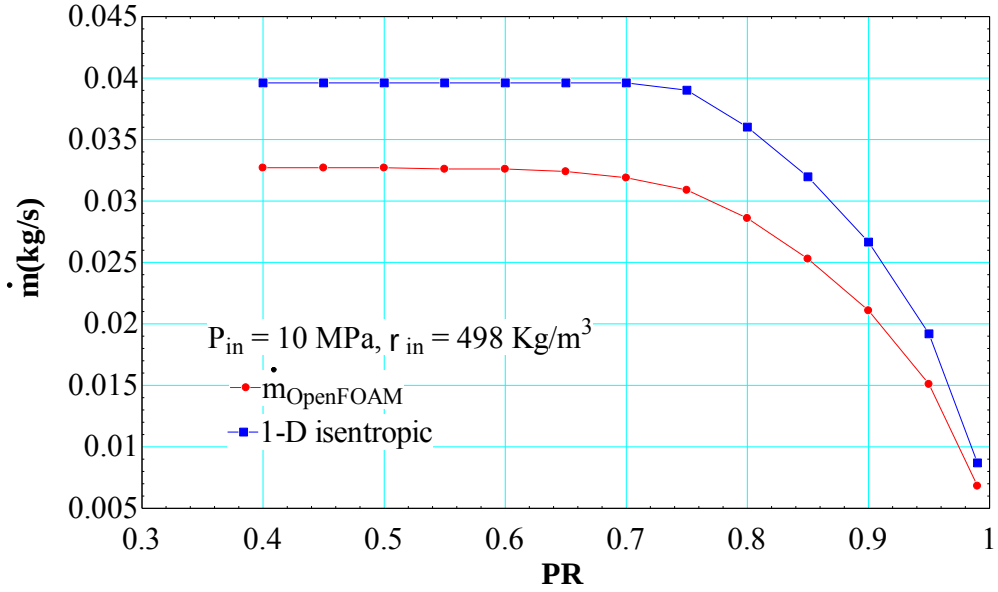

Figure 4.38: Leakage rate for inlet condition of 10 MPa and 498 Kg/m^3.

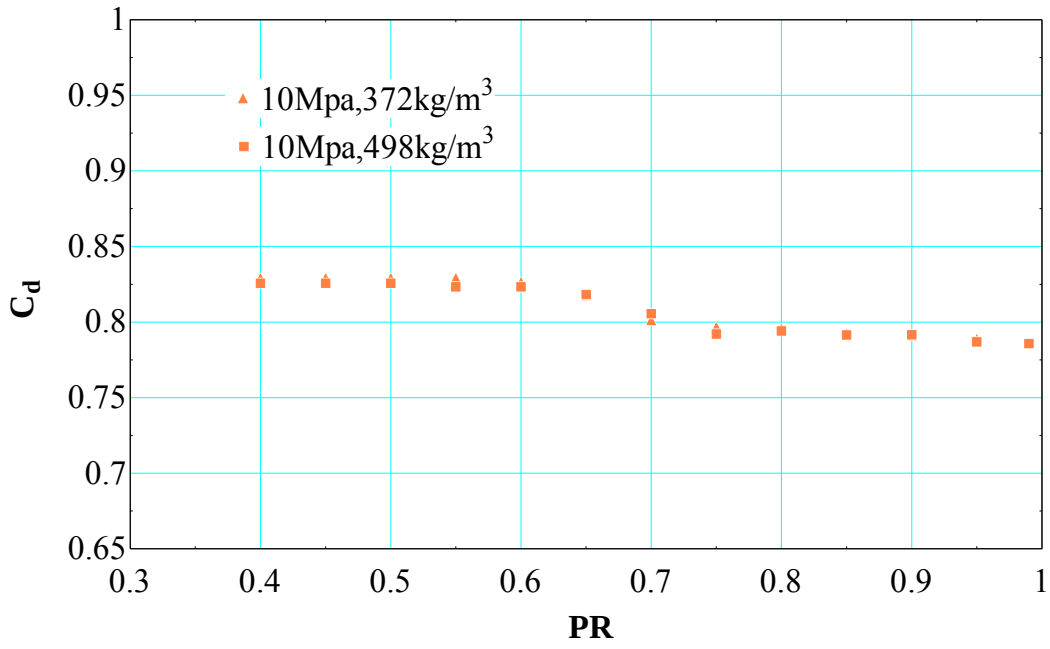

Figure 4.39: C_d for case 3 in Table C.1 and case 2 in Appendix A.

It can be noted from a comparison of the discharge coefficient plots (figures 4.36 and 4.39) that as pressure increases, the increase in C_d from higher PR to lower PR decreases. In other words, as the pressure increases, the discharge coefficient tends to stay constant over the whole range of PR. In order to see if this is really true, the inlet pressure was increased to 11 MPa and simulations (Cases 1 and 2 in Table C.1 of Appendix C) are performed for two inlet densities (372 kg/m^3 and 498 Kg/m^3) and the results for leakage rate are presented in figures (4.40 and 4.41). The discharge coefficient for these two cases is plotted in figure 4.42.

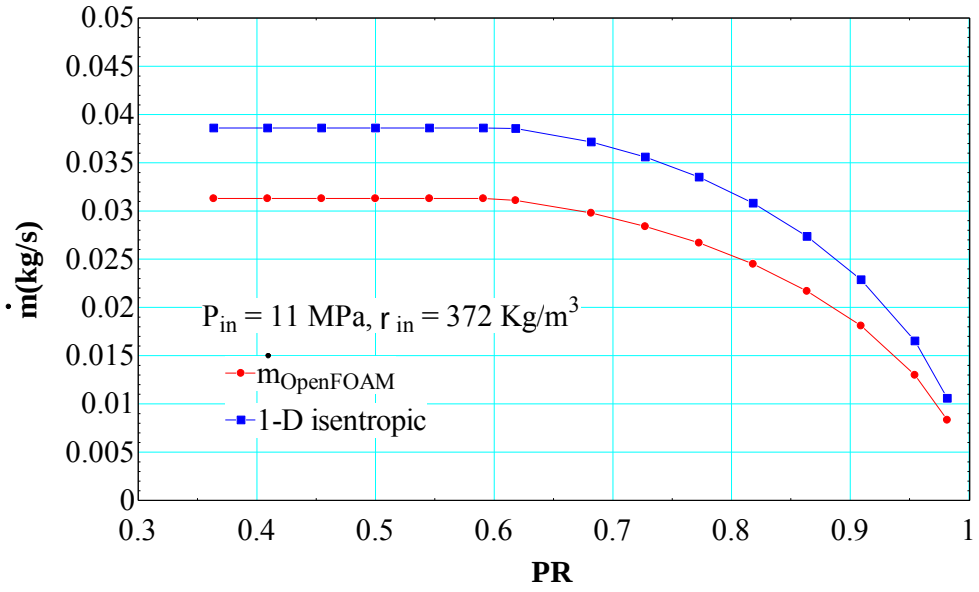

Figure 4.40: Leakage rate for inlet condition of 11 MPa and 372 Kg/m^3.

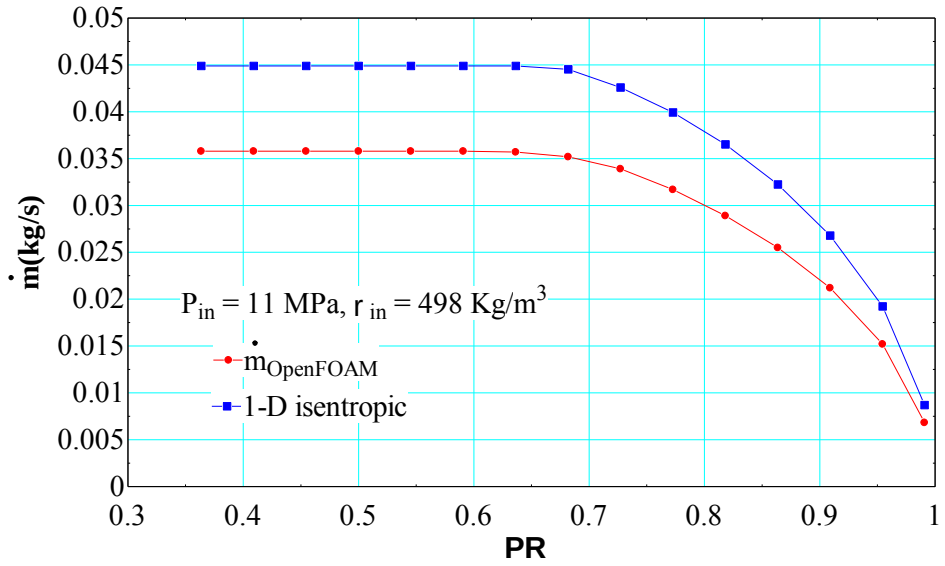

Figure 4.41: Leakage rate for inlet condition of 11 MPa and 498 Kg/m^3.

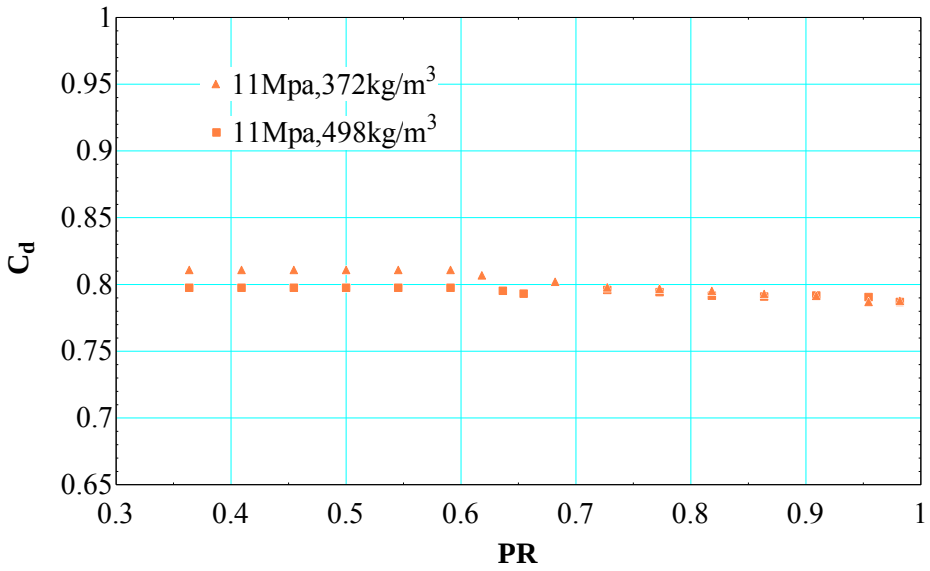

Figure 4.42: C_d for cases 1 and 2 in Table C.1 of Appendix C.

It is interesting to note that discharge coefficient stays nearly constant at 0.8 for both these cases which would mean that choking pressure ratio predicted by the simulations and isentropic model are nearly the same.

One case very close to the critical pressure is simulated (case 6 in Table C.1). It can be seen from the C_d plot, shown in figure 4.43, that spread in the C_d is much higher for this case compared to the high pressure cases (9, 10 or 11Mpa). Inlet conditions which are near the critical point are particularly hard to simulate because they are very close to the saturation dome and tend to deviate from the homogeneous equilibrium model as soon as they enter the saturation dome. As the discharge coefficient is only a function of the inlet pressure for inlet densities tested, it might be safely assumed that for a given inlet pressure, there exists a range of inlet densities for which discharge coefficient is only a function of inlet pressure.

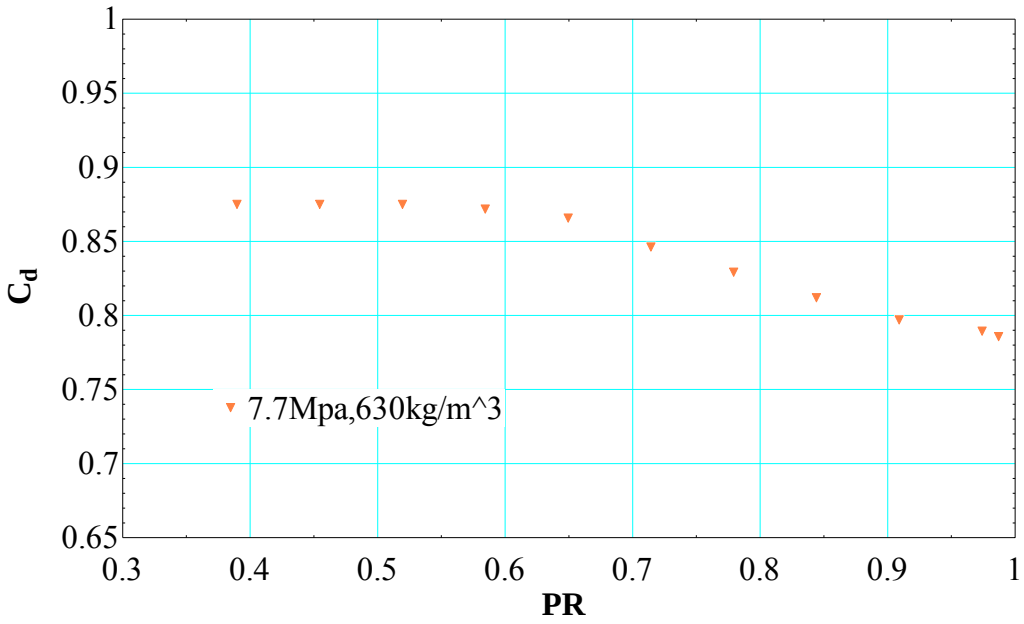

Figure 4.43: C_d for case 6 in Table C.1 of Appendix C.

Downstream conditions from all these simulations can be calculated based upon the following equations:

$$h_{up} = h(P_{up}, \rho_{up})$$

$$h_{down} = h(P_{down}, \rho_{down})$$

$$\dot{m}_{Openfoam} = \rho_{down} * A_{clearance} * V_{down}$$

$$h_{up} = h_{down} + \frac{V_{down}^2}{2}$$

$$S_{down} = S(P_{down}, \rho_{down})$$

$$T_{down} = T(P_{down}, \rho_{down})$$

These equations can be solved simultaneously in EES to calculate downstream temperature and entropy for each pressure ratio. These results are plotted in figure 4.44. For all these cases the choking point is calculated by fitting a sixth order polynomial to

the leakage rate data and taking a numerical derivative of the polynomial. The pressure ratio at which the numerical derivative is zero for the first time is taken as the choking PR.

$$\frac{d\dot{m}_{curvefit}}{dPR}|_{chokedflow} = 0 \tag{4.41}$$

The choking PR can alternatively be calculated by plotting V_{down}, and local speed of sound versus PR. The point where these two plots intersect is the choking PR according to our definition. Technically, choking occurs at the vena contracta, which is the point of minimum area for a fluid flow through an orifice. The Vena contracta might not necessarily occur at the exit of an orifice as a result of which the true fluid velocity at the vena contracta is unknown. Hence, care must be taken while applying this method to find the choking point.

From an observation of the flow curve it can be concluded that, for inlet conditions (11MPa, 372Kg/m^3) and (11MPa, 498Kg/m3), which are bounded by the two curves, choking occurs very close to the saturation point where flow enters the two phase region. As inlet condition drifts below the two curves (10MPa, 372Kg/m^3) and (10MPa, 498Kg/m^3) choking is slightly delayed going into the two phase region. Whereas for inlet conditions which are completely below the two curves (9MPa, 372Kg/m^3), (9MPa, 498Kg/m^3), and (7.7MPa, 630 Kg/m^3) choking occurs very late into two phase dome, which is in good agreement with the theory put forward earlier. It might be interesting to test some inlet conditions that are above both the curves but this is left to future work.

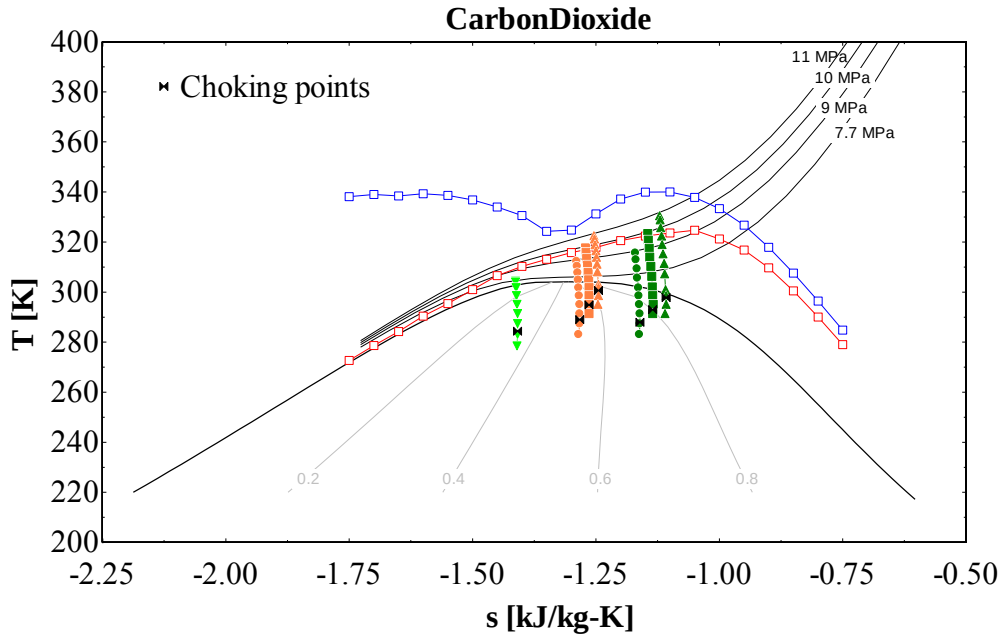

Figure 4.44: Choking point calculations for annular orifice (Flow curve).

One should expect that the presence of multiple teeth would cause a delay in choking as most of the times choking occurs at the exit of the last tooth where the pressure drop is maximum, as mentioned earlier. In that case we can ask ourselves a question: "Can the isentropic choking theory which worked well for annular orifices, be applied to labyrinth seals?" To answer this question the geometry is held constant, which is the same as case 2 in Appendix B, and the inlet operating conditions are varied. The inlet conditions simulated are the same as those used for annular orifices so that a direct comparison can be made (cases 1-6 in Table C.2 of Appendix C, case 2 in Appendix B).

4.3.2 Results for labyrinth seal

Three inlet densities (372, 498 and 630 Kg/m^3) are simulated for an inlet pressure of 9 MPa (cases 3-5 in Table C.2 of Appendix C) and leakage rate results for these three cases are presented in figures (4.45, 4.46 and 4.47).

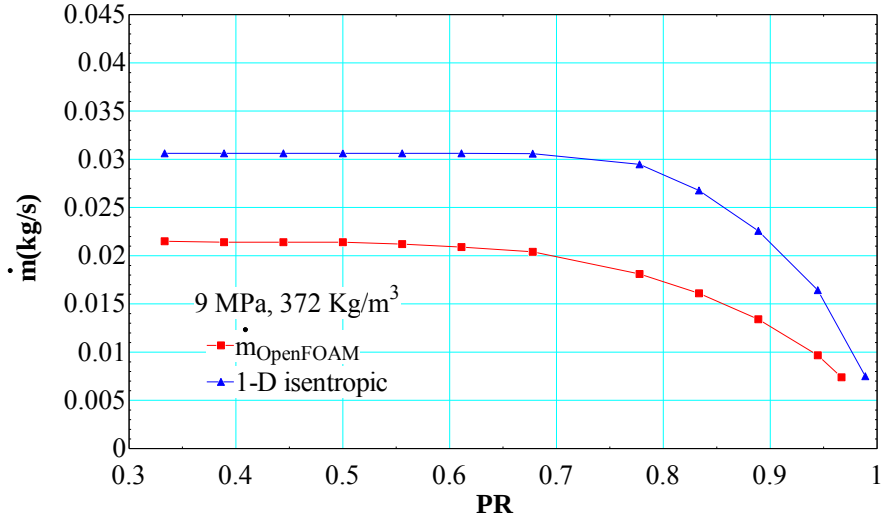

Figure 4.45: Leakage rate for inlet condition of 9 MPa and 372 Kg/m^3.

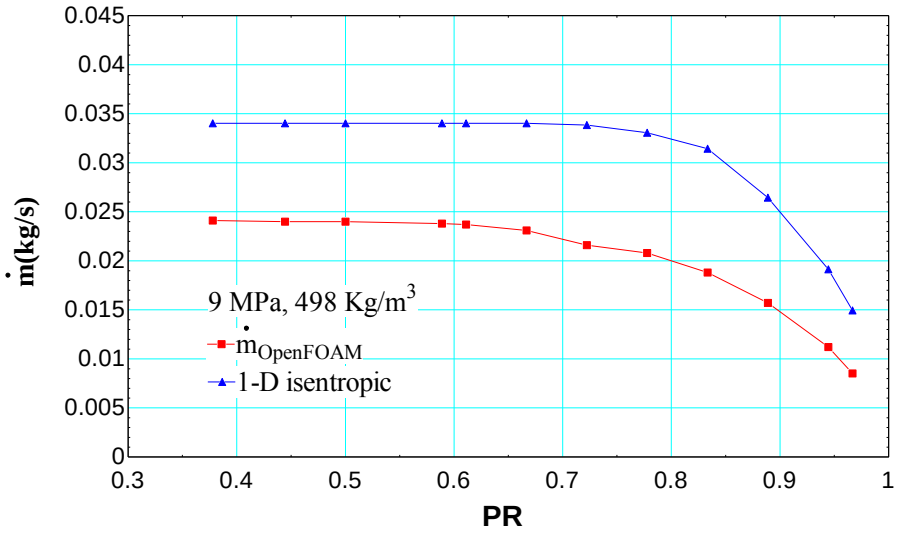

Figure 4.46: Leakage rate for inlet condition of 9 MPa and 498 Kg/m3.

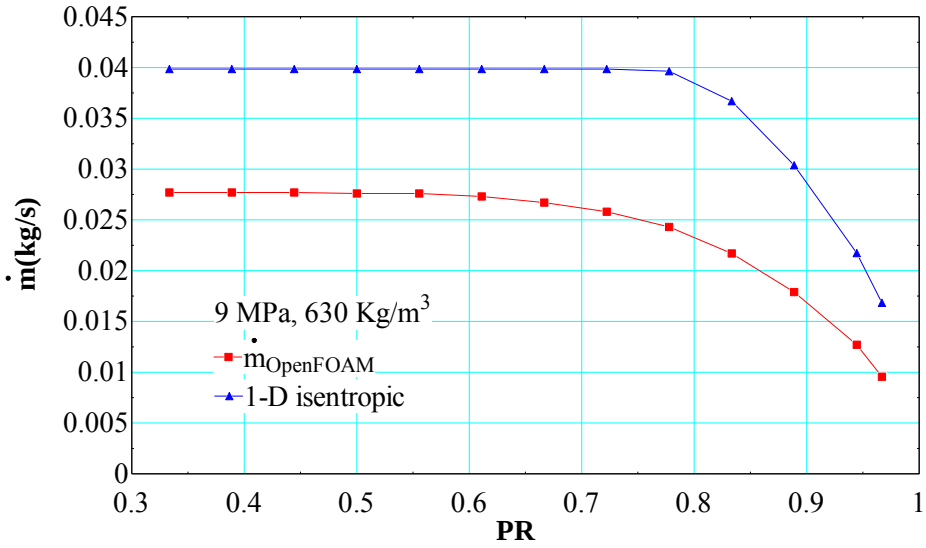

Figure 4.47: Leakage rate for inlet condition of 9 MPa and 630 Kg/m^3.

The conceptual $C_{d,}$ as defined earlier in equation (4.17) for all three cases is plotted in figure 4.48. It is interesting to note that the C_d for these inlet densities is nearly the same for all pressure ratios as observed in the case of annular orifices. However, the C_d which is 0.8 for higher PR's in the case of an annular orifice is now 0.6 for three teeth labyrinth seals indicating that the leakage rate has been reduced due to the presence of multiple constrictions.

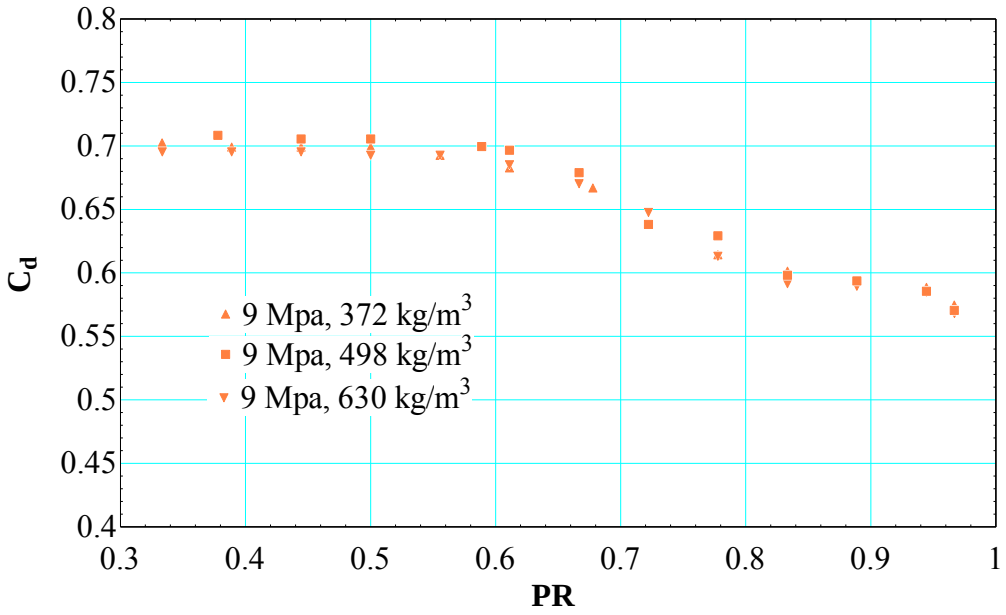

Figure 4.48: Conceptual C_d for an inlet pressure of 9 MPa (cases 3, 4 and 5 in Table C.1).

To see if this is true for other pressures as well, the pressure was increased to 10 MPa and two inlet densities (372 Kg/m^3 and 498 Kg/m^3) are simulated (case 2 in Table C.1 and case 2 in Appendix B). Results for the leakage rates are self-explanatory and are presented in figures 4.49 and 4.50. The conceptual C_d for both these cases, plotted in figure 4.51, collapse on to each other just like in the case of annular orifices reassuring our claim that, there exists a range of inlet densities for which C_d is only a function of inlet pressure.

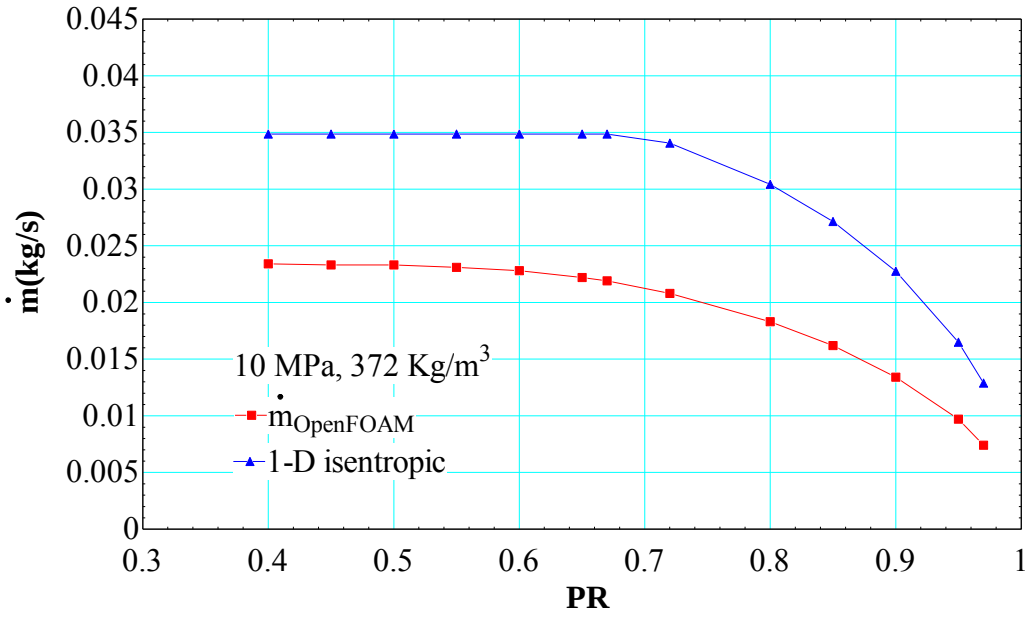

Figure 4.49: Leakage rate for inlet condition of 10 MPa and 372 Kg/m^3.

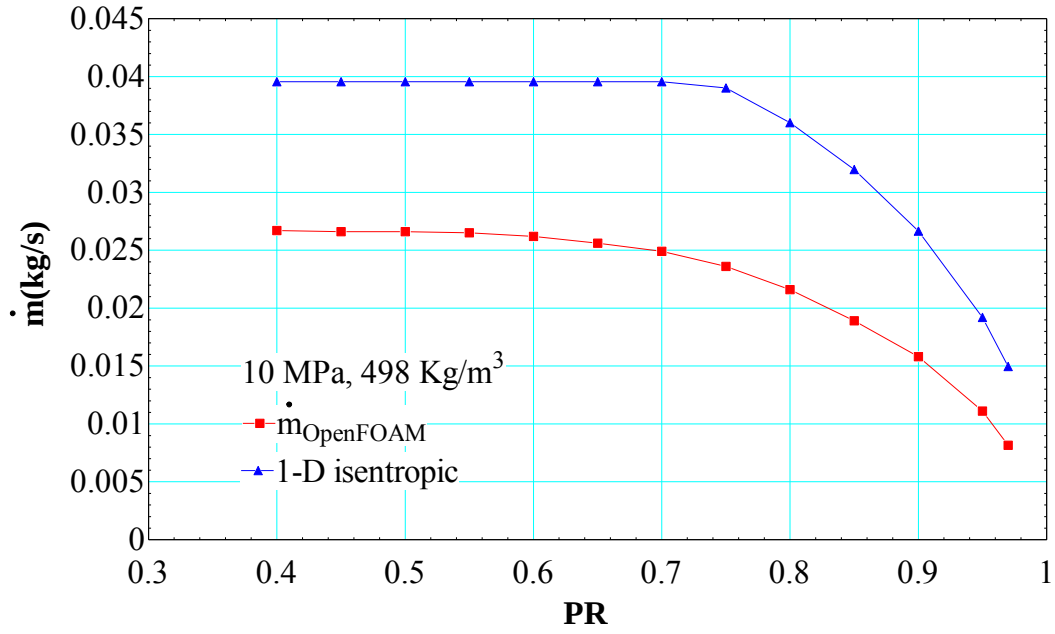

Figure 4.50: Leakage rate for inlet condition of 10 MPa and 498 Kg/m^3.

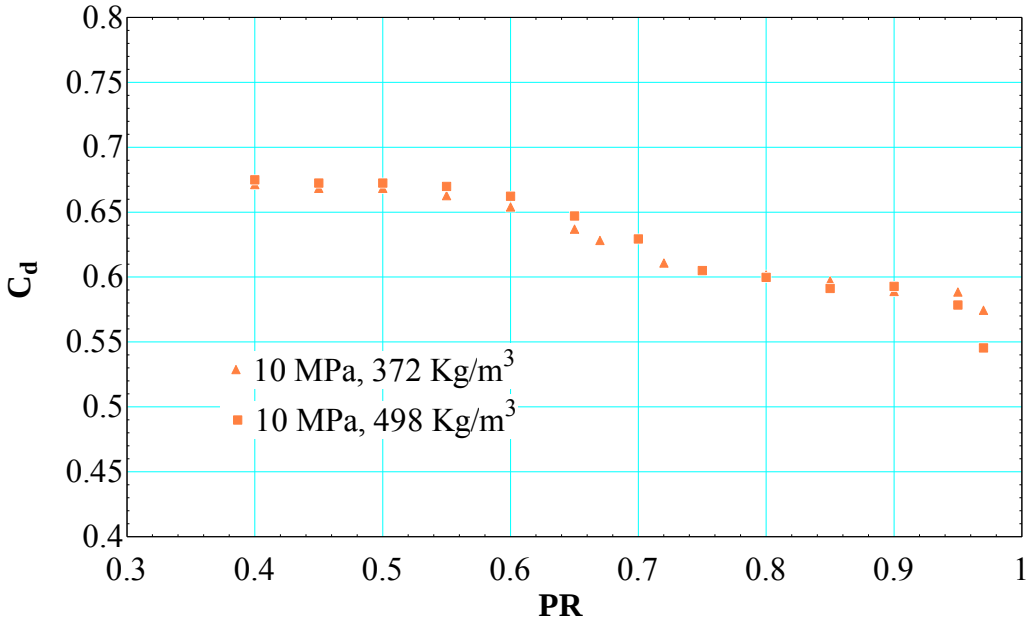

Figure 4.51: Conceptual C_d for an inlet pressure of 10 MPa.

One simulation was performed for an inlet pressure of 11MPa and density of 498 Kg/m^3 (case1 in Table C.1 of Appendix C) to check if C_d stays constant over the whole range of PR's like in the case of an annular orifice. The conceptual C_d for this case is presented in figure 4.52 and it can be seen that the C_d is not constant but is tending towards becoming constant. Further increase in pressure should result in a constant C_d over the whole range of PR.

The conceptual C_d for 7.7 MPa, 630 Kg/m^3 (case 6 in Table C.2 of Appendix A) presents some unusual behavior as shown in figure 4.53. The reason why the C_d starts increasing instead of staying constant at higher PR's is unknown at this point and requires more detailed study. As for now it can be safely assumed that the unusual trend

is caused due to the presence of multiple constrictions as this behavior is not observed in the case of an annular orifice for the same operating condition (Figure 4.43).

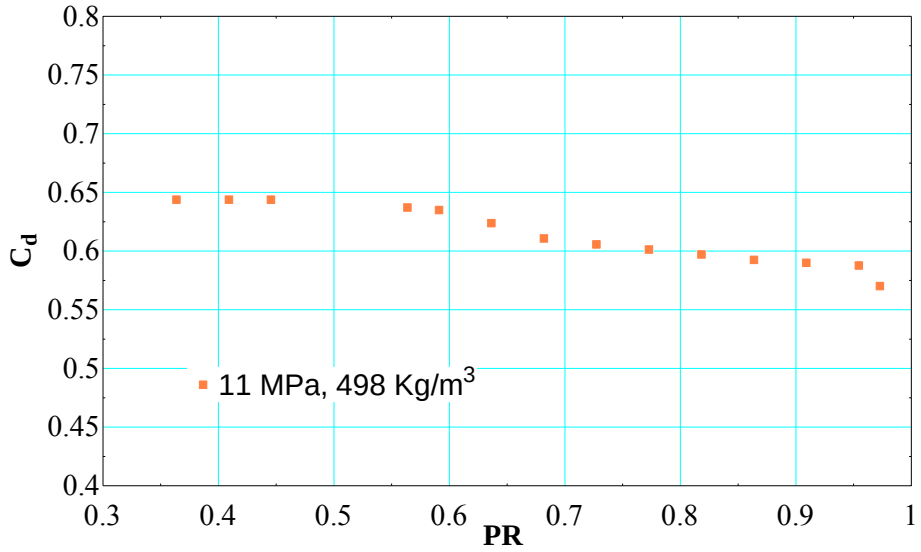

Figure 4.52: Conceptual C_d for an inlet pressure of 11 MPa.

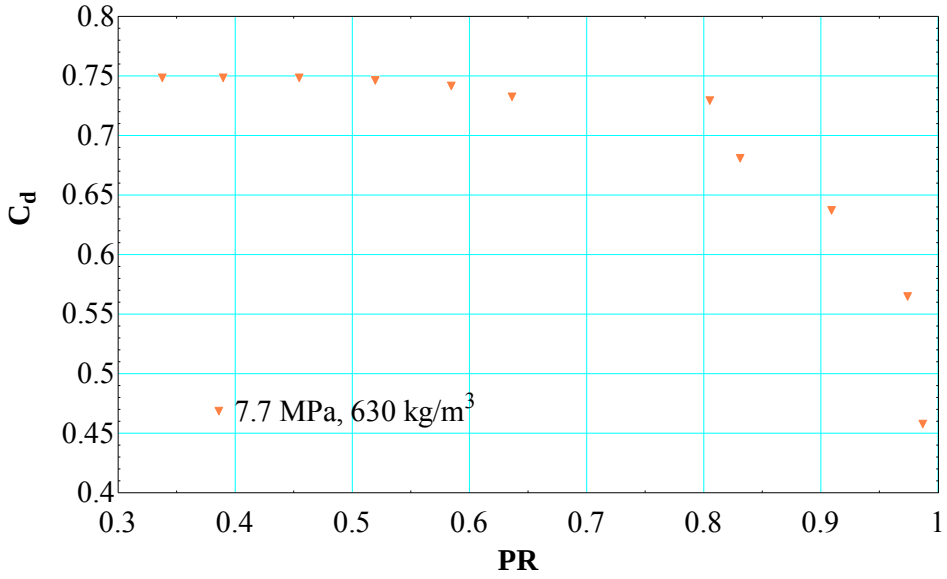

Figure 4.53: Conceptual C_d for an inlet pressure of 7.7 MPa.

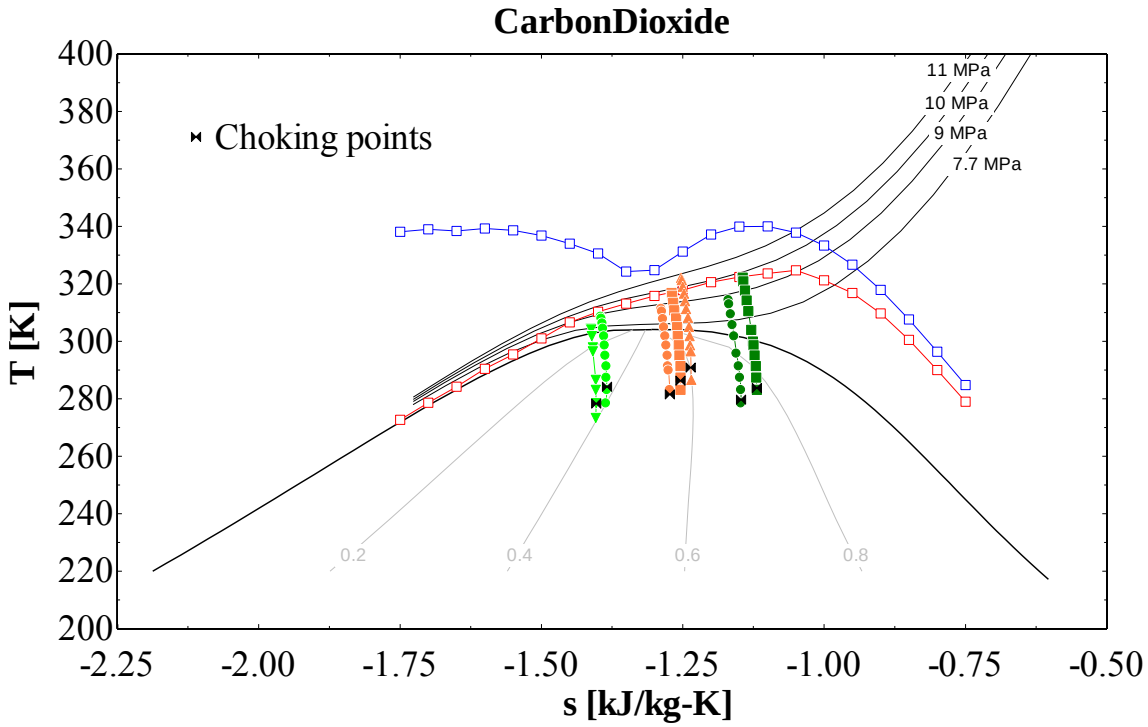

Figure 4.54: Choking point calculations for labyrinth seal (Flow curve).

From figures (4.54 and 4.44), it can be observed that for a similar set of operating conditions choking in the case of labyrinth seals is significantly delayed compared to annular orifices. Even for an operating condition of 11Mpa, 498Kg/m^3 which is bounded by the two curves, the flow chokes late into the two phase dome suggesting that 1-D isentropic choking theory derived for annular and plain orifices cannot be extended to labyrinth seals. So, "Is there a 1-D isentropic model which can predict choking behavior of labyrinth seals?"

Let us revisit the 1-D isentropic model presented for labyrinth seals. From the 1-D isentropic model the local speed of sound at the exit of a labyrinth seal is defined as,

$$\rho_{down}\frac{dh_{down}}{d\rho_{down}} = \frac{dP_{down}}{d\rho_{down}} = c^2 \qquad (4.42)$$

From equation (4.42), it can be said that for a given inlet entropy condition and downstream pressure the local speed of sound at the exit is independent of upstream conditions and the geometry of the labyrinth seal. Therefore, under similar conditions the speed of sound is the same for annular orifices as well as labyrinth seals. However, the downstream velocity of the fluid will depend on the geometry and is different for annular orifices and labyrinth seals. Figure 4.32 presented the calculations for local speed of sound and downstream velocity as a function of upstream and downstream pressures for an annular orifice (S_{in} = -1.0 KJ/Kg-K). In the case of a labyrinth seal, equations (4.19 – 4.28) are used to the calculate downstream velocity and the results are presented in figure 4.55 for S_{in} = -1.0 KJ/Kg-K.

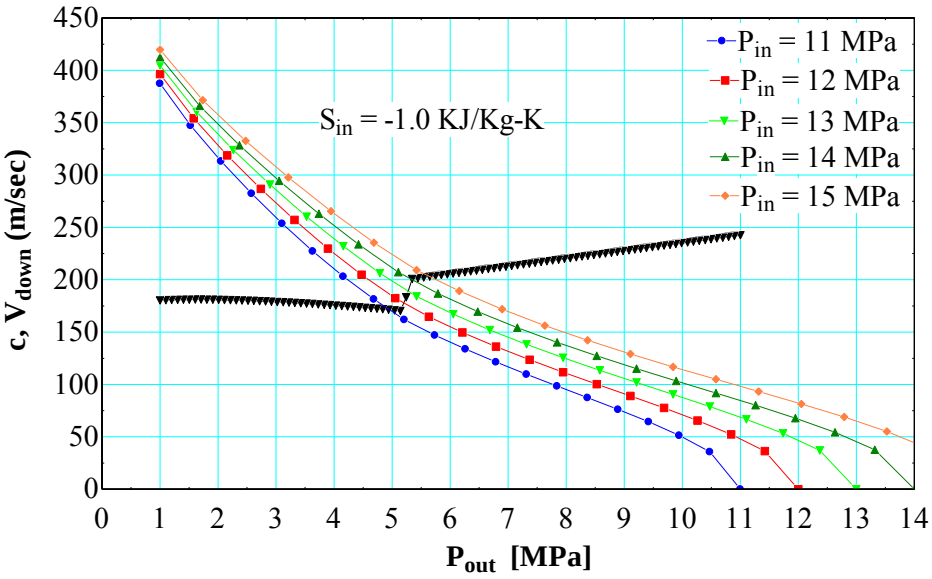

Figure 4.55: Downstream velocity of labyrinth seal and local sound speed as a function of outlet pressure.

Figures 4.55 and 4.32 indicate that for an inlet pressure of 11MPa, the 1-D isentropic model for labyrinth seals chokes in the saturation dome and the 1-D isentropic model for an annular orifice chokes above the saturation dome. Therefore, the curves developed using 1-D isentropic choking model for annular orifices cannot be extended to labyrinth seals. However, from a general observation of figure 4.55 it can be said that there exists a range of inlet pressures for which the downstream velocity curve intersects the sound speed curve very close to the saturation pressure. Following this theory, the inlet entropy can be varied and the upper and lower limit of the inlet pressure for which the flow chokes at saturation point can be calculated for each inlet entropy. This would result in two different sets of curves but the conclusions made for annular orifices are still valid in the case of labyrinth seals.

CHAPTER V

VALIDATION OF COMPUTATIONAL DATA

Some experimental data obtained from the University of Wisconsin, Madison will be used in this section to show the capabilities of model developed in OpenFOAM. It should be noted that the author did not perform any experiments for this thesis. The experimental data available is that of a plain orifice having an inner diameter of 1.006 mm and a length of 5 mm resulting in $L/D \sim 5$. The radius of curvature of the inlet edge has been carefully measured at UW, Madison and it has been reported that the edge can be considered as a sharp edge. Hence, a sharp edge has been used for these computational studies. However, it is very important to measure the radius of curvature accurately as it has a significant effect on the leakage rate as shown later in this section. Simulations are performed for this particular orifice for different operating conditions (Table C.3) and leakage rate results are presented in figures 5.1 through 5.5.

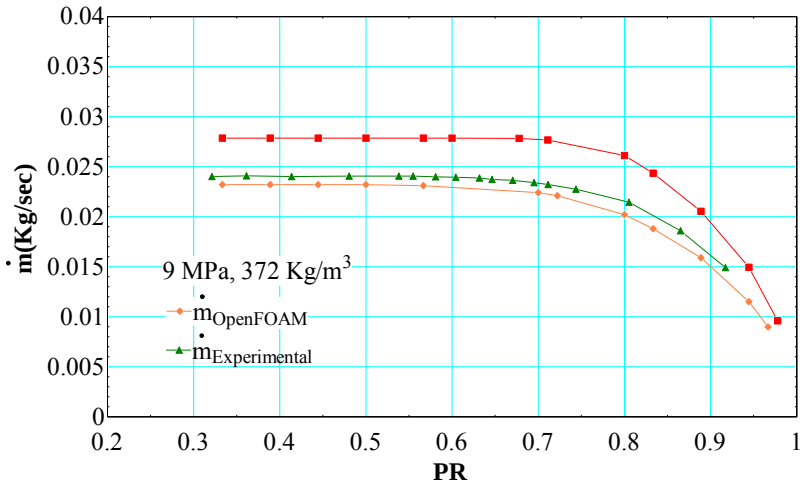

Figure 5.1: Leakage rate for inlet condition of 9 MPa, 372 Kg/m^3 (case 1 in Table C.3).

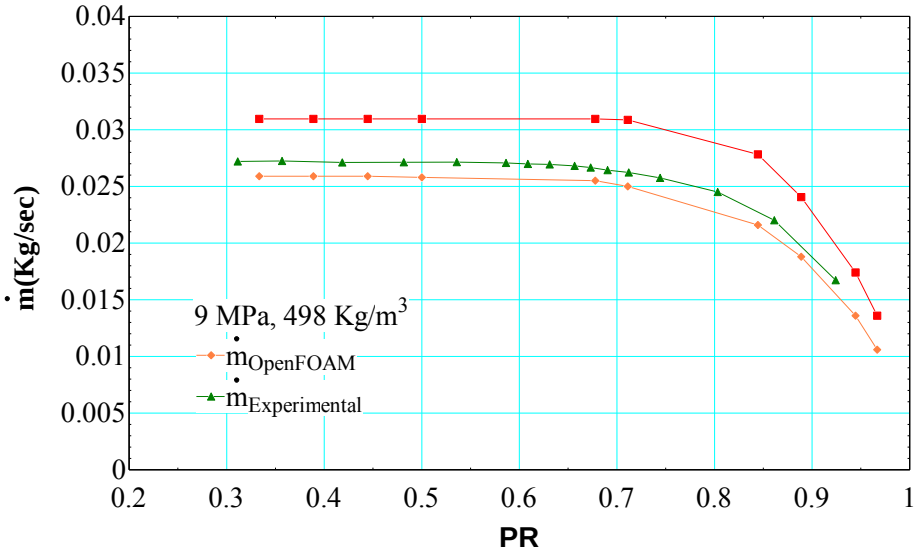

Figure 5.2: Leakage rate for inlet condition of 9 MPa, 498 Kg/m^3 (case 2 in Table C.3).

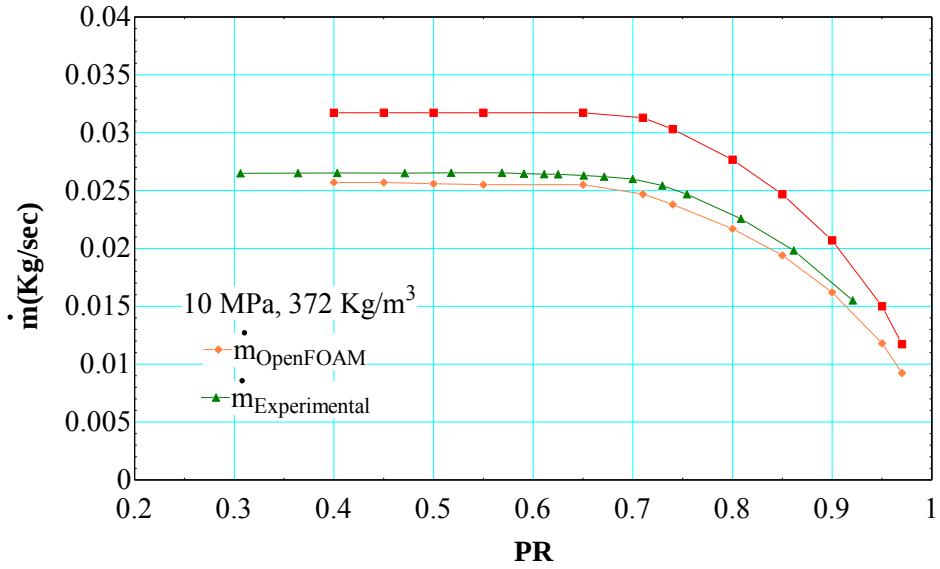

Figure 5.3: Leakage rate for inlet condition of 10 MPa, 372 Kg/m^3 (case 3 in Table C.3).

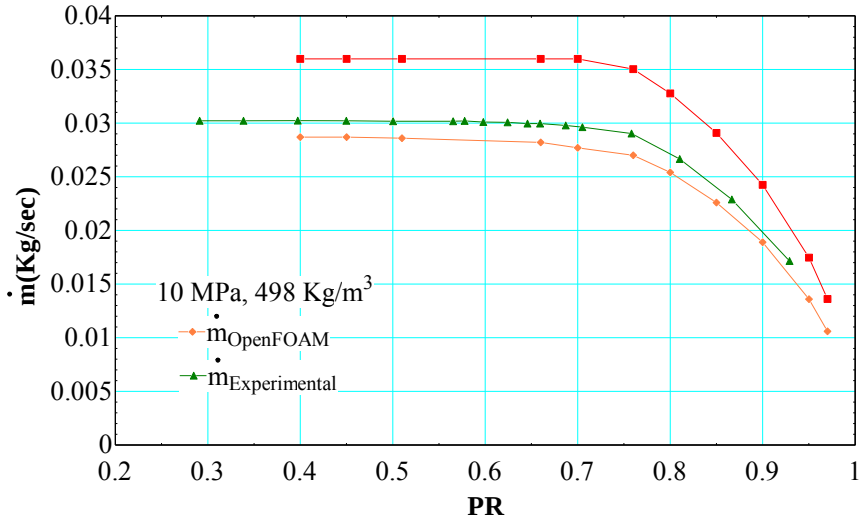

Figure 5.4: Leakage rate for inlet condition of 10 MPa, 498 Kg/m^3 (case 4 in Table C.3).

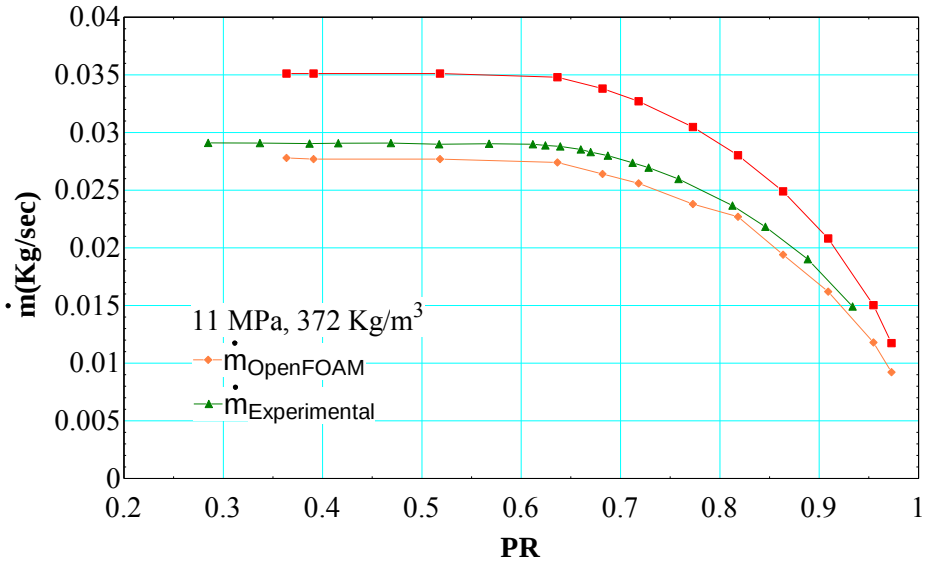

Figure 5.5: Leakage rate for inlet condition of 11 MPa, 372 Kg/m^3 (case 5 in Table C.3).

It can be qualitatively concluded from these figures that OpenFOAM, is in general, capable of predicting the experimental data for all operating conditions. For each operating condition, the PR's at which experimental data is available doesn't match with that of computational data and hence, in order to facilitate a comparison, a 6th order polynomial curve is fit to the experimental data and the leakage is calculated for the needed PR's. An error analysis is performed to compare the numerical simulation data with that of the experimental data and the results are plotted in figure 5.6 for all operating conditions. It can be concluded from the error analysis that the majority of the simulation data for higher PR and low leakage rate are within +/- 10 % of experimental values and for low PR and high leakage rate all data points are within +/- 10 % of experimental values with majority of the data close to a 5 % error. This slight error could be due to the fact that there are adverse property changes as S-CO_2 flows through an

orifice and a refined mesh based on gradients in properties is needed to capture the flow field more accurately. Implementing an adaptive mesh refinement algorithm in OpenFOAM to refine the mesh automatically based on gradients in properties will minimize the error further and is to future work.

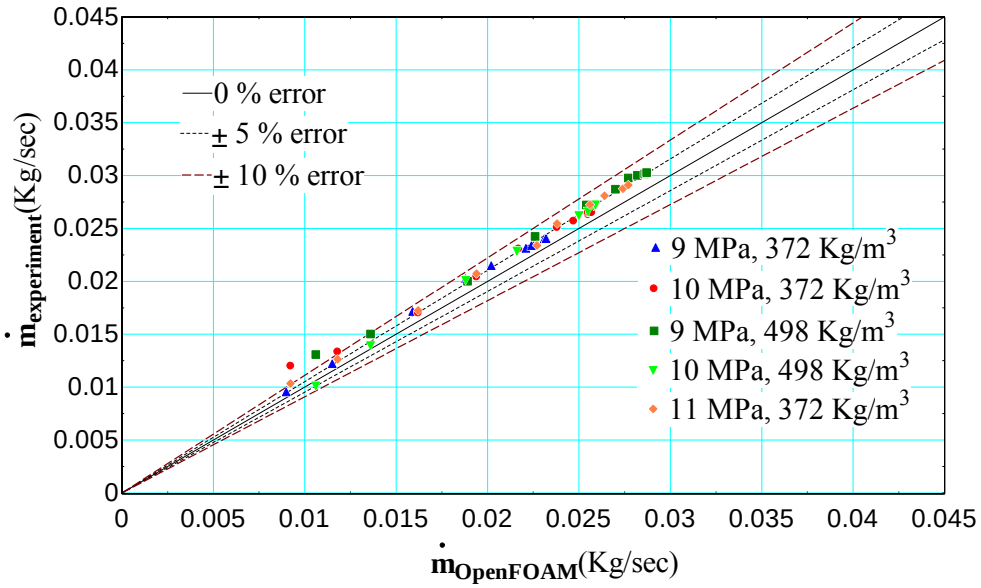

Figure 5.6: Error analysis for Plain orifice data.

5.1 Effect of radius of curvature

Due to flow separation at the inlet of an orifice, the area at vena contracta might change as the radius of curvature is changed. Hence, it is important to measure the radius of curvature of the inlet edge as it has a significant effect on the leakage rate as shown in figure 5.7. The presence of a chamfered edge with a chamfer radius as small as 0.005 mm causes the leakage rate to increase by about 5 %. In the future, if numerical data is being compared to the experimental data care has to be taken to measure the radius of

curvature accurately and use it for simulations otherwise the error between simulations and experiments can be expected to be as high as 5-10 %.

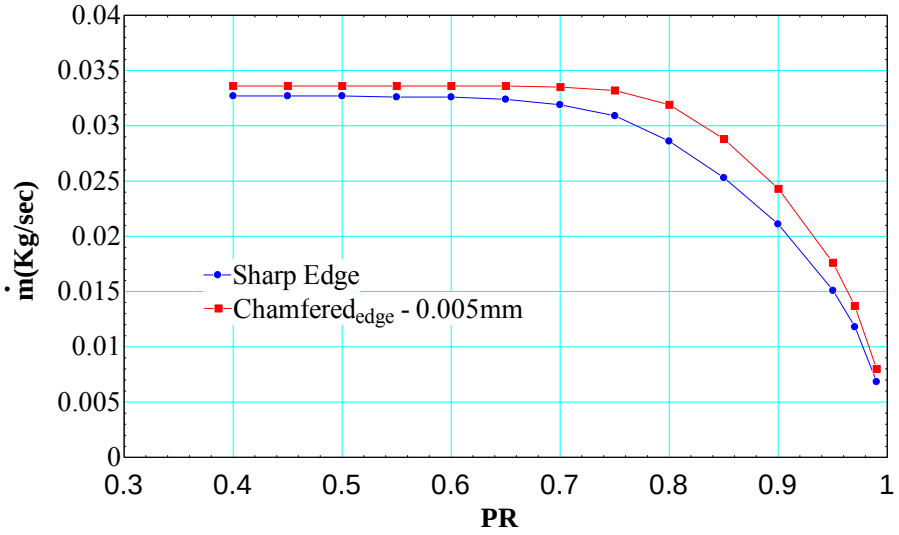

Figure 5.7: Effect of radius of curvature on leakage rate.

CHAPTER VI

CONCLUSIONS AND FUTURE WORK

This thesis was based on computational studies performed to understand the qualitative behavior of S-CO_2 flow through labyrinth seals. An Open source CFD software Open FOAM was used to perform a series of simulations for S-CO_2 flow through annular orifices, labyrinth seals and some plain orifices. To accurately model the properties of S-CO_2, a FIT (Fluid Property Interpolation Tables) algorithm was implemented in OpenFOAM which is based on biquintic spline interpolation resulting in an error of about ~ 0.01 %. To solve the Navier-Stokes equations in the saturation dome, Homogeneous equilibrium model (HEM) is assumed to be valid. All simulations performed are tabulated in Appendix A, B and C. This parametric study was divided into two parts:

The first part explained about the effect of geometrical parameters on leakage rate through seals while holding operating condition constant. (Appendix A and B) Conclusions that can be drawn from study of geometrical parameters are as follows:

1) W_{tooth}/c (Tooth width to clearance ratio) is the only major geometrical parameter influencing discharge coefficient of an annular orifice.
2) There exists a certain range of W_{tooth}/c for which C_d is independent of W_{tooth}/c.
3) Except for very low h/s (tooth height to pitch ratio) tooth depth has no significant effect on C_d.

4) The carryover coefficient, γ as defined by Hodkinson is independent of pressure ratio and stays constant for a fixed geometry of a seal.
5) The major geometrical parameters influencing γ is *c/s* (clearance to pitch ratio) and to some extent W_{cavity}/c (Cavity width to clearance ratio).
6) Based on the results from numerical simulations a model for γ has been developed. This model is developed for constant tooth width and needs modification in the future to include effect of tooth width.

$$\gamma = 0.91559 + \left[0.395745 + 0.113839\left(\frac{W_{cavity}}{c}\right)\right]\left(\frac{c}{s}\right)$$

7) Shaft rotation has no effect on C_d of an annular orifice at lower PR's but has a significant effect for a smaller pressure drop and needs further validation to develop a model for the same.
8) Shaft rotation has no influence on the carryover coefficient.
9) To predict leakage through a labyrinth seal, each constriction can be treated individually and leakage rate equation for each constriction can be written as,

$$\dot{m} = C_d|_{ntooth}\gamma\dot{m}_{isentropic}$$

Where the C_d of the first tooth is same as that of an annular orifice and C_d for the following tooth depends on the C_d of previous tooth and γ of the cavity. For first constriction γ is equal to 1.

10) A simple 1-D isentropic model for labyrinth seals assuming C_d and γ equal to 1, works reasonably well in predicting leakage through multiple constrictions.

The second part explained about the effect of operating conditions on the leakage rate and choking through a seal while holding the geometry constant.

Conclusions that can be drawn from study of operating conditions are as follows:

1) Changing the inlet operating condition changes leakage through seals significantly depending on inlet density and pressure.
2) A 1-D isentropic choking theory has been put forward which predicts that there exist a range of inlet pressures for which the flow chokes at the saturation point for a given inlet entropy condition. Based on this theory, two curves are presented for an annular orifice. These two curves control choking based on inlet operating condition as follows:
    a. If the inlet condition is bounded by the two curves, the flow chokes very close to the saturation point when the flow enters the saturation dome.
    b. If the inlet condition is below both the curves, flow chokes late into the saturation dome.
    c. If the inlet condition is above both the curves, the flow chokes before it enters the two phase dome.
3) The 1-D isentropic choking theory developed is applied to simulations performed on annular orifices for a range of operating conditions (Table C.1) and it has been observed that the theory works reasonably well for all the cases.
4) From simulations performed on annular orifices and labyrinth seals (Table C.1 and C.2) it has been shown that, for a given inlet pressure there exist a range of

inlet densities for which the discharge coefficient is independent of density and is only a function of inlet pressure.

5) At high enough inlet pressures where properties are not sensitive to temperature changes, S-CO_2 behaves more like an incompressible fluid and the discharge coefficient stays constant over the whole range of PR's. This inlet pressure increases as the number of constriction in a labyrinth seal increases.
6) It has been concluded that the 1-D isentropic choking model is in general valid for any labyrinth seal geometry but the upper and lower pressure limit curves depend on the number of constrictions present in the labyrinth seal. As number of constrictions increases these two curves move farther away from the critical point.

Finally, some experimental results for circular orifice (L/D ~ 5) obtained from the University of Wisconsin, Madison were used to show the capabilities of the FIT model implemented in OpenFOAM and the validity of the homogeneous equilibrium model. Simulations to match these experiments were performed and are shown in Table C.3. A comparison of numerical results with that of experimental results indicated that OpenFOAM is capable of predicting experimental data within 10 % error with majority of data close to 5 % error. This concludes that the HEM is good in predicting CO_2 flow behavior in two phase dome. Error can be minimized by implementing an adaptive mesh refinement algorithm in OpenFOAM to refine the mesh based on the gradients in properties or flow variables.

Recently, an experimental supercritical CO_2 seal testing loop has been completed in construction to measure the flow rate of carbon dioxide driven by large pressure drops through shaft seal geometries. Figure 5.1 shows the schematic of seal test loop facility and details of the components of seal test loop are provided in Appendix D.

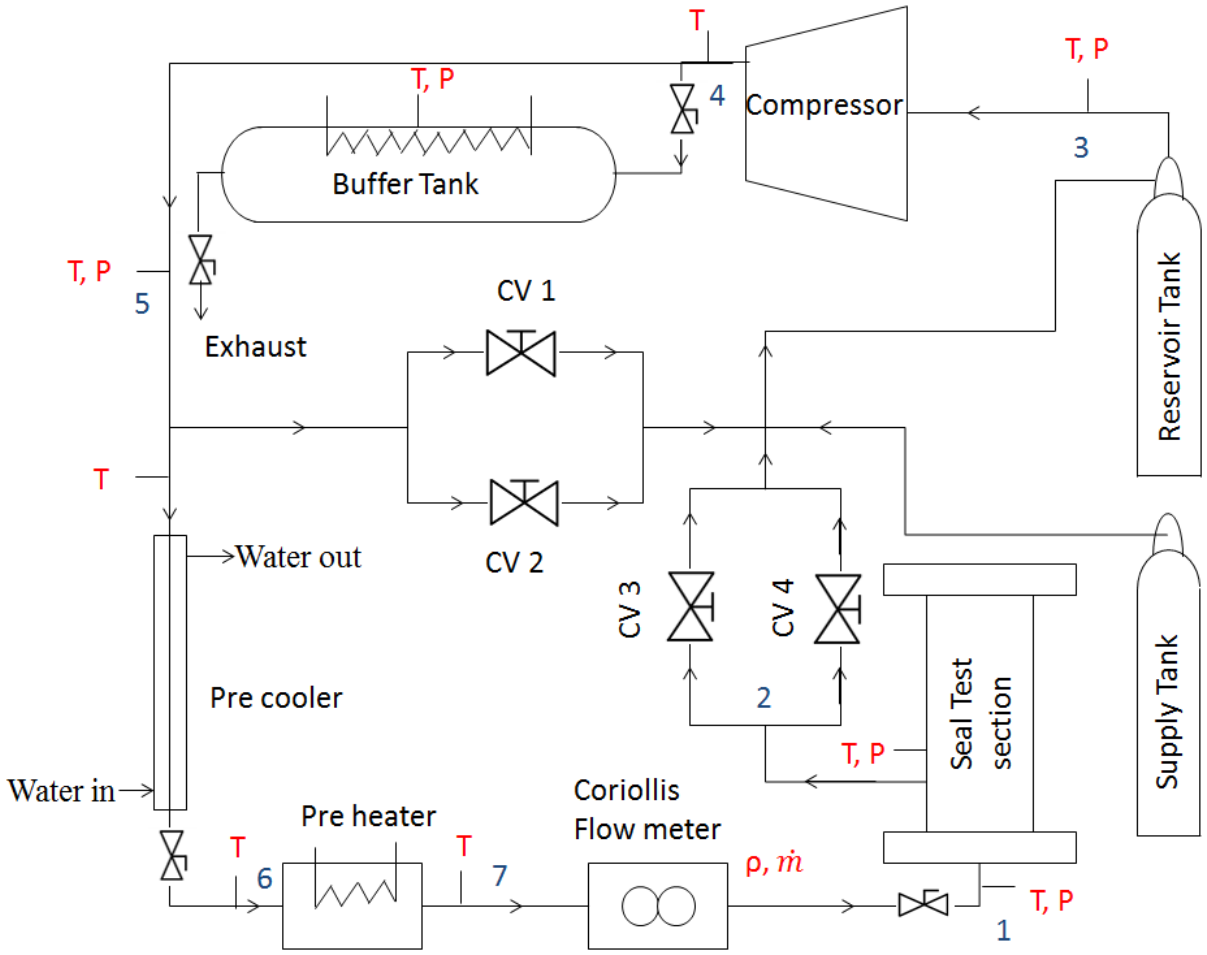

Figure 6.1: Schematic of S-CO_2 seal testing facility.

REFERENCES

[1] USDoE, 2002. *"A Technology Roadmap of Generation IV Nuclear Energy Systems",* Issy-les-Moulineaux, France: In Proceedings of Nuclear Energy Research Advisory Committee and the Generation IV International Forum.

[2] Dostal, V., Hejzlar, P. & Driscoll, M., 2006. "The Supercritical Carbon Dioxide Power Cycle:Comparison to Other Advanced Power Cycles". *Nuclear Technology,* Volume 154(3), pp. 283-301.

[3] Dostal, V., 2004. " A Supercritical Carbon Dioxide Cycle for Next Generation Nuclear Reactors". PhD thesis, Nuclear Engineering Department, Massachusetts Institute of Technology, Cambridge, MA, USA.

[4] Klein, S. & Nellis, G., 2011. *Thermodynamics.* New York, NY, USA: Cambridge University Press.

[5] Liao, S. & Zhao, T.S., 2002. "Measurements of Heat Transfer Coefficients from Supercritical Carbon Dioxide Flowing in Horizontal Mini/Micro Channels". *Journal of Heat Transfer,* Volume 124, p. 413.

[6] Glatzmaier, G. & Turchi, C., 2009. *"Supercritical Carbon Dioxide as a Heat Transfer and Power Cycle for CSP Systems".* Troy, NY, In Proceedings of the Supercritical Carbon Dioxide Power Cycle Symposium.

[7] Rodarte, M., 2011. *"The Development of an Experimental Test Facility to Measure Leakage Through Labyrinth Seals".* MS thesis, Nuclear Engineering Department, University of Wisconsin-Madison, Madison, WI, USA.

[8] Wright, A., 2010. *"Operation and Analysis of a Supercritical Carbon Dioxide Brayton Cycle",* Sandia National Laboratories, Albuquerque, New Mexico.

[9] Starkman, E. S., Schrock, V. E., Neusen, K. F. & Maneely, D. J., 1964. "Expansion of a Very Low Quality Two-Phase Fluid Through a Convergent-Divergent Nozzle". *Journal of Basic Engineering,* Volume 86, pp. 247-256.

[10] Lockhart, R. W. & Martinelli, R. C., 1949. "Proposed correlation of data for isothermal two-phase, two-component flow in pipes". *Chem. Engng Prog,* Volume 45(1), pp. 39-48.

[11] Chisholm, D., 1967. " A Theoretical Basis for the Lockhart-Martinelli Correlation for Two-Phase Flow". *International Journal of Heat and Mass Trasnfer,* Volume 10, pp. 1767-1778.

[12] Fauske, H. K., 1962. *"Contribution to the Theory of Two-Phase, One-Component Critical Flow",* ANL-6633, Argonne National Laboratory, Argonne.

[13] Zivi, S. M., 1964. "Estimation of Steady-State Steam Void-Fraction by Means of the Principle of Minimum Entropy Production.". *Journal of Heat Transfer,*Volume 86(2), p. 247.

[14] Moody, F. J. , 1965. "Maximum Flow Rate of a Single Component, Two-Phase Mixture. *Journal of Heat Transfer,*Volume 87(1), pp. 134-142.

[15] Ward-Smith, A. J., 1979. "Critical Flowmetering: The Characteristics of Cylindrical Nozzles with Sharp Upstream Edges". *International Journal of Heat and Fluid Flow,* Volume 1(3), pp. 123-132.

[16] Linfield, K., 2000. *"A study of the Discharge Coefficient of Jets from Angled Slots and Conical Orifices",* PhD thesis, Department of Aerospace Science and Engineering, University of Toronto, Toronto, ON, Canada..

[17] Brighton, J. A. & Jones, J. B., 1964. "Fully Developed Turbulent Flow in Annuli". *Journal of Basic Engineering,* Volume 86, pp. 835-844.

[18] Tao, L.N. & Donovan, W. F., 1954. "Through-Flow in Concentric and Eccentric Annuli of Fine Clearance With and Without Relative Motion of the Boundaries". *The Americal Society of Mechanical Engineers,* Volume 77, pp. 1291-1301.

[19] Jonsson, V. K. & Sparrow, E. M., 1965. "Experiments on turbulent-flow phenomena in eccentric annular ducts". *Journal of Fluid Mechanics,* Volume 25(1), pp. 65-86.

[20] Mehmet, S., Jerome, J. S., Ismail, A. & M. Evren, O., 2010. "Modeling of Newtonian Fluids in Annular Geometries with Inner Pipe Rotation". *Proceedings of the ASME,* Volume 1, pp. 1453-1461.

[21] Martin, H. M., 1908. "Labyrinth Packings". *Engineering,* pp. 35-36.

[22] Egli, A., 1935. "The Leakage of Steam Through Labyrinth Seals". *Transactions of The American Society of Mechanical Engineers,* Volume 57, pp. 115-122.

[23] Vermes, G., 1961. "A Fluid Mechanics Approach to the Labyrinth Seal Leakage Problem". *Journal of Engineering for Power,* Volume 83, pp. 161-169.

[24] Stocker, H., 1975. "Advanced Labyrinth Seal Design Performance for High Pressure Ratio Gas Turbines". *American Society of Mechanical Engineers,* Issue 75.

[25] Benvenuti, E., Ruggeri, G. & Tomasini, E., 1981. "Analytical and experimental development of labyrinth seals for process centrifugal compressors. *ASME,* Volume 32, pp. 21-35.

[26] Demko, J. A., Morrison, G. L. & Rhode, D. L., 1990. "Effect of Shaft Rotation on the Incompressible Flow in a Labyrinth Seal". *J. PROPULSION,* Volume 6(2), pp. 171-176.

[27] Demko, J. A., Morrison, G. L. & Rhode, D. L., 1988. "The Prediction and Measurement of Incompresible Flow in a Labyrinth Seal". *AIAA.*

[28] Hodkinson, B., 1939. "Estimation of the Leakage through a Labyrinth Gland". *Instituite of Mechanical Engineers,* Volume 141, pp. 283-288.

[29] Suryanarayanan & G. L. Morrison, 2009. "Labyrinth Seal Discharge Coefficient for Rectangular Cavities. *Proceedings of ASME,* Volume 2, pp. 99-114.

[30] El-Gamal, H. A., Awad, T. H. & Saber, E., 1996. "Leakage from labyrinth seals under stationary and rotating conditions". *Tribology International,* Volume 29(4), pp. 291-297.

[31] OpenFOAM, 2012. *"User Guide 2.1.1".* [Online]
Available at: http://www.openfoam.org/docs/user/userch1.php

[32] CFD, 2011 *"Two equation turbulence models".* [Online]
Available at http://www.cfd-online.com/Wiki/Two_equation_turbulence_models

[33] Wilcox, D., 1993. *"Turbulence Modeling for CFD".* DCW Industries, Inc.

[34] Span, R. & Wagner, W., 1996. "A New Equation of State for Carbon Dioxide Covering the Fluid Region from the Triple-Point Temperature to 1100 K at Pressures up to 800 MPa". *American Institute of Physics and American Chemical Society,* Volume 25(6), pp. 1509-1596.

[35] Dyreby, J., 2013 *Northland Numerics.* [Online] Available at: http://www.northlandnumerics.com/

APPENDIX A

Table A.1 Annular Orifice simulations – Geometrical Parameters @ 10Mpa, 498kg/m^3

Case #	No. of Teeth	Clearance (mm)	Tooth width (mm)	Tooth Height (mm)	Shaft Diameter (mm)	Shaft Speed (rpm)
1	1	0.06	0.424	0.79	3	0
2	1	0.09	0.424	0.79	3	0
3	1	0.12	0.424	0.79	3	0
4	1	0.15	0.424	0.79	3	0
5	1	0.09	1.272	0.79	3	0
6	1	0.09	5.088	0.79	3	0
7	1	0.06	0.2827	0.79	3	0
8	1	0.09	0.424	1.11	3	0
9	1	0.09	0.424	0.21	3	0
10	1	0.09	0.424	0.79	9	0
11	1	0.09	0.424	0.79	3	10,000
12	1	0.09	0.424	0.79	3	20,000
13	1	0.09	0.424	0.79	3	28,000
14	1	0.09	0.424	0.79	3	40,000
15	1	0.09	0.424	0.79	3	50,000
16	1	0.09	0.424	0.79	3	60,000

APPENDIX B

Table B.1 Labyrinth seal simulations – Geometrical Parameters @ 10Mpa, 498kg/m^3

Case #	No. of teeth	Clearance (mm)	Tooth width (mm)	Cavity/Tooth height (mm)	Pitch (mm)	Shaft Diameter (mm)	Shaft Speed (rpm)
1	3	0.06	0.424	0.79	1.692	3	0
2	3	0.09	0.424	0.79	1.692	3	0
3	3	0.12	0.424	0.79	1.692	3	0
4	3	0.15	0.424	0.79	1.692	3	0
5	3	0.09	0.424	0.79	1.092	3	0
6	3	0.09	0.424	0.79	1.392	3	0
7	3	0.09	0.424	0.79	1.992	3	0
8	3	0.09	0.424	0.79	2.292	3	0
9	3	0.09	0.424	0.21	1.692	3	0
10	3	0.09	0.424	0.51	1.692	3	0
11	3	0.09	0.424	1.11	1.692	3	0
12	3	0.09	0.424	0.79	1.692	3	10,000
13	3	0.09	0.424	0.79	1.692	3	20,000
14	3	0.09	0.424	0.79	1.692	3	28,000
15	3	0.09	0.424	0.79	1.692	3	50,000
16	3	0.09	0.424	0.79	1.692	3	100,000

APPENDIX C

Table C.1 Annular Orifice simulations – Operating Conditions for Case 2

Case #	Inlet Pressure (MPa)	Inlet Density (Kg/m^3)
1	11	372
2	11	498
3	10	372
4	9	372
5	9	498
6	7.7	630

Table C.2 Labyrinth seal simulations – Operating Conditions for Case 2

Case #	Inlet Pressure (MPa)	Inlet Density (Kg/m^3)
1	11	498
2	10	372
3	9	372
4	9	498
5	9	630
6	7.7	630

Table C.3 Plain orifice simulations – Operating Conditions for L/D ~ 5

Case #	Inlet Pressure (MPa)	Inlet Density (Kg/m^3)
1	9	372
2	9	498
3	10	372
4	10	498
5	11	372

APPENDIX D

Seal test section is the most important component of this test facility and is capable of handling pressures up to 2500 psi. Seal configuration of 0.75" Outer diameter and 1.5" long will be used to stack bushings of different diameters and lengths to create a labyrinth seal. The maximum shaft diameter that can be used to create a shaft-seal interface is 10mm.

Compressor which will be used to increase the pressure of CO_2 is a Hydro-Pac C2.4-40-2050LX/SS-CO2 and can support mass flow rates on the order of 0.1025 Kg/sec. This compressor is a one stage hydraulically driven intensifier and uses a 40 Hp motor to do so. Compressor has a maximum discharge pressure of 2400 psi and can handle inlet pressures ranging from 200-1500 psi. A voltage signal ranging from 0-10 V sent to the compressor from Labview will control the discharge pressure.

Buffer tank will dampen oscillations due to the compressor cycling and can handle pressures up to 2750 psi. Buffer tank is heated using two blanket heaters (3.4 KW each) to make sure that a large amount of liquid CO_2 is not accumulated in the tank. These blanket heaters are controlled by a Proportional Integral and Derivative (PID) controller implemented in Labview which continually monitors and adjusts the power sent to the heaters. Since, the buffer volume is heated; temperature of CO_2 will be as high as 100^0 C and needs to be cooled down before adjusting the temperature at the inlet to the test section. These two tasks are performed by pre cooler and pre heater as described.

Pre cooler is a straight tube in tube heat exchanger where S-CO_2 flows through the inner tube and chilled water flows in the outer tube. Pre heater is a 5.5 KW cartridge heater manufactured at the University of Wisconsin, Madison. A PID scheme implemented in Labview controls the power sent to the heaters and thereby, adjusts the temperature at the inlet to the test section.

Coriollis flow meter is a Micro Motion F025P319CCAAEZZZZ and will be used to measure the mass flow rate and the density before the test section inlet. This flow meter can handle pressures up to 2300 psi and can measure flow rate as high as 0.378 kg/sec.

Pressures at the inlet and outlet to the test section are controlled precisely by four control valves (CV 1, 2, 3 and 4).CV1, and CV 3 are Swagelok SS-4PDF4-PM and have a flow coefficient of 0.7for 5 turns open. These two valves are used for a coarse control of the pressure at the inlet and outlet.CV2, and CV4 are Whitney SS-31RS4-A and have a flow coefficient of 0.04 for 10 turns open. These two valves are used to make fine adjustments to the pressure at the inlet and outlet.

Reservoir tank will be used to separate saturated vapor from two-phase CO_2 exiting the test section. Fluid from the test section enters the tank as a two-phase mixture which is then exhausted through a long tube that runs into the gas cylinder. From there, the fluids separate into liquid and vapor counterparts in order to fill the volume of the gas cylinder entirely. An annular region which is slightly larger than the diameter of the inlet tube is used to extract CO_2 as saturated vapor through the same entry hole in the gas

cylinder. The vapor is then extracted through a compression-tee so that it can be cycled through the compressor.

One component not shown in the schematic is Mannesmann DEMAG grinding spindle ES 280 ZG and will be used to spin the shaft inside the seal test section. This spindle can hold collets with a clamping range of 5mm, 6.35mm, 8mm, and 10mm and spin at a maximum speed of 28,000 rpm.

Type E, K thermocouples are used throughout the facility to monitor the temperature of the flow. Omega dyne PX309-3KG5V pressure transducers are used to monitor the pressure at different locations in the loop.